Studies of Third-Order Nonlinearities in Materials and Devices for Ultrafast Lasers

by

Juliet Tara Gopinath

B.S., Electrical Engineering, University of Minnesota (1998)
S. M., Electrical Engineering and Computer Science,
Massachusetts Institute of Technology (2000)

Submitted to the Department of Electrical Engineering and Computer Science in partial fulfillment of the requirements for the degree of

Doctor of Philosophy

at the

MASSACHUSETTS INSTITUTE OF TECHNOLOGY

June 2005

Signature of Author . . . . . .
Department of Electrical Engineering and Computer Science
February 4, 2005

Certified by . . . . . .
Erich P. Ippen
Elihu Thompson Professor of Electrical Engineering
Professor of Physics
Thesis Supervisor

Accepted by . . . . . .
Arthur C. Smith
Chair, Department Committee on Graduate Students
Department of Electrical Engineering and Computer Science

Studies of Third-Order Nonlinearities in Materials and Devices for Ultrafast Lasers

by

Juliet Tara Gopinath

Submitted to the Department of Electrical Engineering and Computer Science
on February 4, 2005 in partial fulfillment of the
requirements for the Degree of Doctor of Philosophy in
Electrical Engineering and Computer Science

Abstract

Recent developments in telecommunications, frequency metrology, and medical imaging have motivated research in ultrafast optics. Demand exists for broadband components and sources as well as highly nonlinear fibers and materials. For this thesis, several different devices have been developed for such applications. Broadband saturable absorbers based on III/V and Si materials systems were developed for femtosecond lasers and have high reflectivity over 200 to 300 nm bandwidths. These absorbers were designed for modulation depths ranging from 0.3% to 18%. Self-starting modelocked operation with the absorbers was achieved in a variety of lasers including Ti:Sapphire, Cr:Forsterite, Er:glass, Cr^{4+}:YAG and erbium-doped bismuth-oxide fiber. In tapered microstructure fiber, highly nondegenerate four-wave mixing was achieved, with a frequency shift of 6000 cm^{-1} in an interaction length of only 1.4 cm. Amplification in erbium-doped bismuth-oxide fiber was demonstrated, with gains of 12 dB achieved between 1520 - 1600 nm in a 22.7-cm length. With a 55.6 cm length of bismuth-oxide erbium-doped fiber, an L-band modelocked laser was constructed, tunable between 1570 - 1600 nm. It produced 288-fs pulses at 1600 nm. Undoped highly nonlinear bismuth-oxide fiber was used to generate smooth, controlled supercontinuum between 1200 to 1800 nm. Pulse compression of 150-fs pulses to 25 fs was also demonstrated. Finally, the nonlinear refractive index coefficient and two-photon absorption coefficient of Ge-As-Se glasses were measured. $Ge_{35}As_{15}Se_{50}$ is found to have a nonlinearity 900 times that of silica.

Thesis Supervisor: Erich P. Ippen
Title: Professor of Physics, Elihu Thompson Professor of Electrical Engineering
Professor of Physics

ACKNOWLEDGMENTS

I do not think it possible to appreciate the sheer amount of work required for a Ph.D. until one has experienced it firsthand. My decision to pursue a Ph.D. was the right one, but I am excited that it is at an end, having missed every deadline possible. First and foremost, I would like to thank my wonderful thesis advisor, Professor Ippen. Without his insightful comments, intuition, high standards, enthusiasm, kindness, patience and willingness always to make time for another lengthy scientific discussion, this thesis would not exist. He has been a fantastic mentor and his generosity and openness with colleagues are to be admired. Working for Professor Ippen at MIT has made for a fabulous 6 years and 5 months of graduate school.

I thank both Professor Kaertner and Professor Kolodziejski for serving on my thesis committee. Professor Kaertner has taught me much about SBRs. His seemingly endless energy, countless ideas and suggestions, and the many derivations at his fingertips continue to inspire me. I have greatly enjoyed my research collaborations with Professor Kolodziejski and her sage advice. Saturable absorbers fabricated in her group are one of the few projects that continued through my entire graduate school experience.

We all miss Professor Haus, since his sudden departure in 2003. Professor Haus was amazing, with interests ranging from polarization mode dispersion to the expansion of the universe. I truly wish that I had more chances to interact with such a great man and for theoretical research.

Without my fabulous colleagues, my Ph.D. thesis would never have been a success. Dan Ripin was wonderful person to work with at MIT - mentor, colleague and friend. I look

forward to working with him at Lincoln Labs, and hope to repay him for the famous lunch he bought me as a prospective graduate student. (Of course, I would have never joined the Ippen group without that touch!) Matt Grein and I have had many interesting discussions at lunch, over coffee, or late at night. His enthusiasm and enjoyment of research never flag, and are a continual source of inspiration. Erik Thoen introduced me to pump-probe spectroscopy and really got me started in the lab. His seemingly unending patience and supply of time for research discussions really amaze me (most especially since I don't have them). Peter Rakich always has a suggestion for any experimental holdup. Most of the time, he is right. The supercontinuum research collaboration was much fun - I especially remember the two sleepless nights we spent trying to make the CLEO 2003 deadline (of course, we failed miserably!). Hanfei Shen has been a pleasure to work with. I have enjoyed our eclectic discussions ranging from restaurants to research to Boston nightlife, (and most especially, the night we took many measurements at the wrong wavelength!). I appreciate his careful proofing of my thesis and all the insightful questions. I know that I will leave the pump-probe setup in competent hands! Ali Motamedi juggles research and classes in a way that is superhuman. I wish him the best of luck with his Ph.D. and bequeath the excitement of heterodyne pump-pump measurements. I appreciate his introduction to high-quality expresso! Jason Sickler brings liveliness to the Ippen group, with never a dull moment. He does need to learn some polite words in Japanese! I can only look up to the work ethic of Marcus Dahlem. He brings good cheer to the lab, as well as beautiful photography. Afternoon coffee breaks with Dave Kielpinski are always enjoyable, whether the topic of discussion turns to atomic physics, politics, or economics. My good wishes to Peilin Hsiung with her future plans. As she herself said, with both of us to graduate, "It's like the ending of an era." We met in our first graduate school class, suffered through impossible homework assignments, shared an office, and participated in numerous optics group ski trips.

Collaborating with Sheila Tandon on the saturable absorber project has been fantastic. She is one of the most systematic and careful people I know. Gale Petrich has always been generous with his time and was always willing to teach me more about MBE growth, sample cleaving or fabrication. I had a wonderful time working with Kazi Abedin, during his stay at MIT (as well as Charles Kerbage, OFS). Kazi and Charles have more energy than I will ever have. I look forward to another round of margaritas and humor, with both of them. Pursuing research projects with Hideyuki Sotobayashi has been a pleasure. He has taught me a good deal about fibers, a little Japanese, as well as drawing my attention to many local concerts. I am saddened that he will return to Japan soon. Thomas Schibli and Oemer Ilday always had time to discuss research and ideas with me. I have learned much from both of them and was

always inspired by our many discussions. I am grateful for PohBoon Phua's assistance with the chalcogenide project. I can only admire his level of research efficiency. Marin Soljačić has always made time for me, despite a very hectic schedule. I enjoyed our discussions about z-scan and had a lot of fun introducing him to the experimental side of the world. Collaborations on saturable absorber projects with Felix Grawert have been interesting and rewarding. Additionally, I would like to thank other present and former group members including: Leaf Jiang, Elisabeth Koontz, Charles Yu, Pat Chou, John Fini, Laura Tiefenbruck, Juhi Chandalia, Aurea Zare, Rohit Prasankumar, Kaoru Minoshima, Mariana Carvalho, Jeff Chen, Lingze Duan, Fuwan Gan, Lia Matos, Shunichi Matsushita, Luciano Socci, Vivek Srinivasan, Yu Chen, Kenji Taira, Maciej Wojtkowski, Vikas Sharma, Robert Huber, Mike Watts, Milos Popovic, Norihko Nishizawa, Aaron Aguirre, Tony Ko, Drew Kowalevicz, Oliver Muecke, Richard Ell, Jung-Won Kim, Christian Jirauschek, Jonathan Birge, Wolfgang Seitz, Jan Molte-Fisher, Philip Wagenblast, Thomas Murphy and Farhan Rana. The group administrative assistants, Donna Gale, Cindy Kopf and Dorothy Fleischer, have helped me with many a difficult situation. Marilyn Pierce, in the EECS graduate office, has been very kind. Her smile and warm welcoming manner put me at ease upon my arrival to MIT.

Throughout the years, I have had a number of other mentors. Paul Juodawlkis and Joe Donnelly have always been just a phone call away at Lincoln Labs. Professor Gadi Eisenstein (Technion, Israel) told me about Professor Ippen's research group and Professors Jim Leger and C. C. Huang (University of Minnesota) supported me on my quest of graduate school. My viola professor, Professor Korey Konkol, at Minnesota inspired me, with his mathematical and musical background.

Graduate school would not have been the same without the generous support of a National Science Foundation Graduate Fellowship (1998-2001) and the IEEE/LEOS Graduate Student Fellowship (2003).

While my Ph.D. success has been due in large part to my learned colleagues, thesis committee and advisor, non-academic interests at MIT have also been important. They have served as a stress release, given me something else to do, and kept me happy. It may surprise some that the Institute has a high quality and eclectic arts and music program. I owe a big thanks to my Brahms piano quartet (MIT Chamber Music Society), an essential part of my life during my final PhD years. I have been privileged to play with extremely talented musicians - Vincent Cheung, Mea Cook, and Catherine McCurry. The haunting and tragic Brahms C minor piano quartet made the writing of this document somehow bearable. Memories of the recent performance will be forever entwined with my thesis! Additionally, my exceptional

music teachers and coaches at MIT and the New England Conservatory deserve a thank you: Carol Rodland, David Kim, Marcus Thompson, and David Deveau.

A careful examination of my MIT office yields clues of another interest: pottery. Peilin Hsiung first told me about the classes offered through the MIT Student Art Association. Art, with its pull on the abstract random side of the brain, is a perfect compliment to the systematic logical problem-solving demanded by many scientific problems. Bowls, cups, plates, vases, anything but scientific experiments! Most importantly, there is no stigma attached to failure.

My friends at MIT have been wonderful. Joyce Wu has taught me the importance of enjoying life, since our first meeting in an unpleasant quantum mechanics class. Fumei Lam has been a wonderful roommate of many years. I have enjoyed our discussions about music, MIT, and the world. Mike Masaki and Hans Callebaut can make me laugh about anything, however I feel. Athicha Muthitacharoen and I have been friends through many years of change for both of us. I would also like to thank Dave Strozzi, Aurelie Thiele, David Kokorowski, Juan Montoya, Ying Zhang, and Selen Stromgen for their friendship. From elsewhere, Wendy Cheng, Tina Johnston, Amit Seshan, and Quynh-Anh Hu.

My boyfriend, Brian Lay, has had a massive dose of this thesis. He's probably corrected more versions of it than anyone else and it has really put a stop to relaxing evenings for quite some time. I am very grateful for his love and patience and making sure that I remembered the importance of laughter and lightheartedness (even during thesis writing at its worst). My parents and my little sister, Charlotte, have been fantastic. Their confidence in me never failed, even in my lowest moments. They have always wanted the best for me, however inconvenient, and instilled a code of high standards and hard work. How could I ask for better role models! My Ph.D. experience at MIT has been very special. I cannot possibly thank everyone enough.

I dedicate my thesis to my family and Brian, with love.

February 2005.

TABLE OF CONTENTS

LIST OF FIGURES

LIST OF TABLES

CHAPTER 1: INTRODUCTION

1.1 Motivation

From 1998 to 2001, the telecommunications industry grew tremendously, driven by the apparent bandwidth demands of the Internet. In 2001, the 'bubble' of growth ended abruptly, and as of 2005, the telecom industry is still recovering slowly from the downturn. While the telecom market is still depressed, there is potential for improvement of the next generation systems. Integrated optical devices, such as all-optical switches and add/drop filters, will be important. Additionally, as bit rates increase, pulsed (modelocked) lasers will become attractive sources. In wavelength-division multiplexed systems (WDM) [1][2], channels are carried by separate colors and in current systems, each channel requires a separate transmitter. A modelocked laser could be spectrally-sliced to replace multiple single wavelength transmitters. Supercontinuum generated by a modelocked laser may also be an alternative for spectral slicing. High-repetition rate laser systems could replace cw-modulated laser sources in time-division multiplexed (TDM) communication systems [3][4].

While the promise of telecommunications has driven much of the research in ultrafast lasers and devices, in recent years, a newly developed field, frequency metrology [5][6][7], has also had a large effect. Frequency metrology combines atomic physics and femtosecond lasers allowing the construction of optical clocks, more accurate than the current time-standard (cesium clock). With a modelocked laser locked to an atomic transition, measurements of frequencies can be made more accurately for impact in the field of physics (e.g. measure-

ment of the fine-structure constant). Turnkey broadband femtosecond laser systems are critical for metrology. Thus, the development of broadband saturable absorbers that enable self-starting operation of such lasers is essential. Controlled spectral broadening in a highly nonlinear fiber is also an important function for frequency metrology systems.

In this thesis, a variety of devices and materials for the above applications have been investigated. Broadband saturable absorbers have been developed for femtosecond laser systems. The unique properties of highly nonlinear microstructure fiber, applicable to frequency metrology, have been demonstrated in a highly nondegenerate four-wave mixing experiment. Bismuth-oxide fiber has been used for broadband amplification and controlled supercontinuum generation. Finally, the nonlinearity and two-photon absorption of chalcogenide glasses, which have potential for highly nonlinear fiber and all-optical switching, have been investigated.

1.2 Modelocked lasers: an overview

Modelocked lasers are the most common method of femtosecond (10^{-15} s) pulse generation. The ratio of one femtosecond to one second is equivalent to the ratio of five minutes to the age of the earth. In femtosecond pulses, energy is concentrated in a few optical cycles and large peak powers are achievable with only moderate pulse energies. The geometrical length scale of femtosecond pulses is small: 10 fs corresponds to 3 μm in vacuum. The large bandwidth of femtosecond pulses is useful for communication systems and metrology; the high temporal resolution for ultrafast spectroscopy [8]; the high spatial resolution for optical coherence tomography (imaging) [9]; and the high intensities for applications such as nonlinear frequency conversion, laser material processing [10], surgery, and high intensity physics.

The generation and application of femtosecond pulses revolves around light-matter interaction. When an intense beam of light interacts with matter, both a linear and a nonlinear response are produced. The nonlinear response is proportional to the nonlinear susceptibility, $\chi^{(j)}$ where $j = 2,3,4$ etc. In optical fibers, due to the material symmetry, the lowest-order nonlinearities result from $\chi^{(3)}$ processes. The topics studied in this thesis: saturable absorption, spectral broadening, four-wave mixing, the nonlinear refractive index coefficient, and two-photon absorption, all result from $\chi^{(3)}$.

Femtosecond pulse generation, or modelocking, can be achieved by a variety of techniques. A set of equally-spaced laser cavity modes in the frequency domain is required. In a laser cavity, the mode spacing is given by:

(1.1)

$$\Delta\upsilon = \frac{c}{2n(\upsilon)L}$$

where $\Delta\nu$ is the mode spacing; c, the speed of light; $n(\nu)$, the frequency-dependent group refractive index; and L, the optical cavity length.

The electric field inside the laser cavity will be a superposition of modes:

(1.2)

$$E(t) = \sum_m a_m e^{i(2\pi\Delta\nu mt + \phi_m)}$$

where $E(t)$ is the time-dependent electric field; m is the mode number; a_m, the amplitude of the electric field in the *mth* mode; and ϕ_m, the phase of mode m. To achieve modelocking, the phases of each cavity mode must be locked together. One major limiting factor in short-pulse generation is dispersion, the frequency dependence of the refractive index n, which causes different wavelengths to propagate at different speeds. Another factor is the gain-bandwidth of the lasing medium.

Short femtosecond pulses can be generated by either active or passive modelocking. In any type of modelocking, a periodic time-dependent loss is added to the cavity. In active modelocking, an amplitude or phase optical modulator is placed inside the laser cavity. The modulator will shorten the optical pulse until it becomes shorter than the modulation window. At this point, the modulator will have little effect on the pulsewidth. In frequency space, the modulator scatters photons from a cavity mode into adjacent modes, thus locking the phases of the cavity modes. High repetition rate operation of an actively modelocked laser can be achieved by driving the intracavity modulator at a harmonic of the cavity repetition rate. Photons are now scattered in modes at a multiple of the cavity repetition rate, determined by the modulator drive frequency. The pulsewidth from an actively modelocked laser can be written as [11]:

(1.3)

$$\tau = \left(\frac{8g}{M\Omega_g^2\Omega_m^2} \right)^{0.25}$$

where g is the gain; M is the modulator strength; Ω_m the modulator frequency, and Ω_g is the gain-bandwidth. Ultimately, the pulsewidth from an active modelocked laser will be limited by the speed of the modulator electronics.

Shorter pulses can be produced by passive modelocking, in which the pulse itself creates an intensity-dependent loss known as self-amplitude modulation (SAM). As the pulse becomes stronger, the peak intensity increases, and SAM becomes larger. Elements that produce SAM are referred to as saturable absorbers. Passive modelocking can be implemented with a variety of techniques including soliton modelocking, polarization additive pulse modelocking (P-APM, fiber lasers), Kerr lens modelocking (KLM, solid-state lasers), and semiconductor saturable absorber modelocking. The mechanisms can be grouped into two categories: slow and fast saturable absorbers. Slow absorbers recover on a longer timescale than that of the pulse; fast saturable absorbers recover more quickly than the pulse. In slow saturable absorber modelocking, the leading edge of the pulse is shaped by the absorber, and the trailing edge by gain depletion. In contrast, a fast saturable absorber will shape both edges of the pulse. Slow absorbers include soliton modelocking and most semiconductor saturable absorbers. Fast absorbers include KLM and P-APM.

Over 150 years ago, J. S. Russell observed the first soliton in an English canal. Soliton modelocking in lasers results from the balance of group-velocity dispersion (GVD) [caused by the frequency dependence of the group refractive index] and self-phase modulation (SPM) [caused by the intensity dependence of the refractive index]. The master equation of modelocking describes the evolution of a pulse in a modelocked laser [12]:

(1.4)

$$\left[-j\varphi + g - l + \left(\frac{g}{\Omega_g^2} + jD \right) \frac{\partial}{\partial t^2} + \left(-j\delta + \gamma \right) |u|^2 \right] u = 0$$

where φ is the net linear phase shift; g, the laser gain; l, the linear loss per pass; Ω_g, proportional to the finite bandwidth of the laser gain; D represents the contribution of GVD, δ is the contribution from SPM; and γ, the SAM, inversely proportional to the loss saturation intensity. The exact solution of the master equation is [13]:

(1.5)

$$A(z,t) = A_o \operatorname{sec} h \left(\frac{t}{\tau} \right)^{(1+j\beta)}$$

where $A(z,t)$ is field, A_o the field amplitude; t is time; τ is the pulsewidth; and β the chirp parameter. The soliton pulsewidth and field amplitude follow the area theorem below.

(1.6)

$$A_o \tau = \sqrt{\frac{|\beta_2|}{\delta}}$$

where β_2 is the contribution from GVD and δ, the contribution from SPM. Thus, in soliton modelocking, the pulse energy will be limited by the dispersion of the cavity. High peak powers and small second-order dispersion yield the shortest pulsewidths.

Polarization additive-pulse modelocking [14] and Kerr lens modelocking [15] both utilize the nearly instantaneous Kerr effect in the laser medium itself. P-APM is applied to fiber lasers as it is compatible with single spatial mode propagation, and KLM, to solid-state lasers, as it requires free space propagation. The Kerr effect produces a change in index of refraction of a material directly proportional to the nonlinear refractive index coefficient and the optical intensity. An intensity-dependent index of refraction results from the Kerr effect. In KLM, a spatial profile with a varying index of refraction is produced, resulting in self-focusing. Thus, by placing an aperture appropriately in the cavity, higher intensity pulses can be favored. The aperture can either be physical, a 'hard' aperture, or 'soft', in which KLM produces better overlap with the gain medium, producing higher gains for higher intensities. The strongest KLM is produced where the change in intensity-dependent beamwaist is the largest, often near the edge of the cavity stability regime. In P-APM, intensity-dependent polarization rotation is produced by the Kerr effect. The peak of the pulse will acquire a different polarization state than the lower intensity wings. By passing the pulse through a polarizer, the wings can be eliminated.

While the shortest pulses are produced through fast saturable absorber modelocking, such as KLM, semiconductor saturable absorbers can also offer a convenient method of short pulse generation. Semiconductor saturable absorbers are a fairly recent technology development. A semiconductor laser was modelocked with a semiconductor saturable absorber for the first time in 1980 [16]. Several years later, a solid-state color center modelocked laser was modelocked with a saturable absorber [17]. Today, standard saturable absorbers can be purchased commercially. Semiconductor saturable absorbers have a section that absorbs until the interband absorbing transition becomes saturated. At high intensities, the absorption is fully bleached (saturated), and this state is favored over a low-intensity higher loss cw-state. Lasers can be modelocked purely through semiconductor saturable absorber effects or a saturable absorber can be used in combination with another modelocking mechanism such as soliton, KLM, P-APM, or an active modulator.

1.3 Outline of thesis

An outline of this thesis follows. In Chapter 2, research on a variety of semiconductor saturable absorbers is discussed. Characterization tools and techniques are presented in Section 2.3. Section 2.4 details the design, characterization and implementation of a high modulation depth saturable Bragg reflector (SBR) for an Er:Yb waveguide laser. Section 2.5 presents research on ultrabroadband III/V SBRs for an ultrafast Cr^{4+}:YAG laser. Large area, 500 μm, devices for lasers at 1550 nm, are detailed in Section 2.6. Section 2.7 is devoted to the discussion of the design, fabrication, and characterization of an ultrabroadband Si/Ge-based SBR and its implementation in an Er:glass laser. Highly nondegenerate four-wave mixing in microstructure fiber is the subject of Chapter 3. Section 3.2 gives some background on the topic, and Section 3.3 describes the highly nondegenerate four-wave mixing experiment. Chapter 4 describes experiments performed with erbium-doped and highly nonlinear bismuth-oxide fiber. Amplification studies of a short length of erbium-doped bismuth-oxide fiber are presented in Section 4.3. Section 4.4 describes an L-band laser constructed also with a short length of erbium-doped bismuth-oxide fiber. Supercontinuum and pulse compression experiments with lengths of undoped, highly nonlinear bismuth-oxide fiber are detailed in Section 4.5. In Chapter 5, research on Ge-As-Se chalcogenide glasses is presented. Measurements of their nonlinearities and TPA coefficients are detailed in Section 5.3 Finally, in Chapter 6, conclusions and future work are discussed. There are two appendices. Appendix A lists the SBR samples Professor Ippen's laboratory, giving the structure and other salient characteristics. Appendix B is devoted to the discussion of preliminary results of ultrafast pump-probe on broadband saturable absorbers.

CHAPTER 2: SATURABLE BRAGG REFLECTORS

2.1 Abstract

A variety of saturable Bragg reflectors (SBRs) have been developed for use in femtosecond and picosecond laser systems at wavelengths ranging from 800 nm to 1550 nm, using both III/V and Si-based materials. Section 2.4 discusses a high modulation depth 1550 nm, SBR on a conventional GaAs/AlAs mirror that was used to modelock an Er:Yb:glass waveguide laser. The structure was fabricated in collaboration with Professor Kolodziejski and G. Petrich at MIT. Coatings were deposited by P. O'Brien at Lincoln Labs. F. Grawert, in Professor Kaertner's group at MIT, performed the laser experiments. An ultrabroadband monolithic SBR is the subject of Section 2.5. The SBR was designed, characterized and implemented in an ultrafast Cr^{4+}:YAG laser, producing 36-fs self-starting pulses. The absorber was grown in Professor Kolodziejski's lab by G. Petrich, and post-growth oxidations were performed by A. Erchak. Collaborators in Professor Ippen's group include D. Ripin and H. Shen, who incorporated the device in the Cr:YAG laser. In Section 2.6, an extension of the ultrabroadband SBR research is described. Large area SBRs were pursued at a variety of wavelengths for lasers including Ti:Sapphire, Cr:Forsterite, Cr^{4+}:YAG, and bismuth-oxide erbium-doped fiber. Complete, 500-μm-diameter devices were fabricated, characterized, and implemented. The absorber was fabricated in collaboration with Professor Kolodziejski's group at MIT, with G. Petrich performing the growth of the structure, and S. Tandon implementing the post-growth oxidations. The structures were implemented in lasers by collaborators in Professor Kaertner's group, including J.-W. Kim, R. Ell, and T. Schibli, and from

Professor Ippen's group, J. Sickler and H. Sotobayashi. H. Shen collaborated on the design of the absorbers. Finally, in Section 2.7, the characteristics of a broadband Si/SiO_2/Ge-based SBR are discussed. Professor Kimerling's group at MIT fabricated the device, specifically J. Liu, S. Akiyama, and K. Wada. Professor Kaertner's group, specifically F. Grawert, collaborated on the device design. The saturable absorber was incorporated in the Er:glass laser by F. Grawert. H. Shen collaborated on the pump-probe measurements.

2.2 Background

Ultrafast lasers, producing picosecond and femtosecond pulse trains, have many applications including frequency metrology [5][6][7], nonlinear optics [8], medical imaging [9], and laser machining [10]. Often ultrafast lasers are not simply turnkey systems, making them difficult to utilize for practical applications. By incorporating a saturable absorber, one can stabilize such a laser against environmental fluctuations, relax critical cavity alignment constraints, and enable self-starting operation. However, femtosecond laser systems require very broadband devices that are not available commercially.

The shortest pulses to date have been generated in solid-state lasers with Kerr lens modelocking (KLM), which relies on a weak nonlinearity to produce an intensity-dependent loss [18][19][20]. In such systems, modelocking can be difficult to start, as extremely high peak intensities are required for the nonlinearity to become effective. Sometimes, even banging on the table is necessary to start KLM! Typically, in KLM systems, the laser cavity is operated near the edge of the stability regime, requiring critical alignment. However, with the addition of a saturable absorber, self-starting modelocking can be achieved and the constraints on cavity alignment can be relaxed [21][22]. If shorter pulses are produced, materials can be studied with higher time resolution. The insight gained can be used to design even better devices.

The application of saturable absorbers is not limited to solid-state KLM systems. They can also be used in fiber lasers [23][24][25], as the primary means of modelocking, or as simply a stabilization element. For this thesis, their application to both ultrafast solid-state laser systems: Cr^{4+}:YAG, Cr:Forsterite, and Ti:Sapphire, as well as fiber lasers, is investigated.

Saturable absorbers can either be used in a transmissive or a reflective geometry. In a transmissive geometry, care must be taken that the substrate of the absorber does not detrimentally influence the laser operation. To avoid this difficulty, absorbers can be fabricated on

a mirror, in a reflective geometry. A reflective saturable absorber is called a saturable Bragg reflector (SBR). However, integrating a high quality absorbing layer with a broadband and highly reflective mirror can be challenging.

Semiconductor-based saturable absorbers provide an intensity-dependent loss, favoring laser operation with high peak intensities, leading to pulsed, or modelocked output. Light at a desired wavelength excites carriers from the valence to the conduction band and is absorbed. As the incident light becomes increasingly intense, more and more carriers are excited. Eventually all of the states in the conduction band accessible to the incident radiation become full, and the absorber is "bleached", meaning that incident light is no longer absorbed. Absorbers are usually characterized by a bitemporal response, with the fast response originating from intraband dynamics and the slow response, from recombination.

A typical response from an InP/InGaAs absorber integrated with a GaAs/AlAs mirror is shown in Figure 2.1. Light is incident on the absorber at normal incidence, and a beamsplitter collects some of the reflected light. As the fluence incident on the absorber increases, the absorption saturates and the reflectivity of the device increases by 6%.

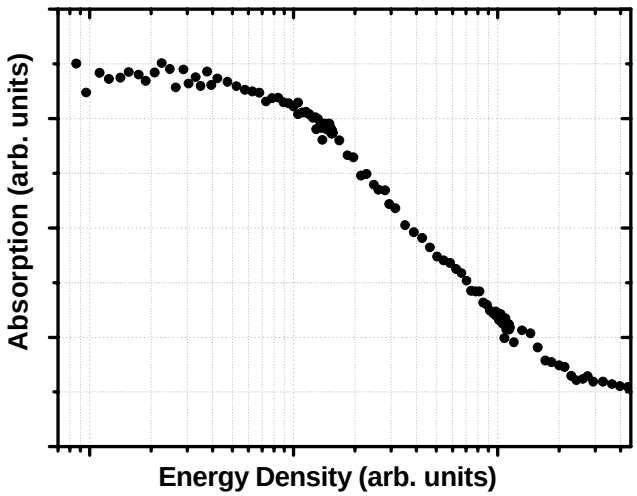

Figure 2.1 Saturation of absorption in a saturable absorber. Data taken on an InGaAs/InP-based absorber by E. Thoen.

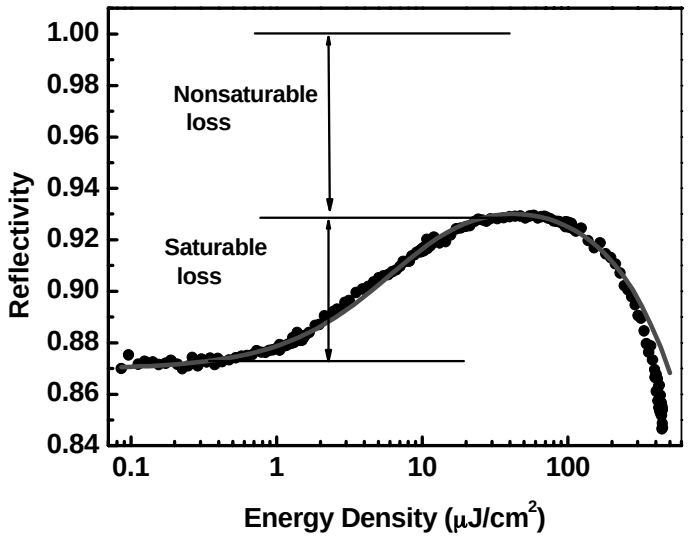

Figure 2.2 Time-averaged reflectivity of an SBR as a function of fluence [26].

There are several key parameters of a saturable absorber: nonsaturable loss, saturable loss or modulation depth, saturation fluence, and recovery time. Figure 2.2 illustrates two of these parameters: nonsaturable and saturable loss. The figure shows the reflectivity of a SBR as a function of fluence. In an SBR, nonsaturable loss is independent of power, and is generally undesirable. Material quality governs nonsaturable loss. Saturable loss is defined to be the difference between the loss measured when the absorption is fully bleached versus completely unbleached. One tailors the saturable loss of an SBR for a particular laser system. In general, fiber lasers (e.g. erbium-doped fiber lasers) require absorbers with 3% to 20% saturable loss, while solid-state lasers (e.g. Cr^{4+}:YAG, Cr:Forsterite, Ti:Sapphire) may only require saturable losses on the order of 0.3% to 2%. Another important SBR parameter is the saturation fluence, which is a measure of the absorber saturability. The saturation fluence is primarily a material parameter, but can also be influenced by the geometry of a structure. Generally, it is desirable to minimize an absorber's saturation fluence. To do this, absorbing layers in an SBR should be placed at the peak of the standing wave of the electric field to maximize the overlap of the electric field with the absorbing region.

The recombination time of an absorber determines whether it acts as a 'slow' or 'fast' absorber. A 'slow' absorber recovers on a time scale longer than the pulsewidth in the laser system, but a 'fast' absorber recovers faster than the pulsewidth in a particular laser system.

In general lattice-matched materials have nanosecond recovery times. However, by introducing defects through strain (lattice mismatch), low-temperature growth, or ion-bombardment, the recovery time can be reduced with only a small penalty in increased nonsaturable loss and decreased modulation depth. Defects introduce mid-gap states into the absorber, speeding up the recombination time.

For a slow saturable absorber, one that recovers more slowly than the pulse, the absorption, α, can be written as:

(2.1)

$$\alpha = \alpha_{ns} + \frac{\alpha_o}{1 + \frac{F}{F_{sat}}}$$

where α_{ns} is the nonsaturable loss, α_o the saturable loss, F_{sat}, the saturation fluence of the absorber and F, the fluence, energy/area, in the absorber.

Figure 2.2 illustrates some of the key parameters of a saturable absorber: saturable loss and nonsaturable loss. The reflectivity of a mirror with an integrated absorber is plotted versus incident fluence for a typical time-average measurement. These characteristics determine laser performance such as the startup modelocking conditions, the resilience of the system against Q-switching and other instabilities, and the shortest pulse width achievable.

2.3 Characterization tools and techniques

This chapter focuses on the design, characterization, and implementation of a variety of SBRs in both femtosecond and picosecond laser systems. In order to guarantee experimental success, important parameters of the SBRs such as absorber bandgap, modulation depth, saturation fluence, recovery time and reflectivity as a function of wavelength must be measured. Techniques used to determine these parameters for this research will be discussed.

Photoluminescence is a technique used to determine the bandgap of the absorbing regions in an SBR. The bandgap is generally chosen to coincide with the maximum gain of the laser system for which the absorber is intended. The bandgap of the SBR could also be chosen so that the entire laser spectrum is above the material bandedge. In this work, no systematic study of laser performance as a function of absorption bandgap was undertaken, but is an interesting topic for future investigations. A schematic of the experimental setup for photoluminescence is shown in Figure 2.3. A 1 W argon ion laser at 488 nm is used as the signal

source. The laser beam passes through a chopper, and is focused onto a sample mounted in a cryostat. Two large lenses collect the emission, which is focused into a spectrometer, and detected with a Ge or Si photodiode. Photoluminescence measurements can be made from 10K to 295K (room temperature).

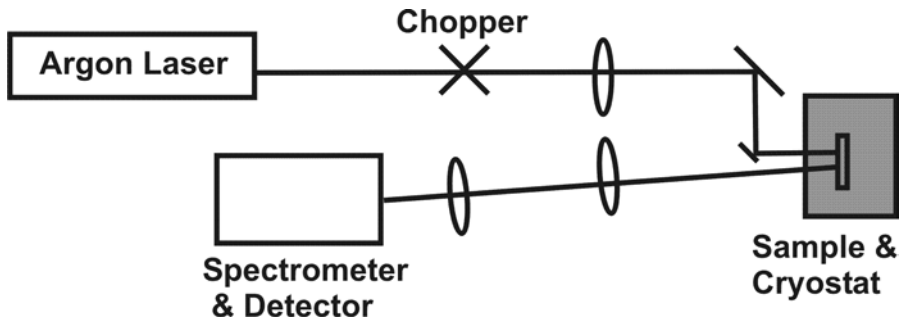

Figure 2.3 Schematic of photoluminescence measurement.

The reflectivity characteristics of the SBRs are measured with a Fourier transform infrared spectrometer (FTIR) [27]. Because the samples studied are small (mm or μm size), the microscope attachment of the FTIR is necessary. The instrument is based on a white light Michelson interferometer. The sample is placed in one arm, and a mirror is dithered in the other arm, generating an interferogram. When a Fourier transform is taken and compared to a known reference (such as air or a gold mirror), the reflectivity as a function of wavelength can be determined. Due to the large cone of angles impinging on the sample and the curved surface of the microscope objective, the absolute reflectivity of samples cannot be determined from an FTIR measurement. In the FTIR, the samples are measured with light incident at a nominal angle of 35 degrees. For mirrors designed at 1550 nm, this corresponds to a wavelength shift (to shorter wavelengths) of ~5%. Of course, to accurately determine this shift, simulations need to be performed. Reflectivity measurements at normal incidence are more desirable, as polarization effects are then eliminated. A spectrophotometer or microspectrophotmeter could be used instead to measure the sample reflectivity as a function of wavelength. In these instruments, white light impinges on a sample at normal incidence and is sent to a spectrometer. By comparing with a reference sample, instrument characteristics can be calibrated out of the measurement. However, spectrophotometers often require large (2 cm diameter) samples for reflectivity measurements. Micospectrophotometers employ a microscope to perform the measurements and are capable of a small spot size (microns).

The absorber saturation characteristics and temporal dynamics are studied with pump-probe spectroscopy, a common technique for studying material dynamics. Pump-probe mea-

surements provide temporal and/or spectral information depending on the specific experimental implementation. Time-resolved pump-probe measurements performed with femtosecond pulses can be thought of as a ‘femtosecond strobe’. In a pump-probe measurement, the sample is strongly perturbed or excited from equilibrium by a high intensity pump pulse. Following the pump pulse, at a varying time delay, the probe pulse, much weaker than the pump, impinges on the sample. The probe pulse is affected by the sample as it relaxes back to equilibrium. By detecting the transmitted or reflected probe pulse, information about a sample such as the strength of the nonlinearity and two-photon absorption, and the times for carrier-carrier scattering, carrier-phonon interactions and recombination can be determined [28].

In the pump-probe studies performed for this thesis, 110-fs to 150-fs pulses from a Spectra Physics Optical Parametric Oscillator (OPO), tunable between 1.4 and 1.6 μm are used as the source. The minimum time resolution of the setup, determined by the source pulsewidth, is about 155-fs to 212-fs (full-width half-maximum [FWHM] width of the cross-correlation). The OPO is synchronously pumped with a Ti:Sapphire at 82 MHz (Spectra Physics Tsunami) which, in turn, is pumped with a 10 W solid-state frequency-doubled YVO_4 (Spectra Physics Millenia). Typical spectra are shown for the Ti:Sapphire (Figure 2.4) and OPO (Figure 2.5). A typical OPO autocorrelation is shown in Figure 2.6. Figure 2.7 shows the pump-probe setup, similar to that reported in [29][30][31]. The setup is collinear and cross-polarized. The OPO pulses pass through an isolator and are then split into pump and probe pulses at a beamsplitter. The pump pulses are passed through a mechanical chopper, a half-wave plate, and a delay stage. The probe pulses pass through a half-wave plate, and are recombined with the pump at a polarizing beamsplitter. They are focused onto a sample with an aspheric lens, and a small portion of the reflected probe is focused onto a detector, which is connected to a lock-in amplifier and computer. A collinear setup is chosen, as this emulates the conditions in the lasers, and allows for high fluence measurements. The resolution limit of the setup is $\sim 10^{-3}$.

To determine the fluence incident on the sample, knife-edge measurements were used to determine the beam size at various distances from the focusing lens [26]. At a given position from the focusing lens, a knife-edge is translated perpendicular to the laser beam. A power meter is placed behind the knife-edge, and intensity as a function of position is recorded. The data can then be fitted to an error function, the integral of a Gaussian, and the spot size determined. If the spot size is measured at several different positions from the focusing lens, we can plot the spot size as a function of distance from the focusing lens. Using the relations for the propagation of a Gaussian beam, we can then determine the size of the

focused spot (beam waist). The beam size of a Gaussian beam is given by the following relation [32]:

(2.2)

$$w^2(z) = w_o^2\left[1 + \left(\frac{\lambda z}{\pi w_o^2 n}\right)^2\right]$$

where w_o is the minimum beam waist (radius); λ, the wavelength; z, the propagation distance from w_o; n, the refractive index of the medium through which the light is propagating, and w, the resulting beam waist (radius). With the knowledge of the beam waist, we can then calculate the fluence incident on the sample. The fluence is given by the following expression:

(2.3)

$$F = \frac{P}{R\pi\omega_o^2}$$

where F is the fluence; R, the laser repetition rate; and P, the average power incident on the sample. In a pump-probe experiment, the probe beam waist on the sample should be smaller than the pump beam waist. In the experiments in this thesis, the probe beam waist was 50-75% the size of the pump beam waist, allowing for good spatial overlap of pump and probe beams.

When pump-probe spectroscopy is performed on semiconductors above the bandgap, the excited carriers undergo processes that contribute to either bleaching or further absorption. For simplicity, I will first discuss the carrier dynamics that lead to bleaching signals in pump-probe. The time constants given are relevant for InP/$In_{0.5}Ga_{0.5}As$ and GaAs/$In_{0.5}Ga_{0.5}As$ systems. The bleaching and absorption dynamics are illustrated in Figures 2.8 and 2.9. When the pump pulse initially excites the system, the carriers form a non-equilibrium distribution. Within a limited energy range, the number of carriers within the conduction band is increased (as well as the number of holes in the valence band), creating a spectral ‘hole’ in the absorption spectrum. In less than 200 fs, the carriers undergo carrier-carrier scattering and thermalize into a hot Fermi distribution. Next, the carriers interact with phonons from the lattice and cool, in ~1 ps to equilibrium with the carriers [33]. Finally, the carriers recombine on a time scale of picoseconds to several nanoseconds, depending upon the ratio of nonradiative to radiative recombination.

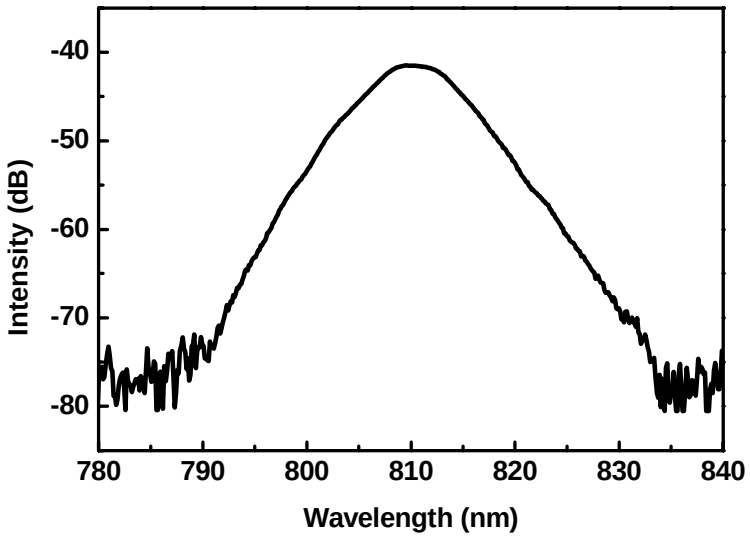

Figure 2.4 Typical spectrum of modelocked Ti:Sapphire laser.

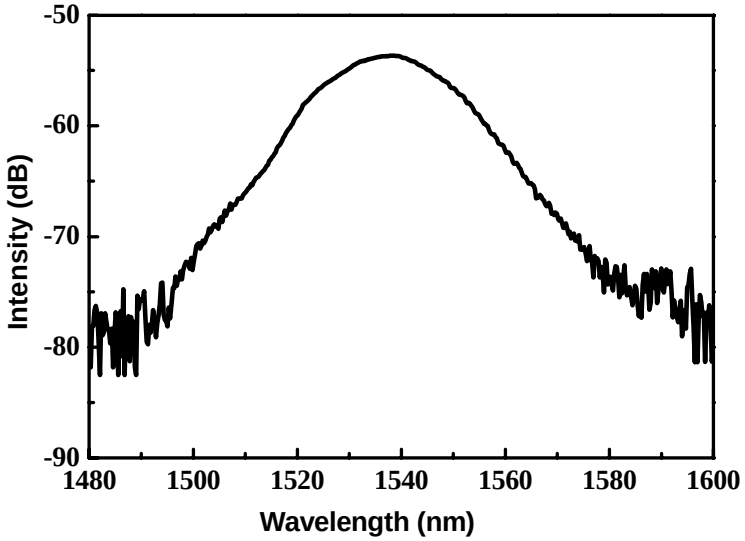

Figure 2.5 Typical spectrum of modelocked optical parametric oscillator.

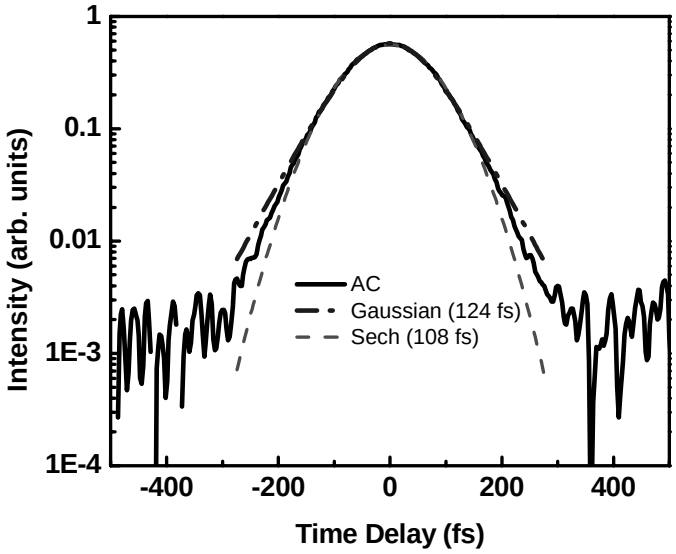

Figure 2.6 Typical autocorrelation of optical parametric oscillator. A measurement is shown in the solid line, a Gaussian fit in the dashed line, and a sech fit in the dot-dashed line. The pulse shape is in between that of a Gaussian and a hyperbolic secant (sech).

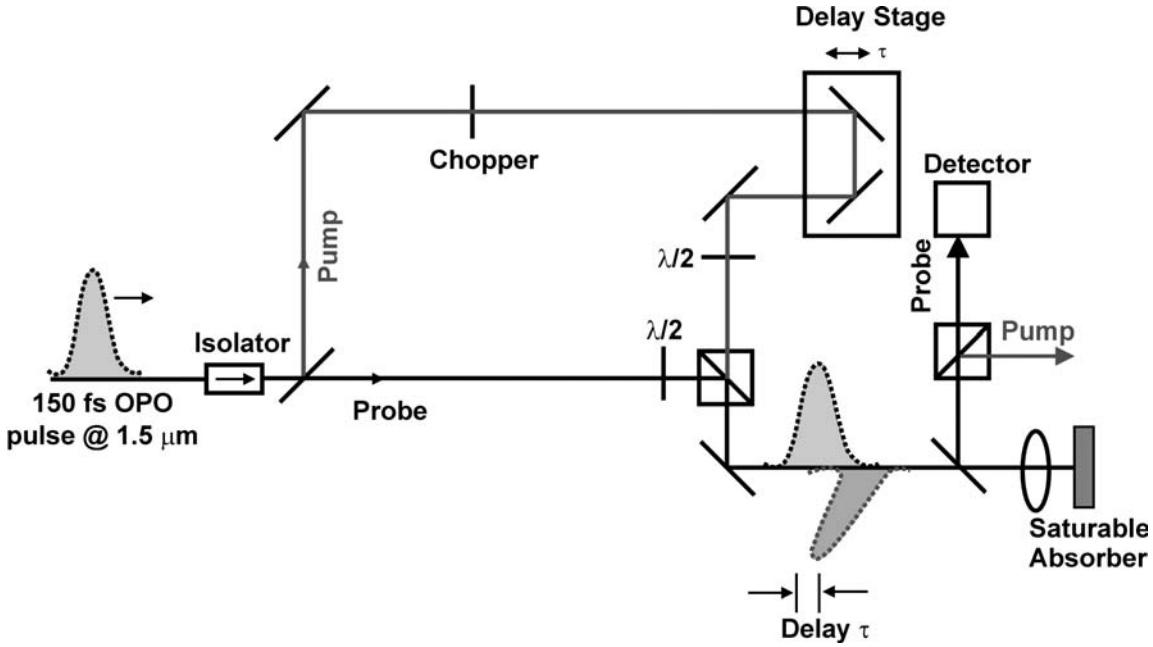

Figure 2.7 Schematic of pump-probe setup used for characterization of SBRs.

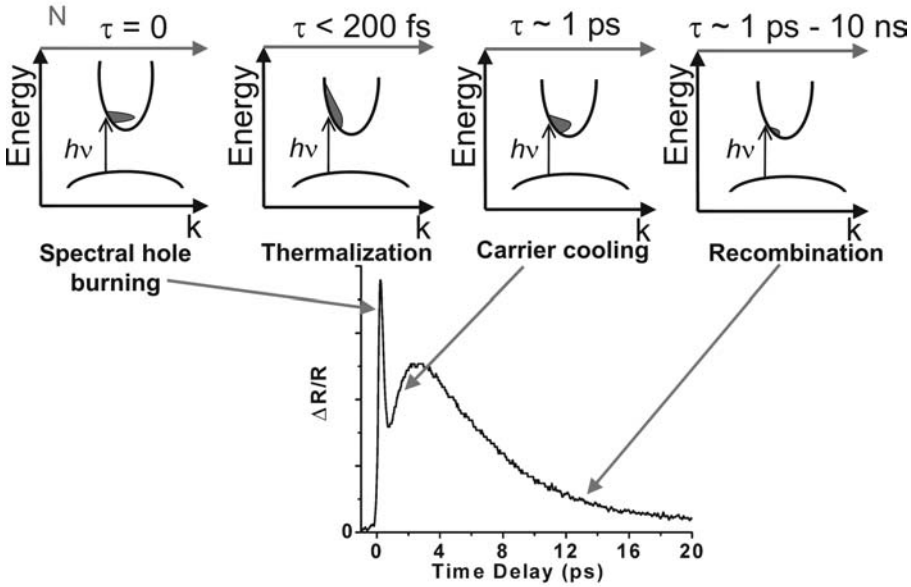

Figure 2.8 Bleaching dynamics in SBRs and example pump-probe trace. τ refers to the timescale of the event (e.g. spectral hole burning, recombination).

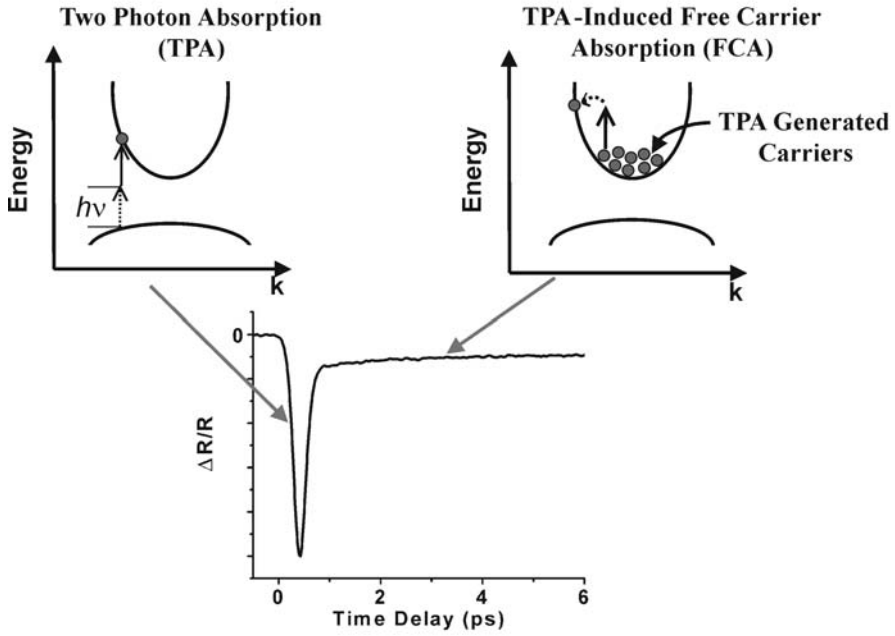

Figure 2.9 Absorption dynamics in SBRs and example pump-probe trace. The pump-probe trace is taken on a sample that only displays absorption dynamics (the wavelength of excitation is below the material bandedge). Generally absorption dynamics occur at higher fluences in SBRs (see Figure 2.2).

In addition to bleaching, additional absorption can also be caused by the carriers. The two main processes contributing to this are two-photon absorption (TPA) and free-carrier absorption (FCA) [34]. Two-photon absorption can only be observed by the probe when the pump and the probe are overlapped in time. In pump-probe, we only detect two-photon absorption of a pump and a probe photon and thus, TPA-caused absorption recovers on the time scale of the cross-correlation. Free-carrier absorption results when hot carriers created by TPA absorb an additional photon. Since FCA does not depend on a pump and probe photon being absorbed simultaneously, FCA can continue to be observed after the pump and probe lose their overlap in time.

Analytical expressions for the sample response to pump-probe spectroscopy can be written as follows.

(2.4)

$$\Delta R(\tau_d) = \int_{-\infty}^{\infty} I_{probe}(\tau_d - t) f(t) dt$$

where *f(t)* is the time-dependent response of the sample; and I_{probe}, the intensity of the probe pulse. The change in reflectivity, ΔR, is measured as a function of delay, τ_d, of the probe pulse from τ_0, the time at which the pump pulse hits the sample. Since electronic detection is slow, the signal detected will have the form of Equation 2.4 [28]. The time-dependent sample response, *f(t)*, is given by the following equation [35]:

(2.5)

$$f(t) = a_{ins}(t)\delta(t) + a_1 e^{\frac{-t}{\tau_1}} + a_2 e^{\frac{-t}{\tau_2}} + \ldots$$

where the amplitude factors are given by a_i, and the instantaneous response is represent by the Dirac δ function and the amplitude by a_{ins}. Excited-state dynamics are represented with exponentials, with relaxation times τ_i. Both electron and hole densities contribute when they have similar relaxation times. So, in order to extract the sample response, one must deconvolve the sample response from the cross-correlation. If the timescales of the signal response are much larger than the pulse cross-correlation width, the cross-correlation can be approximated as a δ-function, and then ΔR is directly proportional to the response of the sample.

2.4 High modulation depth saturable Bragg reflectors for Er:Yb waveguide laser

Fiber lasers are cheap, compact, and recently, have started to offer comparable performance to that of solid-state lasers. However, the maximum gain per unit length of fiber lasers is determined by the constraints on the doping levels of silica fibers with rare earth ions. Above a certain concentration, undesirable effects such as clustering and concentration quenching begin to occur. Thus, with relatively low gain per unit length, typical fiber lasers are tens of meters long, with repetition rates in the 10-30 MHz regime. An alternative, the phosphate-glass-based Er:Yb waveguide amplifier, has been developed recently (sold commercially by Teem Photonics) [36][37]. In waveguide amplifiers, much higher doping levels are achievable due to the phosphate glass host, making gains of 15 dB in 5 cm obtainable. These devices provide amplification over the telecom band, and may be a viable alternative to standard erbium-doped fiber amplifiers.

Because Er:Yb waveguide lasers are short (cm's), they have the potential for high repetition rate pulsed operation. Currently, high bit rate telecommunications uses cw lasers that are modulated and then multiplexed together to achieve the high data rates required. Harmonically modelocked (multiple pulse) fiber lasers could provide an alternative, but a compact fundamentally modelocked waveguide laser system would be more attractive than either of these options. A fundamentally modelocked high repetition rate laser system can be realized simply by incorporating a saturable absorber into the system. Since such systems generally also have high cavity losses, to be effective, the absorber must provide a high modulation depth.

In this research, a high modulation saturable absorber was designed, fabricated, and incorporated into an Er:glass laser [38]. With this absorber, picosecond pulses were produced, and with the addition of an acousto-optic modulator to the cavity, Q-switching instabilities were effectively suppressed.

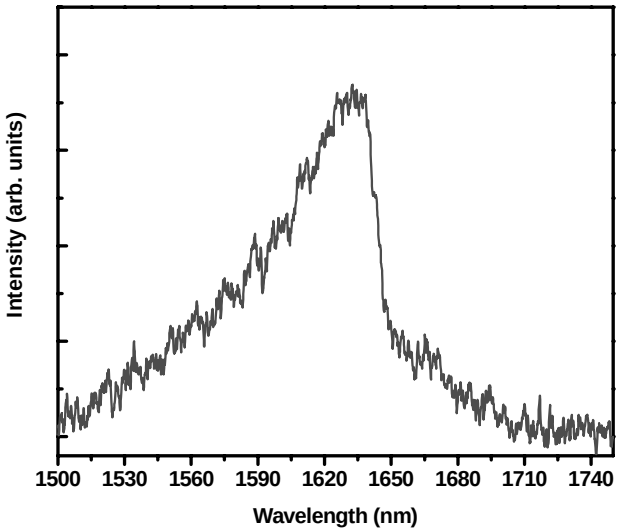

Figure 2.10 Photoluminescence (room temperature) of R921, a high modulation depth SBR designed for an Er:Yb waveguide laser.

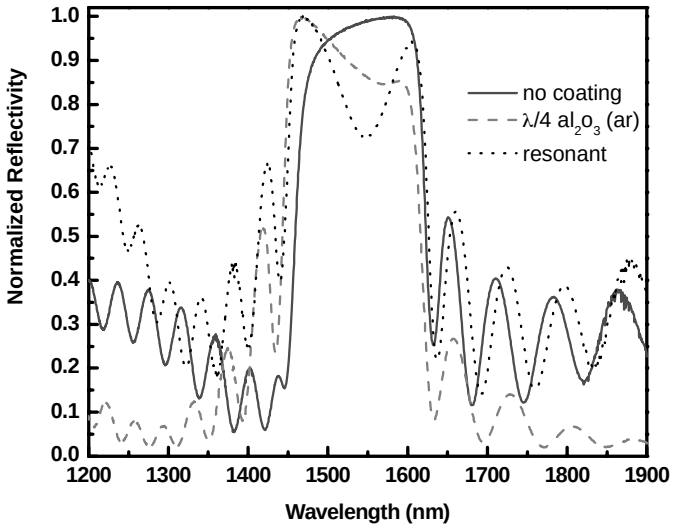

Figure 2.11 Reflectivity as a function of wavelength for R921 uncoated, antireflection-coated, and resonantly-coated.

A saturable absorber with a large adjustable modulation depth for use in a waveguide laser was designed and characterized. The structure (growth number R921, Kolodziejski) consists of a 22 pair GaAs/AlAs mirror, with a λ layer of InP on top containing 12 $In_{0.5}Ga_{0.5}As$ quantum wells. First, the 22 pair GaAs/AlAs mirror was grown by metal-organic chemical vapor deposition (MOCVD) and next, the absorbing region was fabricated by gas-source molecular beam epitaxy (MBE). (The MOCVD mirrors were purchased, but the MBE growth of the absorbing layers was performed at MIT). Before starting growth of the absorber layer, a 15 minute growth interruption was performed in which the GaAs mirror surface was exposed to cracked phosphine as opposed to cracked arsine, to localize defects at the GaAs-InP interface and ensure high quality quantum wells. Figure 2.10 shows the photo-luminescence of the structure, centered at 1635 nm. The sharp roll-off at longer wavelengths is caused by the roll-off of the mirror passband. To enhance the modulation depth, dielectric coatings were applied to the absorber. A $\lambda/4$ layer of HfO_2 was deposited as an antireflection-coating. On other samples, a resonant-coating, which acted like a lossy Fabry-Perot [36], coupling more light in at the resonant wavelengths, was applied. From the top down, the structure of the resonant-coating was as follows: 288 nm of SiO_2, 119 nm of Si, and 577 nm of SiO_2. Reflectivity measurements as a function of wavelength are shown in Figure 2.11 for an uncoated, antireflection-coated, and resonantly-coated structure.

To determine other important parameters of the absorber, pump-probe measurements on the structures were performed, shown in Figure 2.12. At low fluences, the SBR response showed a fast saturation due to spectral hole burning and a long recovery time of about 60 ps due to recombination. The recovery time was considerably shorter than the nanosecond recovery times observed in lattice-matched samples. Defect states at the InP/GaAs interface, due to the significant 3.5% lattice mismatch, were the most probable cause of this lifetime shortening. At higher fluences, an additional non-equilibrium carrier dynamic with a time constant of ~1 ps became apparent. The ~1 ps time constant was due to the cooling of hot carriers via carrier-phonon scattering that subsequently caused an increase in bleaching by state filling at the bottom of the band [33]. In the high fluence regime, the effect of TPA and FCA reduced the spectral hole-burning peak. The maximum modulation depth at 1560 nm for the uncoated structure was 7%, for the antireflection-coated structure 14% and for the resonant structure 18%.

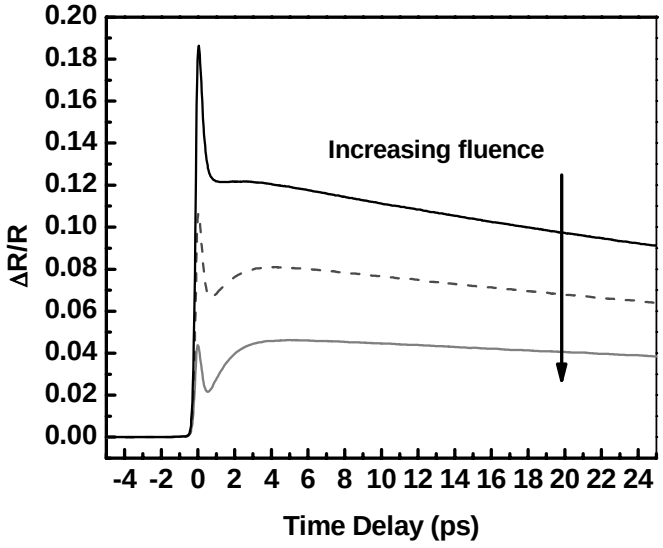

Figure 2.12 Pump-probe of resonantly-coated structure R921 at 1560 nm.

The structure was utilized in an Er:Yb waveguide laser [38], operated in a stretched-pulse laser configuration. The laser consisted of an Er:Yb waveguide amplifier from Teem Photonics with 10 dB of gain over the entire C-band, 5.3 m of single mode fiber (SMF-28), 0.9 m of dispersion compensating fiber with a dispersion of 90 ps^2/km, 5% and 10% output couplers, waveplates for polarization control, a saturable absorber, and an acousto-optic modulator (AOM). A schematic of the laser cavity is shown in Figure 2.13. The amplifier was pumped at 980 nm with 150 mW and an 18 mm lens focused the light onto the saturable absorber, to a spot size of 13 μm radius. Two 50 mm achromatic lenses surrounded the AOM, which was connected to a feedback circuit that suppressed Q-switching in the laser. The laser had a dispersion of -0.02 ps^2 and operated at 29 MHz. The absorber modelocked the laser producing pulsewidths ranging from 1.55 ps to 30 ps full-width half-maximum. However, SBR modelocked lasers are susceptible to additional Q-switching. Lasers with long upper state lifetimes and high repetition rates are most vulnerable, where the gain dynamics are slow compared to those of the optical field [39][40]. In such systems, Q-switching can be prevented by either hard saturation of the absorber [36][41], active feedback stabilization via gain [42], or intracavity loss modulation. In this particular experiment, Q-switching instabilities in the Er:Yb waveguide system were suppressed with an acousto-optic modulator [38].

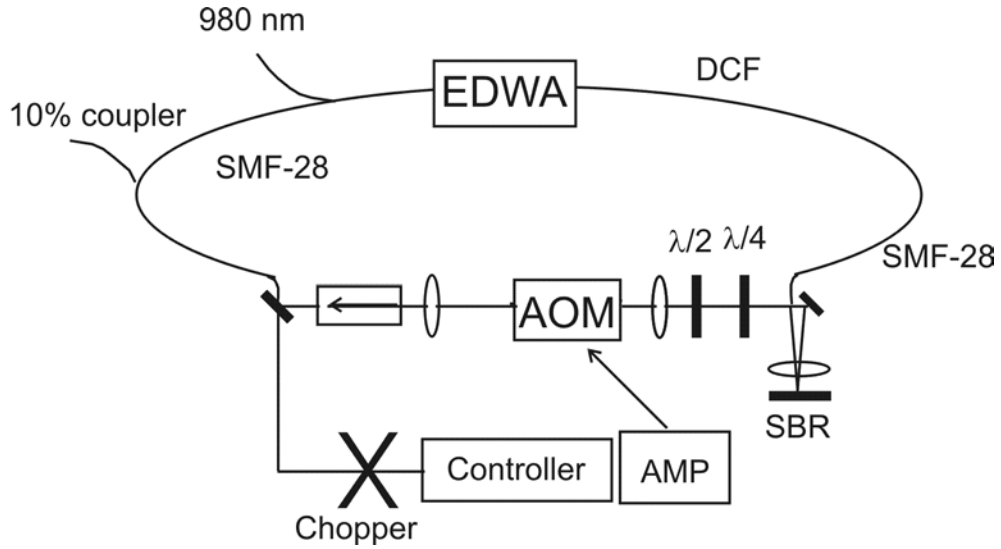

Figure 2.13 Schematic of Er:Yb waveguide laser [38]. EDWA (erbium-doped waveguide amplifier), AMP (amplifier), OC (output coupler), λ/2 (half-wave plate), λ/4 (quarter-wave plate).

2.5 Broadband III/V saturable Bragg reflectors for the Cr^{4+}:YAG laser

Despite the advantages of fiber and waveguide lasers such as cost and compactness, solid-state lasers still produce the shortest pulses at 1300 nm [43] and 1550 nm [44]. These solid-state lasers are modelocked with KLM, in which self-starting can often be a problem. By incorporating a semiconductor saturable absorber mirror, this difficulty has been overcome in a variety of solid-state lasers [45][46][47]. Since the pulse-shaping mechanism of KLM, the nonlinear refractive index, is very fast (response of a few femtoseconds in glasses [48]), the saturable absorber simply starts modelocking. The SBR becomes a 'slow' saturable absorber once pulses reach the femtosecond regime. In this section, broadband saturable absorbers designed to operate in a Cr^{4+}:YAG laser will be discussed.

Cr^{4+}:YAG, with its broadband gain-bandwidth centered at 1450 nm, is an attractive material for ultrashort pulse generation at telecommunications wavelengths. Unfortunately, Cr:YAG is an extremely low-gain system, and there are significant difficulties in obtaining laser crystals of sufficient quality. However, Cr^{4+}:YAG lasers operate at room temperature, and are therefore a nice alternative to cryogenically-cooled color center lasers. Despite the disadvantages of the material, KLM Cr^{4+}:YAG lasers have been used to generate femtosecond laser pulses in the wavelength range from 1300 nm to 1600 nm [49][50][51]. The bandwidth required for femtosecond pulses combined with the stringent loss constraints of this

laser puts high demands on the mirrors used in this system. Double-chirped mirrors, based on SiO_2/TiO_2 materials allow the required bandwidth and reflectivity specifications to be met [52] and in addition, compensate the dispersion of the Cr^{4+}:YAG laser crystal. Using these mirrors, and a purging system to eliminate the water absorption lines in the spectrum, 20-fs pulses were generated. These are the shortest pulses ever achieved from the Cr^{4+}:YAG laser [44].

However, the 20-fs pulses were not self-starting, making the laser difficult to use for applications. In Cr^{4+}:YAG lasers, modelocking has been demonstrated with saturable absorbers based on a variety of materials including InGaAs/InP [53], InGaAs/GaAs [54], or InGaAs/InAlAs [55][56]. In each case, conventional GaAs/AlAs Bragg stacks were used as the mirror. However, ultrashort pulses (sub-50-fs) will ultimately be limited by the bandwidth of such a mirror. For example, a 22-pair GaAs/AlAs Bragg mirror at 1500 nm has a 99.95% bandwidth of 100 nm. A solution was designed and implemented by *Zhang et. al* [57]. An InGaAs/InAlAs quantum well absorber bonded onto a gold mirror was used to generate 44-fs pulses from a Cr^{4+}:YAG laser. Because the intrinsic loss of the gold mirror was too large for the loss-sensitive Cr^{4+}:YAG laser, the gold mirror reflectivity was enhanced by $SiO_2/TiO_2/SiO_2$ dielectric layers [58]. Higher order dispersion rather than mirror bandwidth probably limited the pulsewidth achievable. While the pulses produced with the device were short, the fabrication of the SBR was complex.

In this section, we will discuss a broadband, monolithically-integrated SBR for a Cr^{4+}:YAG laser. When incorporated into a Kerr lens modelocked Cr^{4+}:YAG laser, 36-fs pulses with a FWHM bandwidth of 68 nm were generated [59].

The absorber consisted of an $In_{0.5}Ga_{0.5}As$ /InP quantum well absorber on top of a broadband, high-index contrast oxidized 7-pair $GaAs/Al_xO_y$ Bragg mirror. The absorbing region was made up of a 10 nm $In_{0.5}Ga_{0.5}As$ quantum well centered in a $\lambda/2$-thick InP layer. The mirror center wavelength was chosen to be 1440 nm, well matched to the gain peak of the laser and the double chirped mirrors (DCMs). The large difference in the refractive index of the mirror layers, GaAs (3.39 at 1550 nm), and Al_xO_y (1.61 at 1550 nm), allow the fabrication of mirrors that are highly reflective and broadband. With only 7 layer pairs, the calculated reflectivity is 99.9% over the wavelength range 1220 - 1740 nm and 99.99% over the range 1300 - 1600 nm. The refractive index and square of the electric field standing wave pattern in the high-dielectric contrast SBR are shown as a function of position in Figure 2.14. For contrast, in Figure 2.15, the measured reflectivity of a conventional GaAs/AlAs mirror and $GaAs/Al_xO_y$ oxidized mirror are shown.

The saturable absorber mirror and absorber regions were fabricated through gas-source molecular beam epitaxy with the mirror layers grown as GaAs/AlAs. Before starting growth of the absorber layer, a 15 minute growth interruption was performed in which the GaAs mirror surface was exposed to cracked phosphine as opposed to cracked arsine, to localize defects at the GaAs/InP (3.5% lattice mismatch) interface and ensure high quality quantum wells. Following growth, a wet-oxidation process was used to convert the AlAs layers to Al_xO_y [60]. In the wet oxidation setup, nitrogen gas carried water vapor from a heated bath to the sample located in a furnace tube. A cleaved rectangular piece of the Cr^{4+}:YAG SBR (growth number R885, Kolodziejski) was placed within a wet oxidation furnace at 400^oC. Because the oxidation process converts high-index AlAs to low-index Al_xO_y laterally from the edge of the structure, only material near an exposed edge oxidizes. After 9.5 hours of oxidation, the resulting Al_xO_y layers extended as far as 200 to 300 μm into the structure, a significantly larger area than previously achieved in VCSELs. When the AlAs is converted to Al_xO_y, a 10 to 20% layer thickness contraction occurs. The layer contraction, combined with the weak bonds between the GaAs and Al_xO_y layers, makes the structures susceptible to delamination, or layer peeling. However, the right combination of oxidation time and temperature can prevent the undesirable effects of delamination. Cross-sectional scanning electron micrograph (SEM) images of typical unoxidized (as-grown) and oxidized SBR structures are shown in Figure 2.16(a) and (b). The irregular appearance of the polycrystalline or amorphous Al_xO_y shown in Figure 2.16(b) was due primarily to the cleaving. No delamination of the layers is apparent.

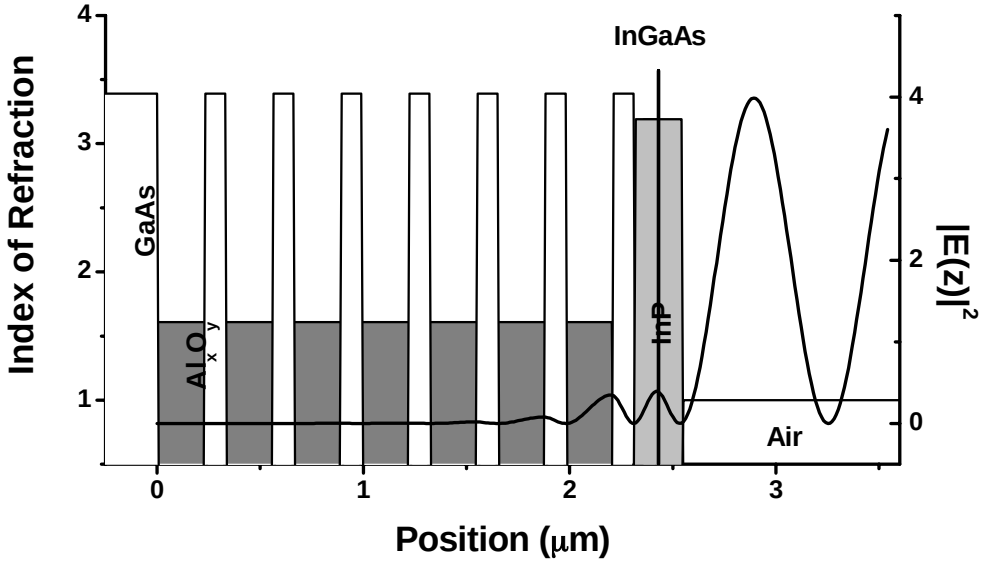

Figure 2.14 Refractive index and square of electric field standing wave pattern in the broadband SBR.

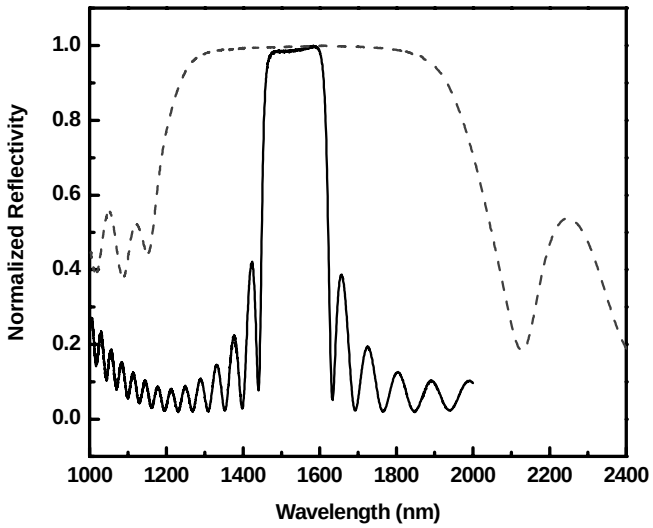

Figure 2.15 Reflectivity as a function of wavelength for a 22-pair GaAs/AlAs mirror (solid black) or an oxidized 7-pair GaAs/Al_xO_y mirror (dashed gray).

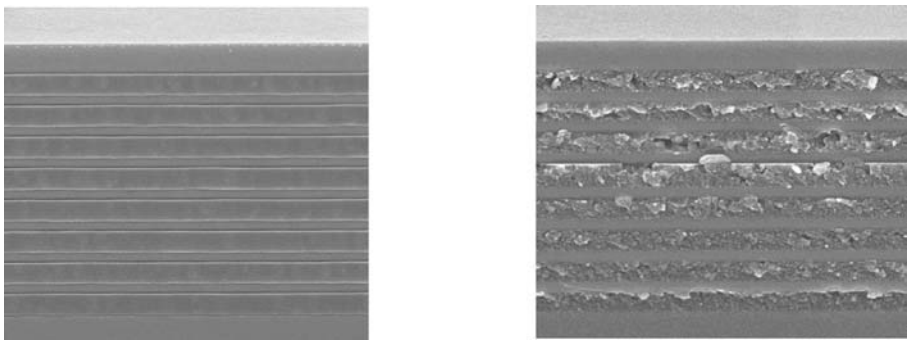

(a) (b)

Figure 2.16 Typical cross-sectional scanning electron micrograph of a) unoxidized (as-grown) b) oxidized SBR structure.

The SBR's optical properties were studied using several techniques. Mirror reflectivity was characterized using Fourier transform infrared spectroscopy, and is shown in Figure 2.15. Qualitatively, the SBR had a stopband from 1300 to 1800 nm. The exact reflectivity can be determined accurately through measurements of the device in a laser. Using the analysis below, we determined the absolute reflectivity of the absorber to be > 99.2% [61]. The laser threshold condition can be written as:

(2.6)

$$P_{th} = (L - \ln R)\frac{Ah\omega_p}{2\sigma\tau_f\eta_{pe}}$$

where P_{th} is the threshold power; R is the reflectivity of the output coupler; A is the cross-section of the beam focus in the laser crystal; ω_p is the frequency of the pump light; σ is the stimulated emission cross-section; τ_f is the fluorescence lifetime; η_{pe} is the overall pump efficiency; and L, the total optical loss in the cavity excluding the output coupler. When one element in the cavity is changed, such as a mirror or the SBR, all values remain constant except for R, L, and η_{pe}. To simplify further, we can assume that η_{pe} is relatively constant, as the mode in the cavity will not differ significantly with a slightly different mirror such as the SBR or output coupler. Equation 2.6 can then be rewritten as:

(2.7)

$$P_{th} = k(L + T)$$

where T is the transmission of the output coupler, and k is a constant. The approximation below is used to simplify Equation 2.6.

(2.8)

$$\ln(R) = R - 1 = -T$$

which assumes $R \sim 1$, and $T << 1$. Thus, the insertion loss of one mirror (or SBR) can be determined from three datasets of laser output power versus input power (L-L curve). By determining the laser threshold (onset of lasing) from the L-L curves, we can calculate the loss of the unknown mirror. In datasets *x* and *y*, the resonator has a known mirror (**Mirror A**) in place of the SBR, but has two different output couplers OC_x and OC_y. The same output coupler, OC_x, is used in datasets *x* and *z*, but they have different end mirrors - **Mirror A** and the SBR. In datasets *x* and *y*, the loss term, *L*, remains constant, and *T*, is known. The constant in Equation 2.7 can be determined.

(2.9)

$$P_{th,x} - P_{th,y} = k(L_x - L_y) + k(T_x - T_y) = k(T_x - T_y)$$

Using *k*, we can now solve for the loss of the SBR as follows, by comparing the conditions of resonators *x* and *y*.

(2.10)

$$\frac{P_{th,z} - P_{th,x}}{k} = (L_z - L_x) = (L_c + L_{SBR}) - (L_c + L_{mirror\_a})$$

where L_c accounts for cavity losses excluding the output coupler, SBR or end mirror (**Mirror A**). The loss of the SBR is represented as L_{SBR} and that of the end mirror, L_{mirror_a}. We can now write:

(2.11)

$$L_{SBR} = L_{mirror\_a} + \frac{P_{th,z} - P_{th,x}}{k}$$

Thus we can determine the reflectivity of the SBR.

The bandedge of the quantum well, 1540 nm, was determined through photoluminescence, and is shown in Figure 2.17. Typical pump-probe traces at 1540 nm are shown in Figure 2.18. From pump-probe measurements as a function of fluence, the saturation fluence is estimated to be on the order of ~10 $\mu J/cm^2$, the maximum saturable loss is 0.3% and the recombination time, 40 ps.

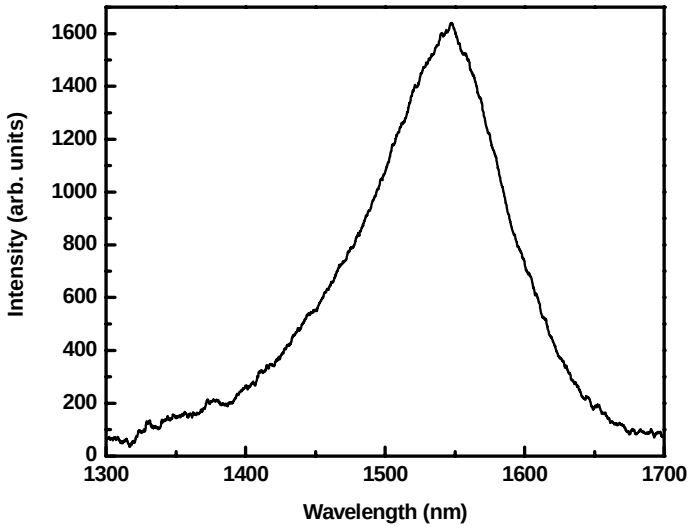

Figure 2.17 Photoluminescence (room temperature) from broadband oxidized absorber.

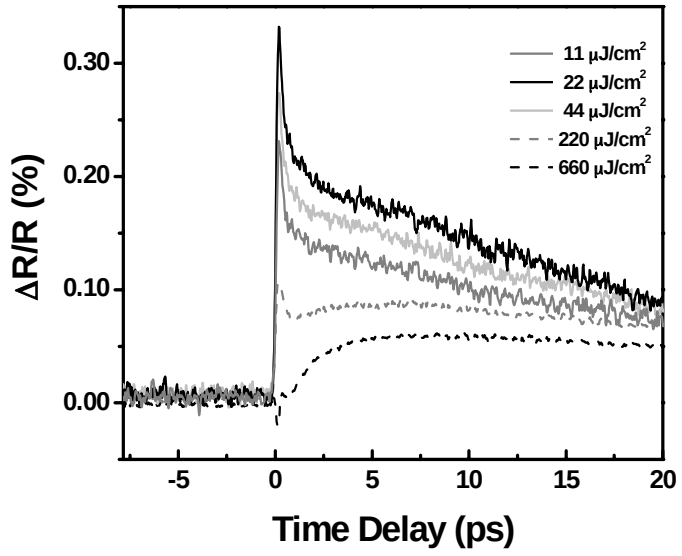

Figure 2.18 Pump-probe traces as a function of fluence at 1540 nm on the broadband absorber.

The broadband SBR was placed in a z-fold Cr^{4+}:YAG laser cavity, shown in Figure 2.19. The cavity consisted of a 2 cm Cr^{4+}:YAG crystal (E. L. S. Co., A. V. Shestakov) with two 10 cm radius of curvature double-chirped mirrors placed on either side. One arm of the cavity contained an output coupler, and the other, a 10 cm double-chirped mirror that focused

the beam onto the SBR to a spot size of ~50 μm radius. The Cr^{4+}:YAG crystal was pumped with an 11 W Nd:YVO_4 laser. The output coupler (OC) had a transmission of 0.7% at 1515 nm and <1.4% transmission from 1420 to 1630 nm. By changing the radius of curvature of the DCM closest to the SBR, the fluence on the SBR could be varied, as long as the spot was still smaller than the SBR oxidized region. To compensate dispersion in the laser cavity, necessary for ultrashort pulse generation, the laser cavity was designed to have 6 DCM reflections each cavity round-trip to compensate the normal dispersion of the Cr^{4+}:YAG crystal.

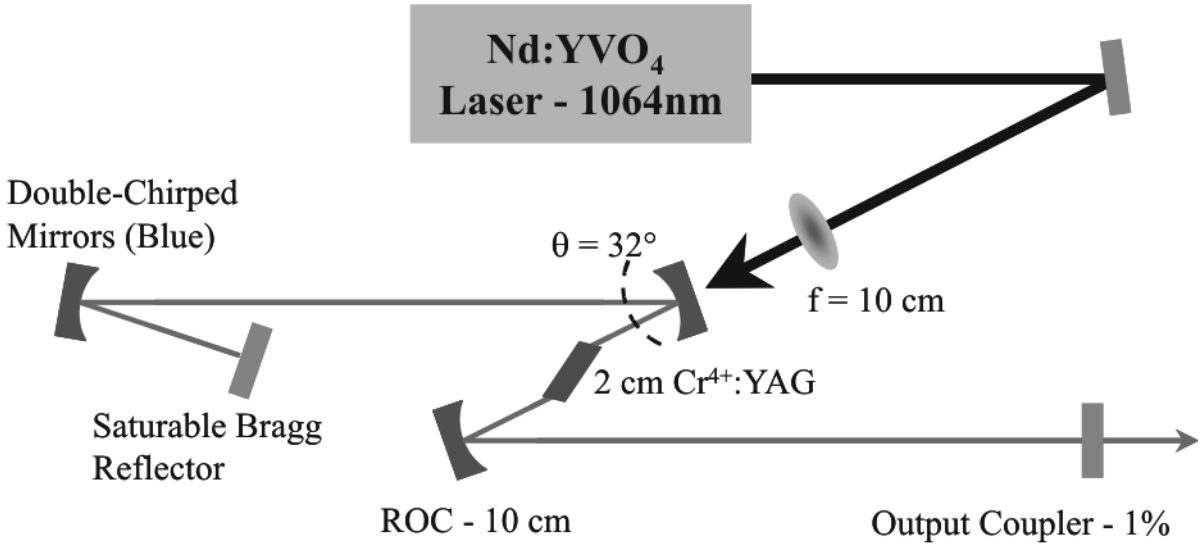

Figure 2.19 Schematic of z-fold Cr^{4+}:YAG laser incorporating the broadband oxidized SBR.

When the SBR was incorporated in the laser, the output power decreased from 600 mW to 300 mW, with 9 W of absorbed pump. No damage to the SBR was observed during laser operation and the samples did not appear to degrade over a long period of time in the laboratory. A birefringent filter was inserted in the laser cavity to tune the center wavelength. The SBR produced picosecond pulses, tunable between 1400 to 1525 nm but the roll-off of output coupler reflectivity limited modelocked operation on the short wavelength side of the spectrum. Next, the birefringent filter was removed, and the laser cavity aligned to optimize KLM. To produce the shortest pulses, the curved mirror separation and the laser crystal position were varied. Because of the water absorption lines in air at wavelengths shorter than 1500 nm, KLM was only possible when the cavity was enclosed in plastic tubes and purged with dry nitrogen gas to remove water vapor.

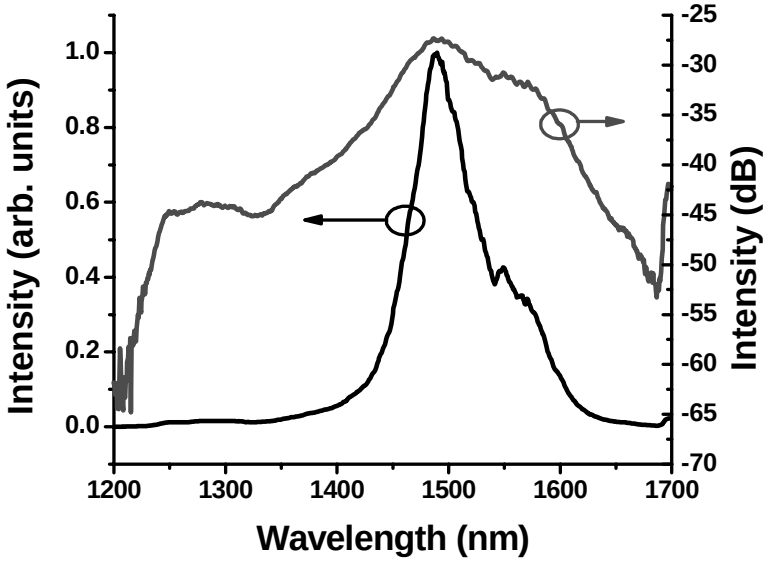

Figure 2.20 Spectrum of self-starting Cr^{4+}:YAG laser incorporating broadband SBR [59].

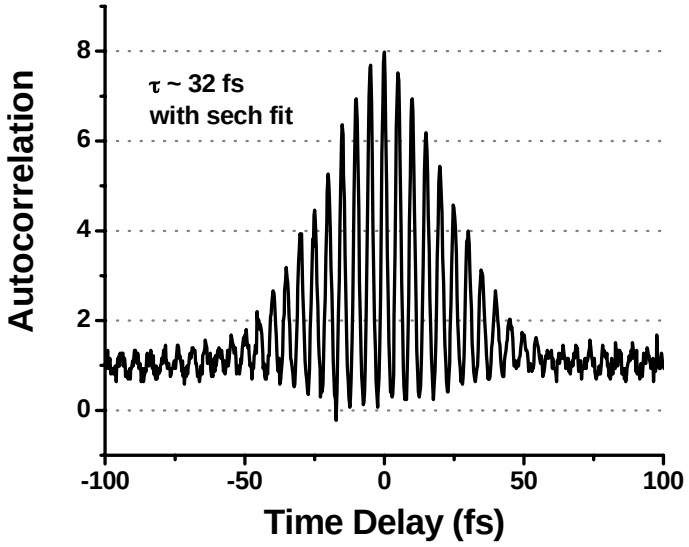

Figure 2.21 Fringe-resolved autocorrelation of 32-fs pulse from self-starting Cr^{4+}:YAG laser incorporating broadband SBR [59].

Modelocked operation yields a spectrum centered at 1490 nm with a FWHM of 68 nm. A plot of the modelocked optical spectrum is shown on linear and logarithmic scales in Figure 2.20. The optical spectrum extends from 1200 to >1700 nm, the limit of the optical spectrum

analyzer. In Figure 2.21, an autocorrelation, measured by a fringe-resolved two-photon absorption autocorrelator [62], is shown. Assuming a secant-hyperbolic (sech)-shaped pulse, the autocorrelation yields a pulsewidth of 32 fs. However, it is known that the width of a non-sech-shaped pulse is often underestimated by a sech-shaped fit. The measured spectrum corresponds to a Fourier limit of 36 fs.

With this SBR, 35-fs self-starting pulses were produced from the Cr^{4+}:YAG laser, the shortest self-started pulses to date [59]. We believe that the pulses were not limited by the mirror bandwidth, but by two-photon absorption (TPA) and free-carrier absorption (FCA) in the structure itself [29]. Using the operating parameters of the laser, we calculated an intracavity fluence of 1 mJ/cm^2 incident on the SBR. Careful examination of the pump-probe traces in Figure 2.18 at a similar fluence indicated that the absorber was overly saturated. Two-photon absorption caused the SBR to act as an inverse saturable absorber, in which the loss increased as fluence increased. While TPA can stabilize lasers against Q-switching instabilities, in this case, TPA and FCA may limit the pulsewidth achievable. In general, operation around the saturation fluence of an SBR is desired, as it produces the maximum change in reflectivity for a given change in fluence and does not suffer from absorption losses (TPA, FCA). To mitigate the effects of TPA and FCA, the spot size on the SBR could be increased, thus lowering the intensity, and therefore TPA, for a given power. However, the small device area did not allow a larger spot size. The fabrication of larger oxidized regions or the use of materials with a lower TPA coefficient than that of InP/$In_{0.5}Ga_{0.5}As$ should enable shorter self-starting pulses.

2.6 Large area saturable Bragg reflectors for lasers including Ti:Sapphire, bismuth-oxide erbium-doped fiber, and Cr:Forsterite

Larger area oxidized mirrors were developed, in an attempt to achieve shorter self-starting pulses from a variety of solid-state lasers. However, large area GaAs/Al_xO_y-based structures could not be fabricated. Delamination was a persistent problem, caused by the weak bond between the GaAs and Al_xO_y and the 10-20% thickness contraction of the AlAs when converted to Al_xO_y. Examples of delaminated structures are shown in Figures 2.22 and 2.23. Low-temperature oxidation techniques stabilize the mirror layers [59], but limit the dimensions available for oxidation. By replacing GaAs layers with $Al_{0.3}Ga_{0.7}As$ layers, the bond at the interface with the Al_xO_y layer is strengthened and greatly extends the achievable oxidation dimensions [63][64]. With this design modification, complete oxidation of 500 μm diameter mesas was demonstrated (Figures 2.24 and 2.25).

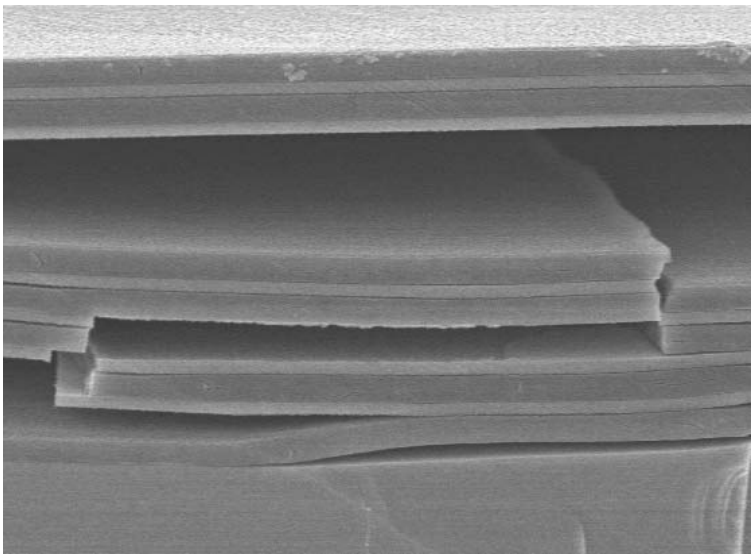

Figure 2.22 Side view of a delaminated GaAs/Al_xO_y interface in broadband oxidized absorber (scanning electron micrograph).

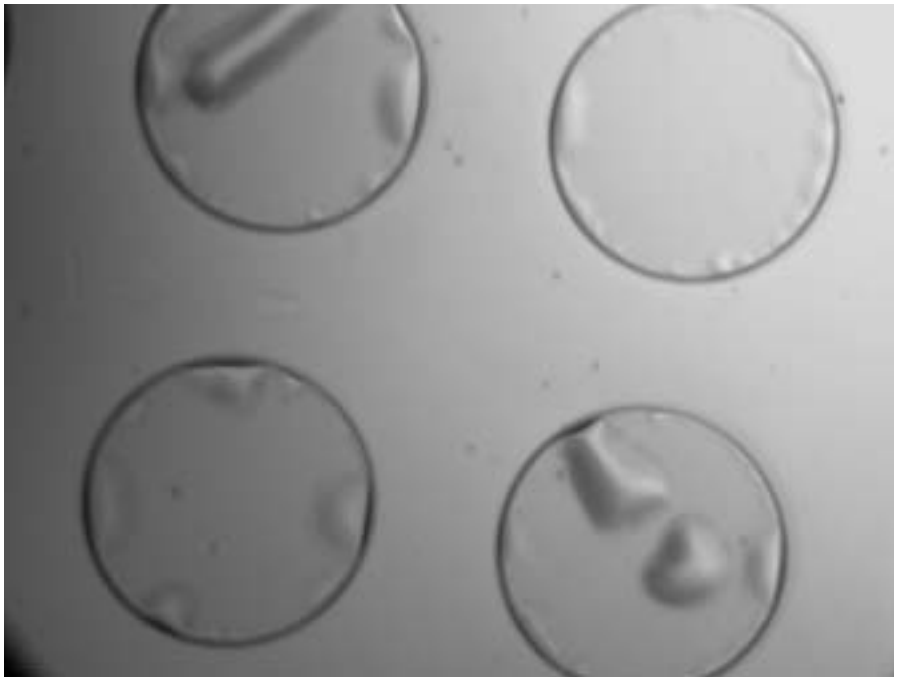

Figure 2.23 Top view of a delaminated mesa structure (microscope image).

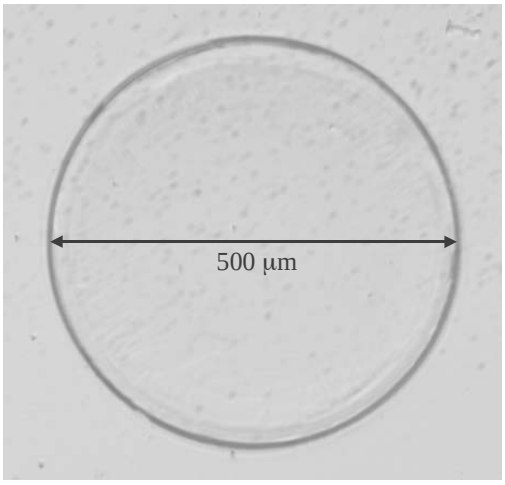

Figure 2.24 Top view of fully oxidized 500 μm mesa consisting of an $Al_{0.3}Ga_{0.7}As/Al_xO_y$ mirror and an absorber for the Cr:Forsterite laser (microscope image) [63][65][66].

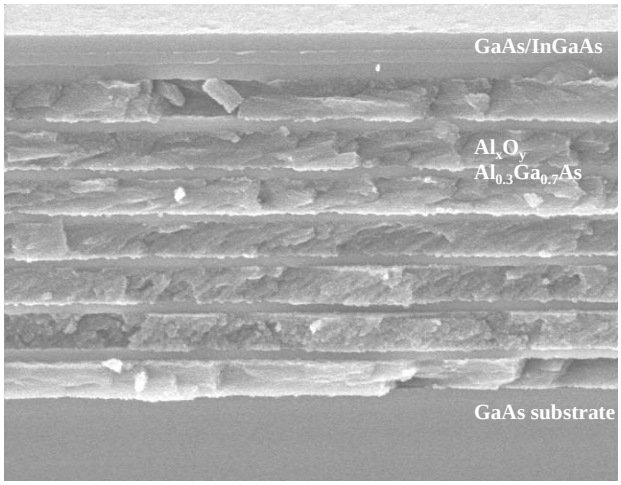

Figure 2.25 Scanning electron micrograph of fully-oxidized 500 μm mesa consisting of an $Al_{0.3}Ga_{0.7}As/Al_xO_y$ mirror and an absorbing layer designed for a Cr:Forsterite laser (side view) [63].

Five-hundred micron diameter SBRs for 800 nm, 1300 nm, and 1550 nm were designed and fabricated. The devices for 1300 and 1550 nm consist of seven pair $Al_{0.3}Ga_{0.7}As/Al_xO_y$ mirrors with a λ/2 layer of InP or GaAs on top, containing one centered $In_{0.5}Ga_{0.5}As$ quantum well or quasi-bulk absorbing layer. At 1300 nm, an SBR with a 40 nm $In_{0.5}Ga_{0.5}As$ absorbing layer placed in a λ/2 layer of GaAs has been demonstrated in a Cr:Forsterite laser, producing 30-fs pulses used for a frequency metrology experiment [65] [66]. The measured reflectivity versus wavelength is shown in Figure 2.26, taken with a microspectrophotometer. Also plotted, is the spectrum achieved with the 1300 nm SBR in the Cr:Forsterite laser (growth number R946, Kolodziejski).

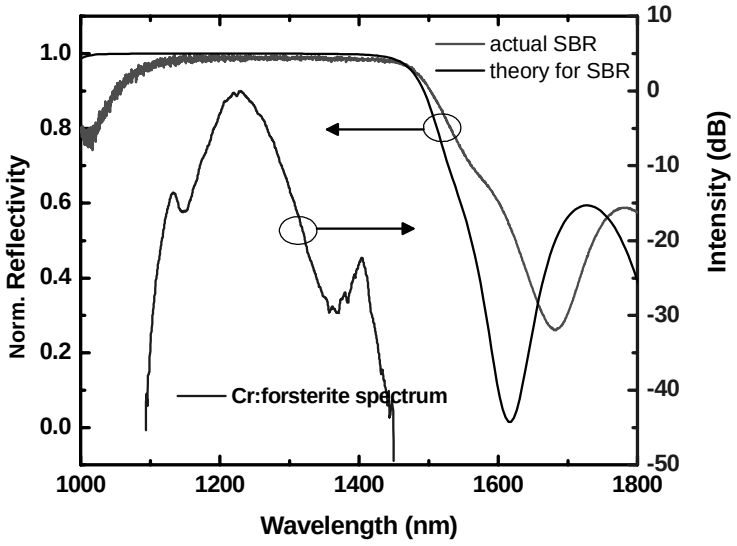

Figure 2.26 Measured and calculated reflectivity spectra for R946. A modelocked Cr:Forsterite laser spectrum achieved with the device is shown also. The structure was oxidized on 4/23/03 for 5 hrs at 410C [64][65].

In the 1.5 μm range, several different SBR devices were fabricated with varying modulation depths. Two structures were developed for the low gain Cr^{4+}:YAG laser, with relatively small modulation depths. Both have a 7-pair mirror, consisting of $Al_{0.3}Ga_{0.7}As/Al_xO_y$ layers centered at 1440 nm. In the first structure (growth number R968, Kolodziejski), a 10 nm $In_{0.5}Ga_{0.5}As$ quantum well was embedded in a λ/2 GaAs layer. Pump-probe, shown in Figure 2.27, was performed at 1550 nm. Reflectivity measurements are plotted as a function of wavelength, in Figure 2.28. The structure has a modulation depth of 0.3% and fluence behavior similar to that of the original Cr^{4+}:YAG broadband absorber. However, one may notice that the recovery time is somewhat different - 12 ps versus 40 ps of the original structure. In the GaAs/$In_{0.5}Ga_{0.5}As$-based structure (R968), the strain was concentrated in the quantum well. While the structure appears to have less delamination issues than the InP/$In_{0.5}Ga_{0.5}As$-based SBRs (i.e. R885), the strain concentrated in the quantum-well region may cause an increase in nonsaturable loss of the structure, an important consideration when designing structures for a loss-sensitive laser such as the Cr^{4+}:YAG.

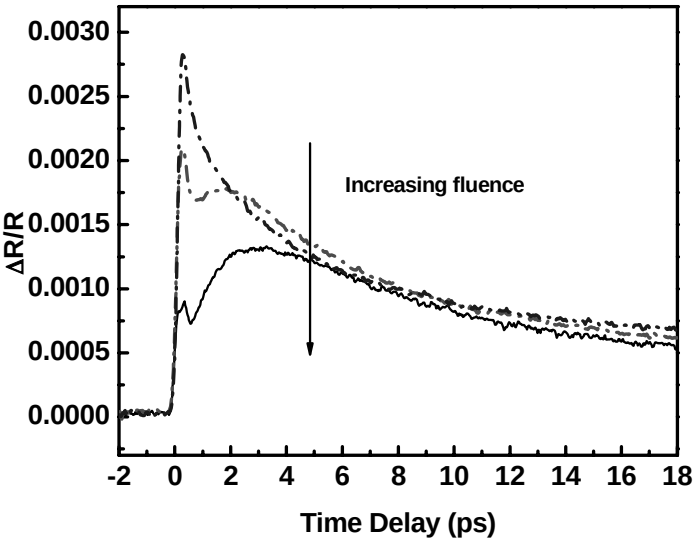

Figure 2.27 Pump-probe traces for an oxidized Cr^{4+}:YAG SBR (growth number R968). The oxidation parameters were: 410C, 4.5 hr. The sample was measured at 1540 nm.

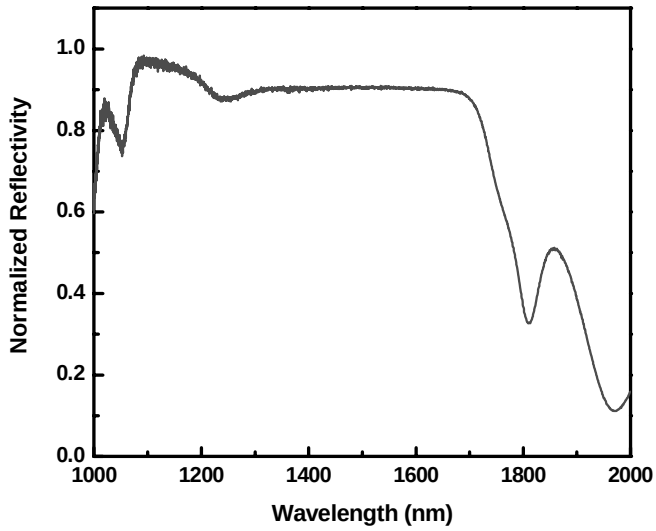

Figure 2.28 Reflectivity versus wavelength for Cr^{4+}:YAG SBR (growth number R968). The data is taken with an FTIR for a structure oxidized on 4/25/03 at 410C for 5 hrs.

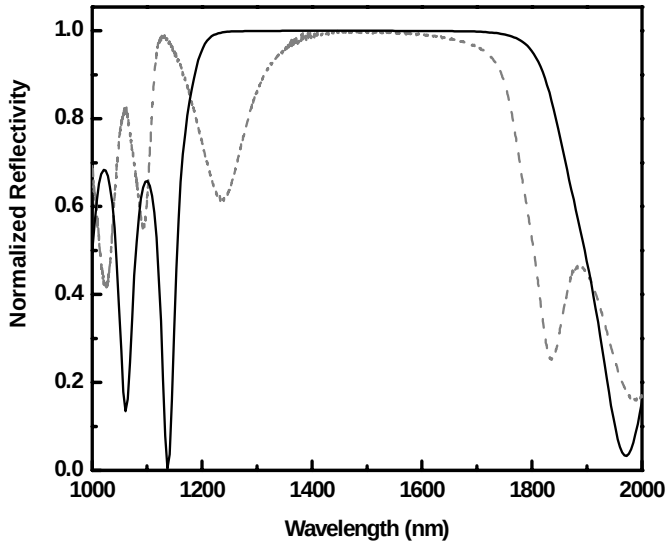

Figure 2.29 Calculated (black solid line) and measured (grey dashed line) reflectivity versus wavelength for R971. The calculated reflectivity does not include loss. When loss is included, the bandwidth is similar to the measured structure.

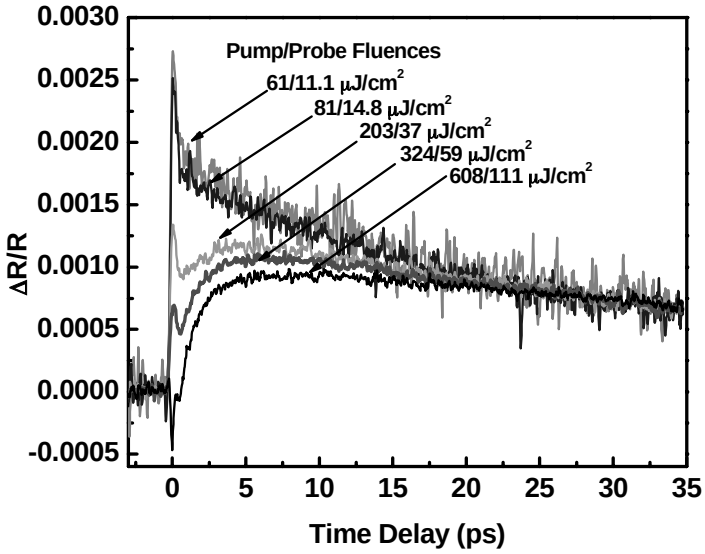

Figure 2.30 Pump-probe data for R971 versus fluence at 1540 nm. Data courtesy of H. Shen.

Two-photon absorption in an SBR can limit the achievable pulsewidth. A saturable absorber in the TPA regime acts as an inverse absorber, producing an intensity-dependent loss

opposite to that of an SBR. The higher the intensity, the more loss is produced by TPA. To mitigate these effects, one can defocus on the absorber or utilize materials with relatively small TPA coefficients. However, in order to defocus, a large area is required. The new GaAs/InGaAs-based SBR structures should suffer less from the effects of two-photon absorption than the original InP/InGaAs-based Cr^{4+}:YAG absorbers. The GaAs/InGaAs-based structures have larger usable areas of up to $1.96x10^5$ μm^2 in contrast to the $3.14x10^4$ μm^2 of the original Cr^{4+}:YAG absorber. Additionally, the new structures are constructed from materials with lower TPA coefficients (GaAs cladding layers with TPA coefficient 10 cm/GW [67] versus InP, 90 cm/GW [68]).

Additionally, an alternate structure was developed (growth number R971, Kolodziejski). It consists of a $\lambda/2$ layer of InP with a 10 nm quantum well embedded in the center on top of a seven pair $Al_xO_y/Al_{0.3}Ga_{0.7}As$ mirror. The strain in this structure is concentrated around the interface of the top $Al_{0.3}Ga_{0.7}As$ mirror layer and InP absorber cladding layer. Photoluminescence measurements indicate a bandedge of 1525 nm. Reflectivity measurements are shown in Figure 2.29, and pump-probe traces are shown in Figure 2.30.

A broadband structure at 1550 nm with larger modulation depth than the previous structures was designed and fabricated for a broadband bismuth-oxide-based erbium fiber laser. When incorporated into the bismuth-oxide laser, 155-fs pulses were produced, with the potential for shorter pulses [69]. The structure (growth number R981, Kolodziejski) consisted of a 7-layer mirror centered at 1565 nm, with a $\lambda/2$ layer of InP on top, containing six centered $In_{0.5}Ga_{0.5}As$ quantum wells. The quantum wells were placed at the center of the $\lambda/2$ region to maximize the overlap with the peak of the electric field. The large number of interfaces in this structure result in a device with more strain than the devices previously discussed. The increased strain made delamination-free oxidation more difficult. However, by ramping the temperature of the oxidation furnace before and after oxidation, 500 μm structures were successfully fabricated with minimal delamination as shown in Figure 2.31. Photoluminescence measurements determined the bandgap of the quantum wells to be 1550 nm. Pump-probe performed on the structure yielded a recovery time of 40 ps, with a maximum modulation depth of 1.3% at 1540 nm. Pump-probe traces are shown in Figure 2.32, and the reflectivity as a function of wavelength is shown in Figure 2.33. The structures were antireflection-coated with a quarter wave layer of Al_2O_3, and were proton bombarded, reducing their recovery time to about 6 ps. Proton bombardment simply introduces defects into the material, creating midgap states that speed up the recombination time [29][30].

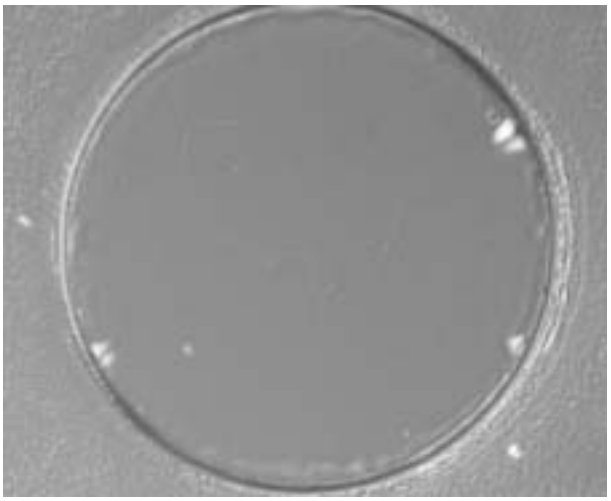

Figure 2.31 Top view of fully oxidized mesa of R981, with 6 quantum wells for a bismuth-oxide erbium-doped fiber laser (microscope image).

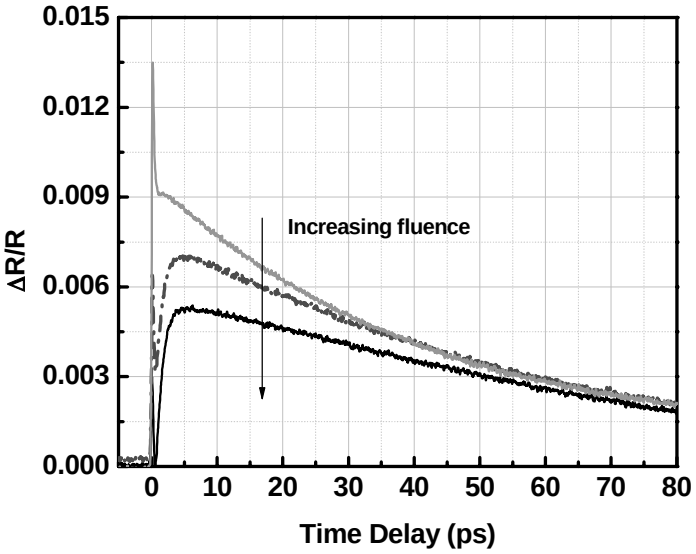

Figure 2.32 Pump-probe traces at 1540 nm on an absorber for a bismuth-oxide laser as a function of fluence (R981). The structure was oxidized at 410C for 4 hrs 45 minutes, with a 50 minute ramp on 9/10/03.

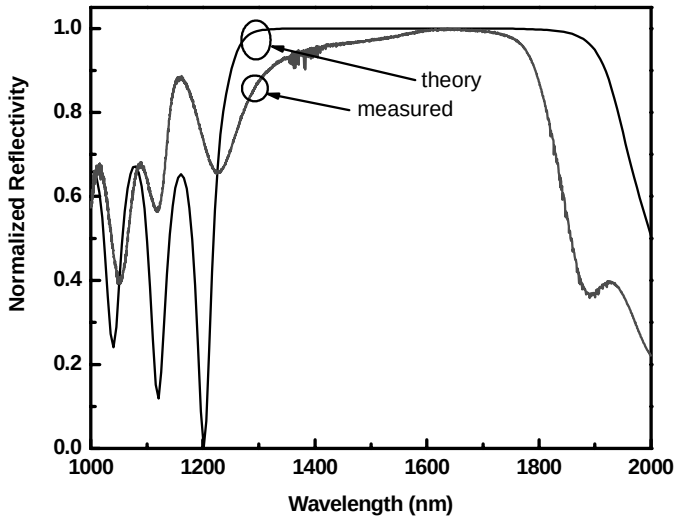

Figure 2.33 Calculated and measured reflectivity as a function of wavelength for bismuth-oxide laser SBR. The structure was oxidized at 410C for 4 hrs 45 minutes, with a 50 minute ramp on 9/10/03. The calculated reflectivity does not include absorption effects.

By simply changing the material of the high index layer of the mirror from $Al_{0.3}Ga_{0.7}As$ to InGaAlP, it was possible to fabricate an SBR for the Ti:Sapphire laser, extending the range of broadband SBR technology into the visible spectrum. Preliminary measurements indicate modelocked operation with a spectrum whose Fourier limit was 15-30 fs. The reflectivities of these 800 nm structures, along with structures designed for 1300 nm and 1550 nm are shown in Figure 2.34 [63][66]. Mirror reflectivities of all three devices span the visible to near-IR, 700 nm to beyond 1750 nm.

In summary, ultra-broadband monolithically-integrated saturable absorbers have been developed for short pulse (sub-100-fs) solid-state and fiber lasers. The devices are stable and do not appear to damage any more easily than conventional SBRs. The long term stability is good: no degradation has been observed after many months in the laboratory. Saturable absorbers with reflectivities covering the visible to infrared wavelength range were developed.

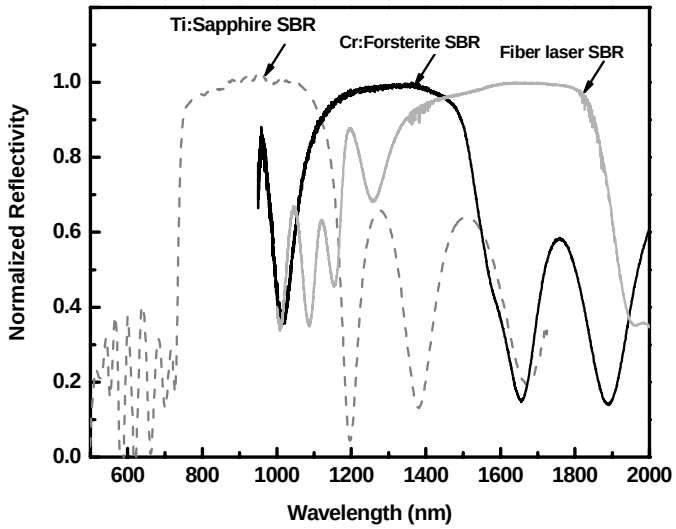

Figure 2.34 Reflectivity versus wavelength for oxidized SBRs covering the visible to the near-infrared. Absorbers for Ti:Sapphire, Cr:Forsterite, and bismuth-oxide erbium-doped fiber lasers are shown [63].

2.7 Broadband Si/Ge saturable Bragg reflectors

In addition to investigating monolithic III/V-based broadband absorbers, we have also designed absorbers based on Si/SiO_2 mirrors. Currently, a 7-pair Si/SiO_2 mirror has been integrated with a 40 nm Ge saturable absorber layer to produce a broadband silicon-based absorber that was incorporated in an Er:glass laser [70]. Pump-probe was performed at 1550 nm with 150-fs pulses.

The silicon/germanium SBR consists of a silicon/silicon-dioxide (Si/SiO_2) Bragg reflector and a germanium saturable absorber layer (Figure 2.35a). Only six layer pairs of Si/SiO_2 were required to achieve a 99% reflectivity bandwidth of 700 nm, due to the high refractive index contrast [$n(SiO_2)=1.45$ and $n(Si)=3.5$ at 1550 nm). On top of the Si/SiO_2 Bragg stack, a 40 nm germanium saturable absorber layer was embedded in a silicon layer of $3\lambda/4$ optical thickness at the center wavelength of 1400 nm. The Ge absorbing layer was placed at a peak of the standing wave pattern of the electric field.

The fabrication process is illustrated in Figure 2.35(b). The structure was fabricated on a silicon-on-insulator substrate (SOI). A layer of polysilicon is deposited, and then ther-

mally oxidized to form a layer pair consisting of a 244 nm SiO_2 layer and 100 nm of Si. This process was repeated for each of the six layer pairs. As the structure became thicker, the roughness in the topmost layers increased, which degraded the quality of the mirror. To prevent these detrimental effects, the topmost layer was bonded to a Si wafer, and the original silicon handle along with the buried oxide of the SOI substrate etched off. Thus the layers with the lowest roughness were now at the top of the structure. Because the structure was high-index contrast, incident light did not penetrate far into the structure and mirror reflectivity and bandwidth are primarily determined by the quality of the topmost layers. On top of the crystalline Si topmost layer, 40 nm of germanium were deposited by UH-CVD [71]. The germanium was passivated with a thin layer of oxide and finally, a poly-silicon cap deposited. This process ensures that the germanium layer was grown on a crystalline silicon layer and is crystalline itself. The germanium layer must be crystalline in order to ensure a high quality absorbing layer. Germanium deposited on poly-silicon is polycrystalline and has undesirable optical properties such as low nonlinearity, low absorption, and high loss. Calculated and measured reflectivity measurements of the structure are shown in Figures 2.36 and 2.37. The comparison between an as-grown structure, with the roughest layers on the surface, and a flipped mirror structure, with the roughest layers at the bottom is also shown.

The device was characterized in a series of pump-probe measurements with 150-fs pulses centered at 1540 nm from an OPO, with a pump to probe fluence ratio of 3 to 1. For fluences between 10 - 40 $\mu J/cm^2$, the germanium layer acted as a fast saturable absorber with a maximum modulation depth of 0.13% (Figure 2.38). We observed sub-picosecond recovery of the bleaching, with the temporal resolution of the measurement limited by the pulse duration. The fast relaxation process was attributed to intervalley scattering within the conduction band. It may also be the result of midgap states. In contrast, for high fluences (e.g., 300 $\mu J/cm^2$), carriers generated by TPA induced FCA, transforming the germanium layer to an inverse saturable absorber. The strong inverse saturable absorption of the Si/Ge-SBR was due to TPA in the germanium layer (β= 300 cm/GW at 1500 nm [72]) which is much greater than that of silicon or gallium arsenide [67]. Higher fluence traces, taken for a constant probe fluence, are shown in Figure 2.39. To verify that the signals observed were mainly from the 40 nm Ge layer (TPA can also occur in the Si cladding), pump-probe measurements were performed on an identical structure lacking the Ge layer (Figure 2.40). Pump-probe spectroscopy was performed for a constant probe fluence, at comparable fluences to the Si/Ge traces shown in Figure 2.39.

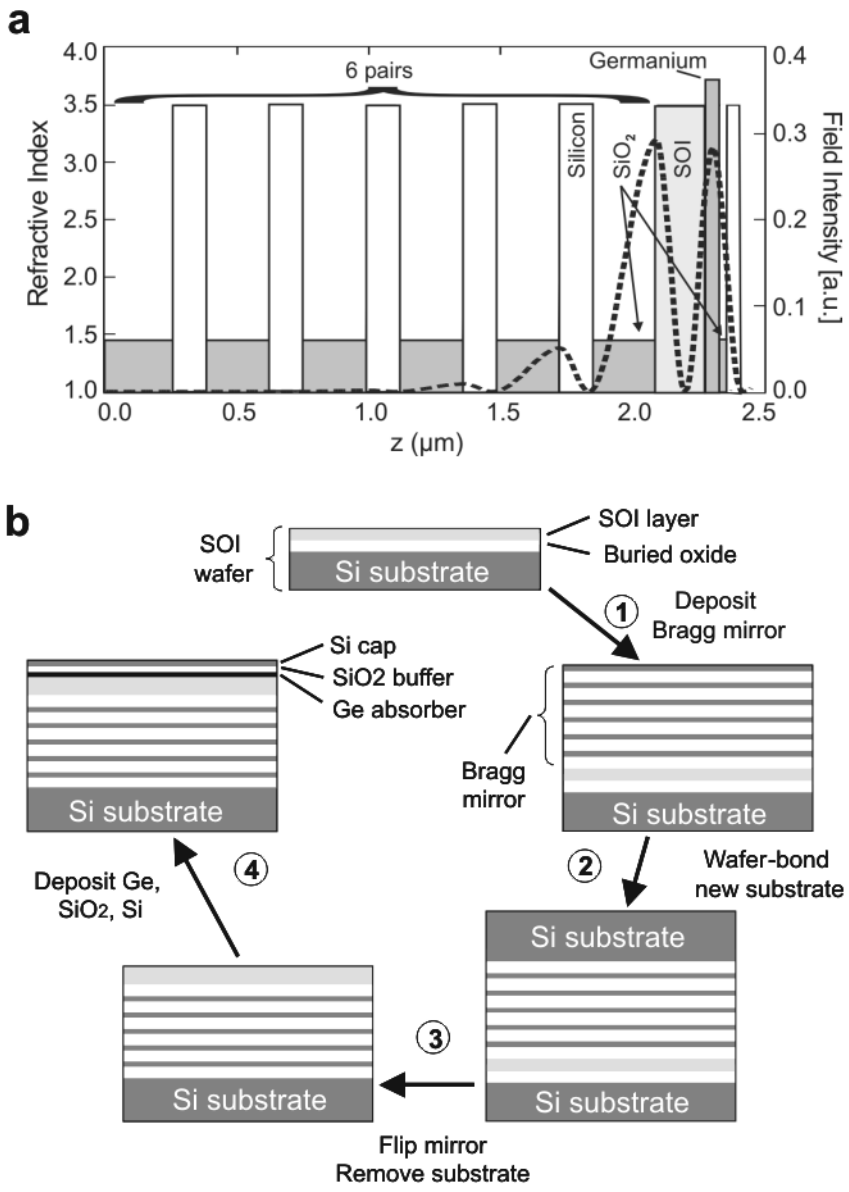

Figure 2.35 (a) Schematic of Si/Ge structure. The square of the electric field and refractive indices of the structure are plotted as a function of wavelength. (b) Fabrication steps for Si/Ge absorber [70].

The signal from TPA and FCA observed in this was an order of magnitude lower than that observed in the Si/Ge SBR. Thus, it is reasonable to conclude that the dynamics of the Ge/Si SBR are dominated by the absorption and bleaching dynamics occurring in the 40 nm Ge absorbing layer.

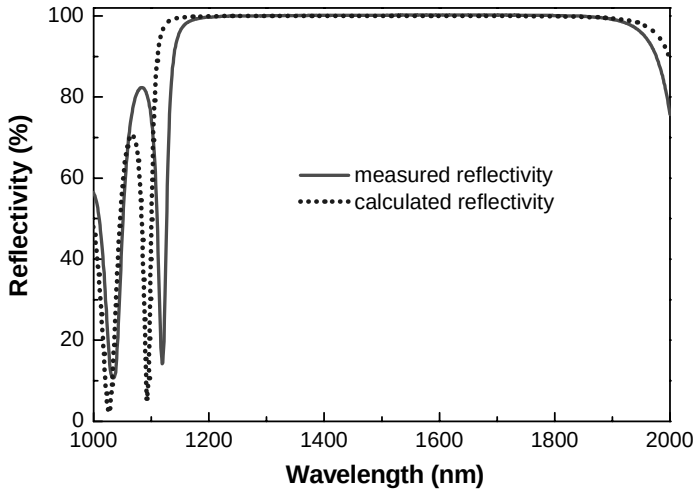

Figure 2.36 Calculated (dotted line) and measured reflectivity (solid line) versus wavelength for the Si/Ge absorber [70].

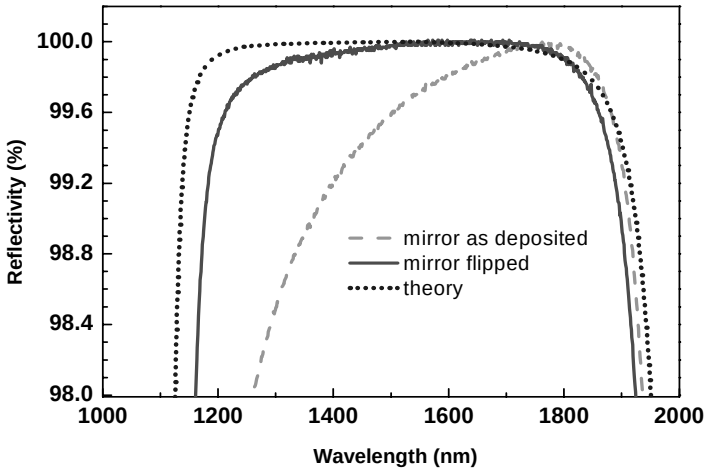

Figure 2.37 Calculated and measured reflectivity of the Si/Ge absorber (zoomed in). The reflectivity of the as-grown structure, with the roughest layers on top (dashed line) and the flipped mirror structure, with the roughest layers at the bottom (solid line) are shown [70].

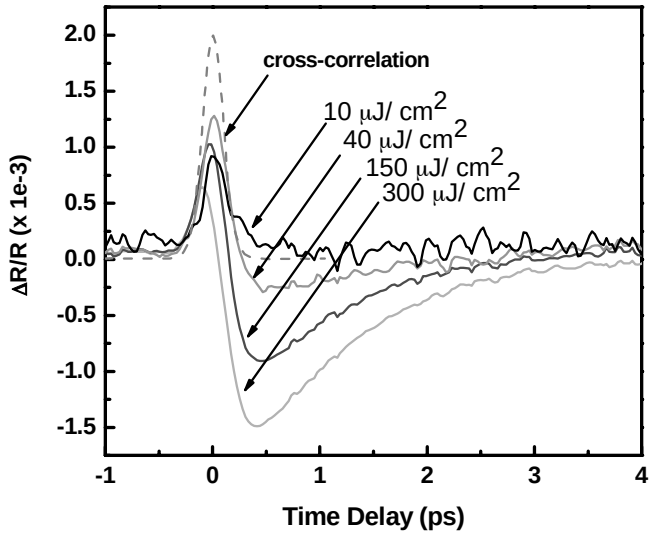

Figure 2.38 Pump-probe traces as a function of fluence for the Si/Ge absorber. The dashed line is the cross-correlation of the pump and probe pulse.

.

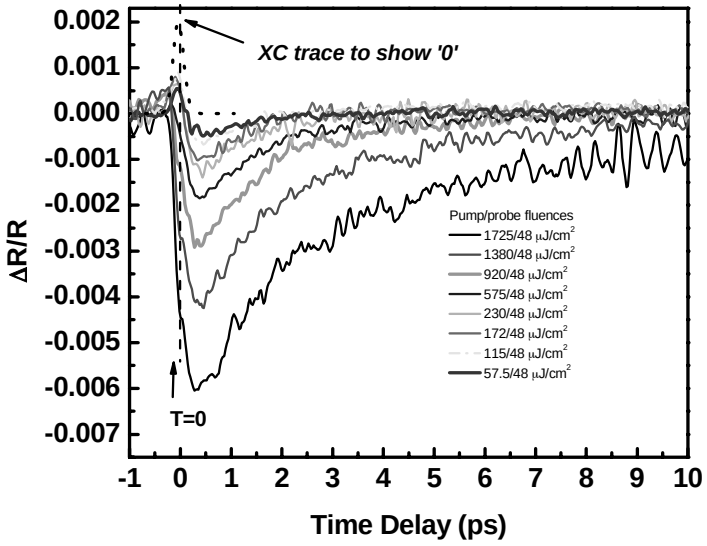

Figure 2.39 Pump-probe of Si/Ge absorber with constant probe fluence at 1540 nm.

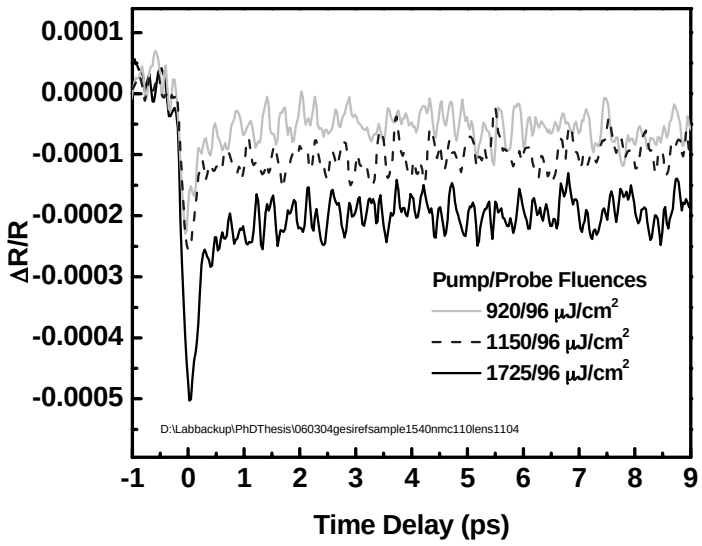

Figure 2.40 Pump-probe of structure similar to the SBR, but without the Ge layer, at 1540 nm with constant probe fluence. The signals are an order of magnitude lower than that of the SBR.

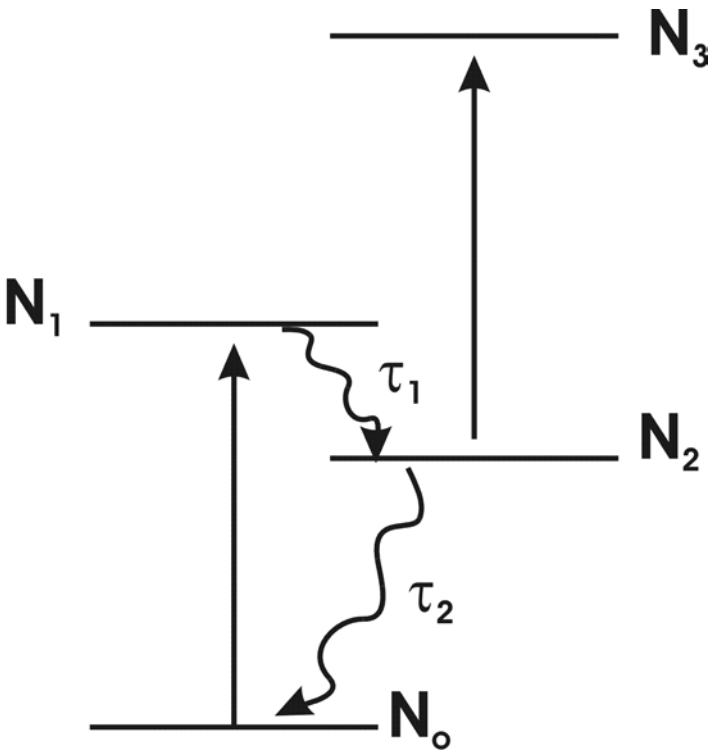

Figure 2.41 Diagram of proposed band-structure producing pump-probe dynamics in Figures 2.38 and 2.39.

We hypothesize that the Ge band structure has four levels accessible to pump and probe, producing the dynamics observed in Figure 2.41. We can now write rate equations to describe the population in each state as follows.

(2.12)

$$\frac{\partial N_1}{\partial t} = (N_o - N_1)\sigma_{01}S - \frac{N_1}{\tau_1}$$

(2.13)

$$\frac{\partial N_2}{\partial t} = \frac{N_1}{\tau_1} - \frac{N_2}{\tau_2}$$

(2.14)

$$\alpha = (N_0 - N_1)\sigma_{01} + N_2\sigma_{23} + N_o\beta_{TPA}S$$

where N_o is the population of the ground state; N_1 is the population of the state which exhibits absorption bleaching (giving rise to the positive signals in the pump-probe traces); τ_1, the lifetime of those carriers in the state; N_2 the population of the state to which the carriers from N_1 relax to; τ_2, the lifetime of this state; and N_3, the population of the highest excited state. The transition between N_2 and N_3 cannot be bleached, meaning that the lifetime in state N_3 is very short. The absorption cross-section between states *x* and *y* is denoted as σ_{xy}, and the absorption coefficient as α. *S* represents the incident photon flux and β_{tpa}, the TPA coefficient.

The Si/Ge SBR (Figure 2.35(a)) was placed in a bulk Er:Yb:glass laser. The laser crystal was phosphate glass (Kigre QX/Er) co-doped with $2.3\text{x}10^{20}$ Er-ions/cm^3 and $2.1\text{x}10^{21}$ Yb-ions/cm^3. The crystal was flat-Brewster polished and the flat end of the crystal acted as a 0.2% output coupler. The laser, a four element cavity with -0.02 ps^2 of dispersion, was pumped with a single mode 980 nm 450 mW diode. A schematic of the setup is shown in Figure 2.42(a).

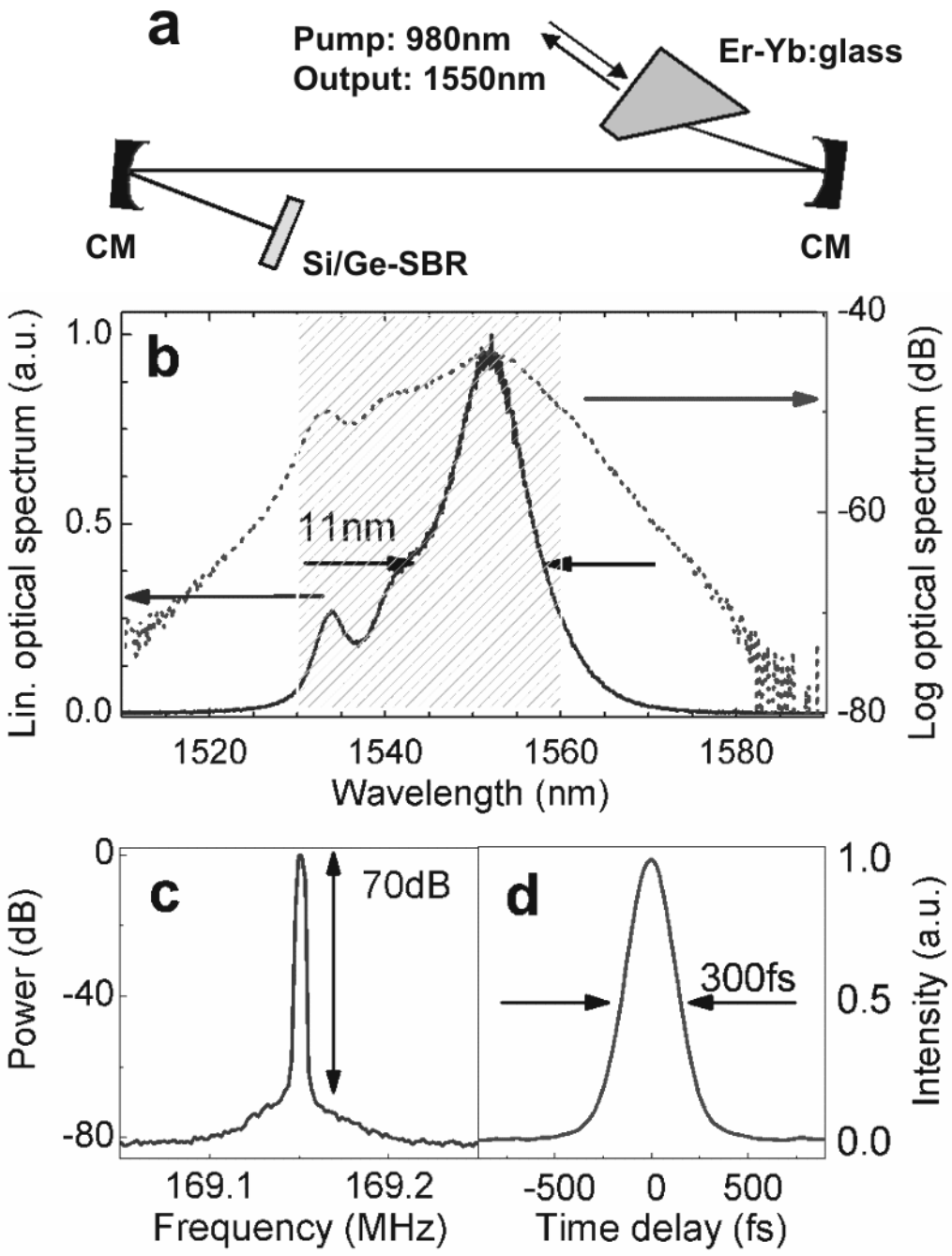

Figure 2.42 (a) Schematic of laser cavity. (b) Modelocked optical spectrum. (c) RF spectra of modelocked laser. (d) Autocorrelation [70].

The main pulse-shaping mechanism in the laser was the intensity-dependent loss of the saturable absorber. The laser produced 220-fs pulses (after external dispersion compensation), and had a spectrum with a FWHM of 11 nm centered at 1550 nm. The pump power was 360 mW, with an intracavity average power of 8.7 W. The repetition rate was 169 MHz, and no evidence of Q-switching was seen. Figure 2.42 shows a typical optical spectrum, RF spectrum, and autocorrelation. To the best of our knowledge, these are the shortest pulses obtained from an Er:Yb:glass laser to date. The previous record from a soliton modelocked laser was 380 fs [73]. From a saturable absorber modelocked Er:Yb:glass laser, the previous record was 2.5 ps pulses [74].

Ultrashort pulse generation was enabled by the high reflectivity and fast dynamics of the Si/Ge saturable absorber. No Q-switching behavior was observed regardless of pump power level despite the long upper-state lifetime and the small emission cross section of the gain medium. We attribute the high stability against Q-switching to the inverse saturable absorption in the Si/Ge-SBR at high intensity [34][41]. With bandwidth comparable to the broadband III/V absorbers presented in the previous section, this absorber may be suitable for ultrashort pulse generation in the Cr^{4+}:YAG laser system, which has a significantly broader gain-bandwidth than the Er:Yb:glass laser.

2.8 Conclusion

In conclusion, a variety of III/V and Si-based saturable absorbers have been discussed. A 16% modulation depth absorber modelocked an Er:Yb waveguide laser. Broadband oxidized monolithic broadband III/V absorbers were used to produce 32-fs pulses from a Cr^{4+}:YAG laser, 30-fs pulses from a Cr:Forsterite, and 155-fs pulses from a bismuth-oxide erbium-doped fiber laser. Finally, a broadband silicon-germanium absorber was developed, and applied to an Er:glass laser, producing 220-fs pulses.

CHAPTER 3: HIGHLY NONDEGENERATE FOUR-WAVE MIXING IN MICROSTRUCTURE FIBER

3.1 Abstract

Tapered microstructure fiber, with a nonlinearity approximately fifteen times that of single mode fiber at 1550 nm (i.e. Corning SMF-28) and an engineered dispersion profile, was used to demonstrate highly nondegenerate four-wave mixing. Frequency shifts of ~6000cm^{-1} were achieved in an 18 cm tapered microstructure fiber, using a pump at 810 nm with 100-fs pulses and a signal at 1540 nm with 150-fs pulses. Idler light was generated at wavelengths between 535 nm and 575 nm with 10% efficiency. Due to the walkoff between pump and signal pulses in the fiber, the interaction length in the tapered fiber was only 1.4 cm. Background is given in Section 3.2, and a highly nondegenerate four-wave mixing experiment is detailed in Section 3.3. The tapered microstructure fiber was fabricated and developed at OFS/ Furakawa, New Jersey by R. Windeler, C. Kerbage, and B. Eggleton. The experiments were performed in collaboration with K. S. Abedin.

3.2 Background

Four-wave mixing (FWM) can be an efficient and simple way to generate new frequency components. It occurs when photons from one or more optical waves are annihilated and new photons are created at a different frequency while conserving energy and momentum.

Four-wave mixing and other such parametric processes are caused by the nonlinear response of bound electrons to an applied optical field. When an optical field is applied, the polarization induced in the medium is nonlinear but contains terms directly proportional to the nonlinear susceptibilities, as seen below, in Equation 3.1.

(3.1)

$$P = \varepsilon_o(\chi^{(1)}E + \chi^{(2)}EE + \chi^{(3)}EEE + \ldots)$$

where P is the polarization; ε_o is the vacuum permittivity; E, the electric field; and $\chi^{(j)}$, with j = 1, 2, 3 … the *jth* order susceptibility. Third-order parametric processes such as four-wave mixing depend on $\chi^{(3)}$ and involve interaction between four optical waves. If we consider only contributions to the nonlinear polarization from $\chi^{(3)}$ and sum up four electric fields of the form:

(3.2)

$$E = \hat{x}\frac{1}{2}\sum_{j=1}^{4}\left(E_j e^{\left[i(k_j-\omega_j t)\right]} + E_j e^{\left[-i(k_j-\omega_j t)\right]}\right)$$

where k_j and ω_j represent the wavevector and optical frequency of the *jth* wave, respectively. Substituting into Equation 3.1 considering only the terms from $\chi^{(3)}$, we obtain [75]:

(3.3)

$$P_{NL} = \hat{x}\frac{1}{2}\sum_{j=1}^{4}\left(P_j e^{\left[i(k_j-\omega_j t)\right]} + P_j e^{\left[-i(k_j-\omega_j t)\right]}\right)$$

P_4 can be expressed as [75]:

(3.4)

$$P_4 = \frac{3\varepsilon_o}{4}\chi^{(3)}_{xxxx}\left\{\left[\left|E_4\right|^2 + 2\left(\left|E_1\right|^2 + \left|E_2\right|^2 + \left|E_3\right|^2\right)\right]E_4 + 2E_1E_2E_3\exp(i\theta_+) + +2E_1E_2E_3^*\exp(i\theta_-) + \ldots\right\}$$

where

(3.5)

$$\theta_+ = (k_1 + k_2 + k_3 - k_4)z - (\omega_1 + \omega_2 + \omega_3 - \omega_4)t$$

(3.6)

$$\theta_{-} = (k_1 + k_2 - k_3 - k_4)z - (\omega_1 + \omega_2 - \omega_3 - \omega_4)t$$

Four-wave mixing is caused by the terms not proportional to $|E_4|^2$ in Equation 3.4. The effect of the remaining terms in producing coupling between P_4 and E_4 is determined by θ_+ and θ_-, or similar angles.

In order to have efficient four-wave mixing, it is important that energy and momentum be conserved. Momentum, *k*, is defined as:

(3.7)

$$k = \frac{n\omega}{c}$$

From Equation 3.4, one can see that two types of four-wave mixing exist: (1) three photons transfer their energy to a single photon (2) two photons at ω_1 and ω_2 transfer their energies to two photons at ω_3 and ω_4. In the first case, if the three photons have the same frequency, the process is known as third-harmonic generation. However, it is the second case that is explored in the experiment below. In our case, the four wave mixing is partially degenerate, with $\omega_1 = \omega_2$.

For a discussion on highly nondegenerate FWM in optical fibers, it is important to understand some key properties of the medium: dispersion and nonlinearity. When light interacts with a dielectric, the medium response is usually frequency dependent. This gives rise to the frequency dependence of the index of refraction, *n*, and is known as chromatic dispersion. The propagation constant of light in a medium $\beta(\omega)$ is defined as $n(\omega)\omega/c$ and can be expanded as a Taylor series.

(3.8)

$$\beta(\omega) = \beta_o + \beta_1(\omega - \omega_o) + 0.5\beta_2(\omega - \omega_o)^2 + \ldots$$

where

(3.9)

$$\beta_m = \left(\frac{d^m \beta}{d\omega^m} \right)$$

When a pulse propagates through a fiber with dispersion, different colors travel at different speeds, as defined by β and its derivatives. A pulse envelope propagating down a fiber

will move at a group velocity of $(\beta_1)^{-1}$, while β_2 is referred to as group velocity dispersion, and causes a pulse to broaden. If n increases with frequency, the dispersion is normal, and β_2 is positive. If n decreases with frequency, the dispersion is anomalous, and β_2 is negative.

In a fiber, the dispersion has contributions from two sources: material, (chromatic dispersion), and waveguide geometry. The propagation constant in a waveguide is frequency dependent meaning that the waveguide itself is dispersive, independent of the material dispersion. Thus, in order to determine the total dispersion of a fiber one must add the material and waveguide contributions to the dispersion. In standard single mode fiber at 1550 nm, dispersion is dominated by the material contribution. A calculation of the fiber dispersion versus wavelength for standard single-mode fiber (SMF-28) is shown in Figure 3.1. The contribution of the waveguide dispersion is small in standard fiber. However, in specialty fibers such as microstructure and photonic crystal fiber, the waveguide dispersion is substantial due to the small core and high index contrast of these fibers.

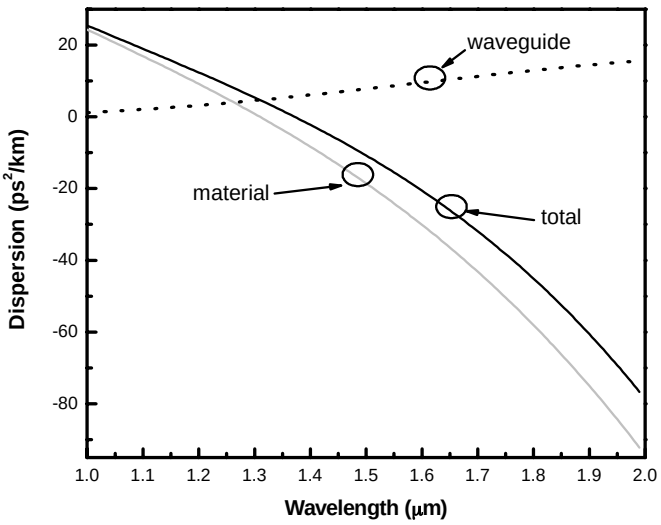

Figure 3.1 Dispersion as a function of wavelength in standard single-mode fiber. The material (solid grey), waveguide (dotted black), and resulting total dispersion (solid black) are shown.

In addition to dispersion, nonlinearity is another important fiber parameter. While $\chi^{(3)}$ is responsible for four-wave mixing, third harmonic generation, and parametric amplification, it is also responsible for nonlinear refraction. In nonlinear refraction, the index of refraction depends on intensity as:

(3.10)

$$n(\omega, I) = n(\omega) + n_2 I$$

where n_2 is the nonlinear index coefficient, and I, the optical intensity inside the fiber. One of the most common effects of nonlinear refraction is self-phase modulation (SPM), in which the pulse experiences a self-induced phase shift as it propagates down the length of the fiber of the following magnitude.

(3.11)

$$\phi = (n + n_2 I) k_o L$$

where

(3.12)

$$k_o = 2\pi / \lambda$$

and L is the fiber length; λ, the wavelength; and ϕ, the induced phase shift.

The interaction of self-phase modulation and dispersion can lead to different regimes of pulse propagation through a fiber. A pulse propagating in fiber can be described by the nonlinear Schroedinger equation [75].

(3.13)

$$\frac{dA}{dz} + \beta_1 \frac{dA}{dz} + \frac{i}{2}\beta_2 \frac{d^2 A}{dz^2} + \frac{\alpha}{2} A = i\gamma |A|^2 A$$

where α represents loss and $A(z, t)$ is the slowly varying envelope of the electric field, $E(r, t)$, written as

(3.14)

$$E(r,t) = \hat{x}\frac{1}{2}\left\{F(x,y)A(z,t)\left[e^{[i(k_o z - \omega_o t)]} + e^{[-i(k_o z - \omega_o t)]}\right]\right\}$$

where $F(x, y)$ is the spatial mode profile; ω, the frequency of the wave; and γ a measure of the nonlinearity of the fiber, defined as:

(3.15)

$$\gamma = \frac{2\pi n_2}{\lambda A_{eff}}$$

where A_{eff} is the effective area of the fiber.

Using the split-step Fourier method [75], this equation can be solved numerically with just a few lines of code. In the split-step method, the pulse is propagated through a small length segment. In the frequency domain, the effects of dispersion are analytically added to the pulse. Then, a Fourier transform is taken, and the effects of self-phase modulation on the pulse are included in the time domain.

3.3 Four-wave mixing in microstructure fiber

Four-wave mixing has many applications including wavelength conversion [75][76], phase conjugation [77], squeezing [78][79], frequency metrology [5][6][7][80], and spectroscopy [28]. In some situations, FWM can be detrimental. It can cause crosstalk between wavelength-division multiplexed channels of a communications system, causing degradation of the bit-error rates. However, FWM has been the subject of extensive research and has been demonstrated in many media including gases, semiconductors, crystals, and optical fibers. In particular, the large bandwidth, low loss, and long interaction lengths of optical fibers make them attractive for FWM.

In 1974, FWM with a frequency shift of 2800 cm^{-1} was observed in a 9-cm SiO_2:B_2O_3 clad waveguide, with a peak pump power of 100 W [81]. A frequency shift of 2900 cm^{-1} was observed in 1 m of graded index multimode fiber, in 1981 [82]. Recently, a frequency shift of 100 cm^{-1} was observed in 6.1 m of microstructure fiber, which had a small core (1.7 μm) for nonlinear enhancement [83]. Wavelength conversion of femtosecond pulses from 1.5 μm to 1.3 μm has also been demonstrated [84]. However, four-wave mixing with femtosecond pulses is made difficult by the existence of material and waveguide dispersion, which contribute to phase mismatch and group velocity differences. The advent of fiber with “engineered” dispersion and nonlinearity profiles such as microstructure fiber has mitigated these problems.

Microstructure fiber is fiber with a pattern of air holes that is able to guide light by index contrast. This fiber took the world by surprise a few years ago, with its high profile application to frequency metrology [5][6][7][80]. Microstructure fiber can be used for many nonlinear processes including supercontinuum generation, four-wave mixing, and high harmonic generation [85][86][87][88]. However, the loss of these fibers, which can be orders of magnitude higher than the 0.2 dB/km loss of conventional fiber, and the loss in coupling into them make it difficult to use them in lasers. They can also be difficult to splice with losses lower than 2-3 dB/splice due to mode mismatch.

In this work, tapered air-silica microstructure fiber with losses as low as 0.3 dB/taper (18 cm length) was used. The fiber can be spliced reliably to standard silica fiber with relatively low losses of 0.1 dB/splice [89][90]. Untapered, the fiber behaves similar to SMF; tapered, the fiber has a nonlinearity an order of magnitude higher and a unique dispersion profile. These properties enabled highly nondegenerate four-wave mixing between 800 nm and 1550 nm femtosecond pulses, the subject of this section.

The microstructure fiber used consisted of a tapered air-silica microstructure fiber (T-ASMF) and untapered air-silica microstructure fiber (ASMF) section [90][91]. The fiber used in this experiment is tapered from an outer diameter of 132 μm to an outer diameter of 10 μm, with a length of 18 cm and a core diameter of 3 μm and is shown in Figure 3.2. The untapered section was composed of a 8 μm diameter germanium-doped silica core surrounded by an undoped silica inner cladding of diameter 40 μm. The index difference between the core and cladding was approximately 0.35%. A ring of six air holes encircled the core and inner cladding, giving the fiber a grapefruit-like cross-section. Surrounding the air holes was a 14 μm ring of silica. The total diameter of the untapered fiber was 132 μm. When the fiber was not tapered, the air holes played little role in guiding the mode. Instead, the mode was guided by the index difference between the germanium-doped core and the inner cladding. The fiber was tapered by heating it in a flame with a weight attached to the end. The temperature was chosen so that the air holes did not collapse, but the fiber stretched without breaking [89]. The tapering process caused the germanium in the 8 μm core to diffuse through the entire central silica region. The mode is now guided by the index difference between the silica and air, ~0.3.

The dispersion and nonlinearity of the tapered fiber were very different from that of the untapered section. Because of the small core size in the tapered section, ~3 μm diameter, the nonlinearity of the fiber was enhanced by a factor of ~15 [90]. The large index difference between the core and cladding (air to silica) in the tapered section of the fiber, 0.3, and the small core size dramatically increase the waveguide dispersion contribution to the total fiber dispersion. The resulting unique dispersion profile of the T-ASMF allowed phase matching between highly nondegenerate waves in the lowest order mode.

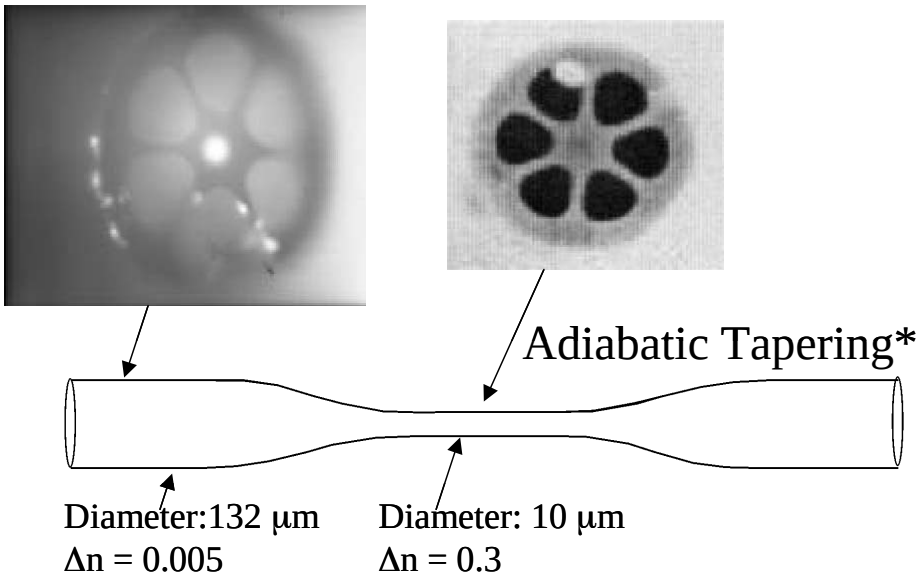

Figure 3.2 Schematic of tapered and untapered air-silica microstructure fiber [89].

Figure 3.3 shows the experimental setup. Pulses from a femtosecond optical parametric oscillator (1540 nm), the signal, and from a Ti:Sapphire laser (810 nm), the pump, were launched into a tapered microstructure fiber. Since the OPO is synchronously pumped by the Ti:Sapphire, the repetition rates of the two lasers were automatically locked. Timing jitter between the two lasers has been shown to be as low as 13 fs [92]. The fiber consisted of an 18 cm long tapered section, with short sections of untapered microstructure fiber on each side. The ASMF sections allowed light to be coupled into the core more easily than the tapered section, and can be spliced with relatively low loss. The pulses from the OPO passed through an isolator, and a variable time delay, used to adjust the relative timing of the OPO and Ti:Sapphire pulses. The Ti:Sapphire pulses also passed through an isolator, which is critical, since a backreflection from the front surface of the fiber can cause the Ti:Sapphire laser to stop modelocking (also stopping the OPO). A dichroic mirror was used to combine the OPO and Ti:Sapphire beams, which are then launched into the ASMF with an 18 mm aspheric lens. Before reaching the tapered region, the pulses propagated through a 25 cm ASMF region. The pump pulses, initially 190 fs FWHM were estimated through split-step simulations to broaden to 620 fs after 25 cm ASMF because of the fiber's normal dispersion. The signal pulses, 150 fs to start, were compressed to ~100 fs, through soliton effects (the fiber has anomalous dispersion).

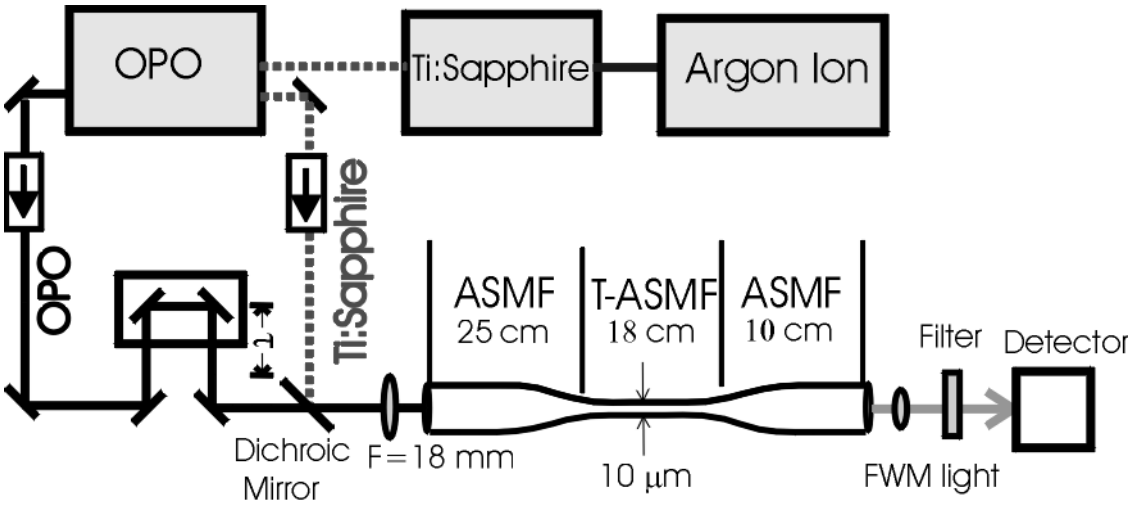

Figure 3.3 Experimental setup for highly nondegenerate four-wave mixing [91].

Maximum incident average powers on the tapered fiber were: 180 mW (pump) and 120 mW (signal). Coupling efficiencies of the signal and pump ranged from 30% to 40%. The relatively low air-to-fiber coupling efficiency was due to the differing spot sizes for the two wavelengths, and the wavelength dependence of the lens focal length and anti-reflection coating. After propagation through the T-ASMF and AMSF, the FWM idler wave was separated from the pump and signal with a color glass filter and focused onto a silicon photodetector.

The pump and signal pulses are femtosecond pulses widely separated in wavelength. As they propagate through the T-ASMF fiber, they walk-off from each other, due to differing group indices, n_g. The group index is inversely proportional to the group velocity, v_g, and directly proportional to first-order dispersion coefficient, $\beta_1(\omega)$ as follows.

(3.16)

$$\beta_1(\omega) = \frac{n_g}{c} = \frac{1}{v_g}$$

By determining the group index, the interaction length of signal and pump can be obtained. The parameters were determined in the T-ASMF and ASMF through numerical simulations. In the tapered section, we assume a step-index fiber with an index difference of 0.3 and a core diameter of 3 μm. Because the germanium-doping diffuses throughout the central silica region in the T-ASMF, the material dispersion in the T-ASMF is calculated using the Sellmeier equation of bulk silica [93]. The ASMF is assumed to have a core-cladding index difference of 0.35% and material dispersion is calculated using the parameters for Ge-doped

silica. The group index and group velocity dispersion versus wavelength for both the T-ASMF and the ASMF are shown in Figure 3.4. The calculations agree well with a measurement performed by *Ye et. al*. [94]. All calculations are performed for the lowest order HE mode in the T-ASMF. The mode propagation is solved for iteratively, and the group-index and group velocity calculated [32]. In the tapered fiber, the difference in index between the mode of the Ti:Sapphire and that of the OPO is 0.0157, giving an interaction length of 1.4 cm. The zero dispersion wavelength was estimated to be ~858 nm.

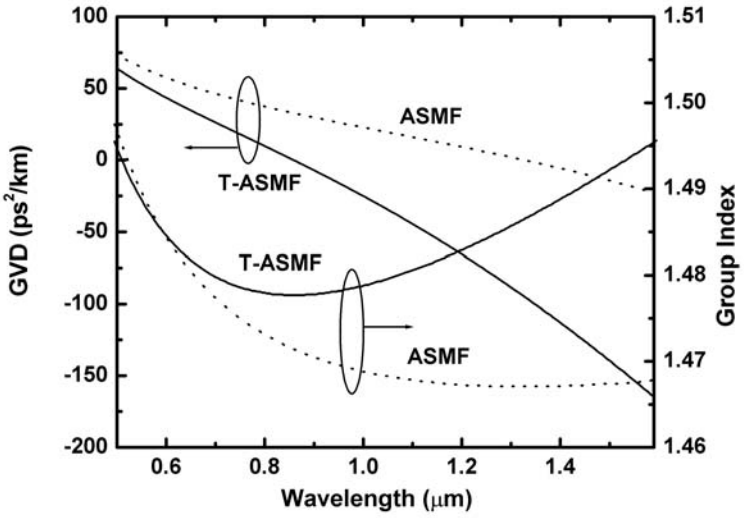

Figure 3.4 The group-velocity dispersion (left axis) and group index (right axis) versus wavelength for the tapered microstructure fiber (solid line) and untapered microstructure fiber (dotted line) [91].

When the signal pulse propagated without the pump, soliton self-frequency shifting of the input was observed. Large soliton self-frequency shifts in this fiber were observed due to the large anomalous dispersion and small third order dispersion (β_3). Soliton self-frequency shifting causes a red-shift of the pulse and is an effect induced by the pulse itself [75]. The red portion of the pulse spectrum is amplified through Raman gain that is fed by the blue components of the spectrum. Energy is transferred from the blue components of the pulse to the red components, causing a red-shift of the pulse. The result is a red-shift of the soliton spectrum that increases with propagation distance.

In the T-ASMF, third-harmonic generation (THG) from the input 1540 nm light and soliton self-frequency shifted light also occurred [87]. Because the third-harmonic was in the visible, this can be observed in the lab without room lights. As the pulse propagated progres-

sively further through the taper, the input light continued to undergo soliton-self-frequency shifting. Thus, the third-harmonic wavelength also shifted. The fiber at input glows green (THG of input 1540 nm light), then yellow (THG of 1710 nm), and finally red (THG of 1950 nm).

When the pump pulse is launched alone, self-phase modulation causes the 10 nm spectrum to broaden to 55 nm FWHM. When pump and signal propagate together, we observe idler due to FWM with wavelengths ranging from 537 nm to 575 nm. A typical optical spectrum of the idler is shown in Figure 3.5. In Figure 3.6, the signal power is kept constant and the idler power is plotted as a function of the incident pump power. The parabolic dependence clearly demonstrates the FWM process in which two photons of Ti:Sapphire are annihilated to generate one photon of idler as well as an additional signal photon. The energy relation is shown below:

(3.17)

$$\omega_{signal} + \omega_{idler} = 2\omega_{pump}$$

where ω represents the frequencies of the pump, signal and idler optical waves.

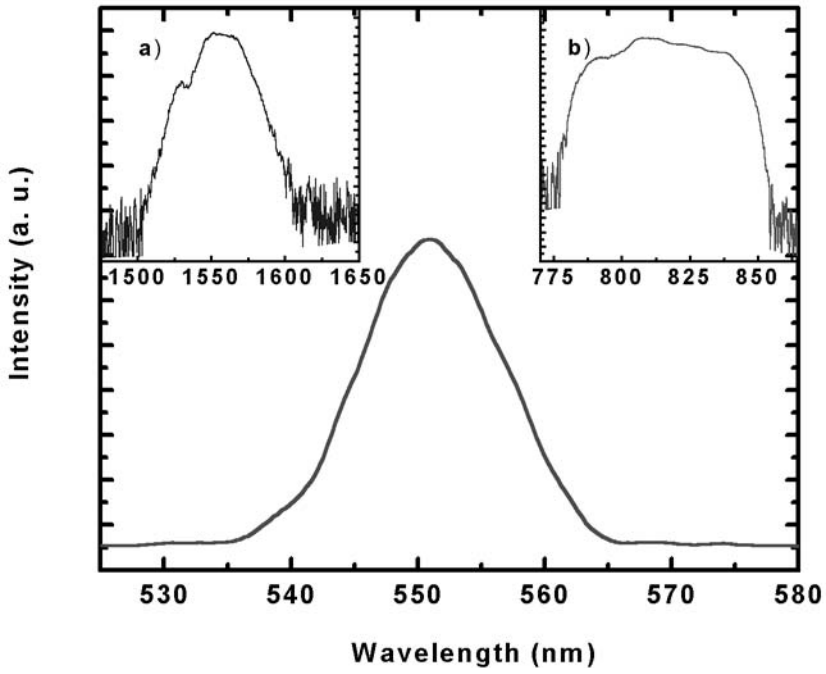

Figure 3.5 Spectrum of: inset (a) signal; inset (b) pump; and idler after propagation through 18 cm of tapered air-silica microstructure fiber [91].

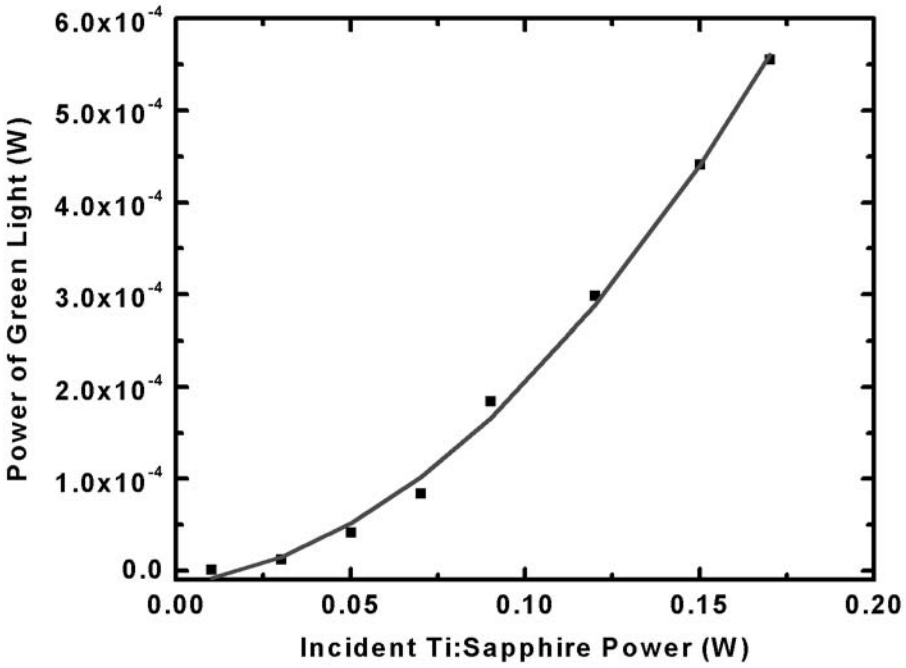

Figure 3.6 Power dependence of idler on pump power, with constant signal power [91].

With a maximum incident pump power of 180 mW and signal power of 80 mW, we were able to produce ~4 mW of idler. The coupling efficiency of the pump beam was 33% and that of the signal, 44%. The efficiency of the FWM process, defined as P_{idler}/P_{signal}, was ~10% (-10 dB). The green output power is ~9% of the maximum power obtainable, calculated from the Manley-Rowe relations of photon conservation. The idler is not constrained to the lowest order mode and may instead have converted to higher order modes, degrading the efficiency.

An expression is derived for the parametric gain coefficient of highly nondegenerate FWM following the approaches of Ref. [75], [95], and [96]. We assume an undepleted pump, a weak signal, a constant value for the nonlinear refractive index n_2, a single effective overlap integral, and no loss.

The phase mismatch in four-wave mixing is defined as:

$$\Delta k = k_3 + k_4 - k_1 - k_2 \tag{3.18}$$

where k_j is the wavevector of the *jth* optical wave defined in Equation 3.7. In this experiment, the pump waves are degenerate so $\omega_1=\omega_2$ and $k_1=k_2$. Assuming the mode over-

lap integrals are the same for the frequencies of pump, idler and signal, the coupled equations governing the amplitudes of the four waves involved can be written as:

(3.19)

$$\frac{\partial A_1}{\partial z} = \frac{in_2\omega_1}{cA_{eff}}\left\{\left[\left|A_1\right|^2 + 2\left(\left|A_2\right|^2 + \left|A_3\right|^2 + \left|A_4\right|^2\right)\right]A_1 + 2A_2^* A_3 A_4 e^{i\Delta kz}\right\}$$

(3.20)

$$\frac{\partial A_2}{\partial z} = \frac{in_2\omega_2}{cA_{eff}}\left\{\left[\left|A_2\right|^2 + 2\left(\left|A_1\right|^2 + \left|A_3\right|^2 + \left|A_4\right|^2\right)\right]A_2 + 2A_1^* A_3 A_4 e^{i\Delta kz}\right\}$$

(3.21)

$$\frac{\partial A_3}{\partial z} = \frac{in_2\omega_3}{cA_{eff}}\left\{\left[\left|A_3\right|^2 + 2\left(\left|A_1\right|^2 + \left|A_2\right|^2 + \left|A_4\right|^2\right)\right]A_3 + 2A_1 A_2 A_4^* e^{-i\Delta kz}\right\}$$

(3.22)

$$\frac{\partial A_4}{\partial z} = \frac{in_2\omega_4}{cA_{eff}}\left\{\left[\left|A_4\right|^2 + 2\left(\left|A_1\right|^2 + \left|A_2\right|^2 + \left|A_3\right|^2\right)\right]A_4 + 2A_1 A_2 A_3^* e^{-i\Delta kz}\right\}$$

where A_j is the amplitude of the *jth* wave. [Note that for our case A_1=A_2]. Also, n_2 is the nonlinear refractive index coefficient; ω_j, the frequency of the *jth* wave; A_{eff}, the mode effective area (inverse of overlap integral); and Δk, the phase mismatch, defined in Equation 3.18. Equations 3.19 and 3.20 can be solved to obtain (assuming undepleted pump waves):

(3.23)

$$A_1 = -\sqrt{P_1}e^{i\gamma_1(P_1+2P_2)z}$$

(3.24)

$$A_2 = \sqrt{P_2}e^{i\gamma_2(P_2+2P_1)z}$$

where P_j=$|A_{j,\,z=0}|^2$ and

(3.25)

$$\gamma_j = \frac{n_2\omega_j}{cA_{eff}}$$

We substituted Equations 3.23 and 3.24 into Equations 3.21 and 3.22, assuming that A_3,A_4 << A_1,A_2. We obtain:

(3.26)

$$\frac{\partial A_3}{\partial z} = 2i\gamma_3\left[A_3(P_1 + P_2) + \sqrt{P_1P_2}\,A_4^* e^{-i\theta}\right]$$

(3.27)

$$\frac{\partial A_4^*}{\partial z} = -2i\gamma_4\left[A_4^*(P_1 + P_2) + \sqrt{P_1P_2}\,A_3^* e^{i\theta}\right]$$

where

(3.28)

$$\theta = \left[\Delta k - \gamma_1(P_1 + 2P_2) - \gamma_2(P_2 + 2P_1)\right]z$$

We now introduce the variables B_3 and B_4 as follows.

(3.29)

$$B_3 = A_3 e^{-(2i\gamma_3(P_1+P_2)z)}$$

(3.30)

$$B_4 = A_4 e^{-(2i\gamma_4(P_1+P_2)z)}$$

We substitute Equation 3.29 into Equation 3.26, and Equation 3.30 into Equation 3.27. We obtain:

(3.31)

$$\frac{\partial B_3}{\partial z} = 2i\gamma_3\sqrt{P_1P_2}\,B_4^* e^{-i\kappa z}$$

(3.32)

$$\frac{\partial B_4^*}{\partial z} = -2i\gamma_4\sqrt{P_1P_2}\,B_3 e^{i\kappa z}$$

where κ is defined as:

(3.33)

$$\kappa = \Delta k + (P_1 + P_2)(-3\gamma_2 + 2\gamma_3 + 2\gamma_4)$$

We now solve Equations 3.31 and 3.32, assuming solutions of the form:

(3.34)

$$B_3(z) = \sqrt{\omega_3}(a_3 e^{gz} + b_3 e^{-gz}) e^{-i\kappa z/2}$$

(3.35)

$$B_4^*(z) = \sqrt{\omega_4}(a_4 e^{gz} + b_4 e^{-gz}) e^{i\kappa z/2}$$

We obtain the parametric gain:

(3.36)

$$g = \sqrt{\left(\gamma_{eff} P_p\right)^2 - \left(\kappa/2\right)^2}$$

where

(3.37)

$$\gamma_{eff} = \left(2\pi / \sqrt{\lambda_i \lambda_s}\right)\left(n_2 / A_{eff}\right)$$

where λ_i is the idler wavelength; λ_s, the signal wavelength; A_{eff}, the effective mode area; and $P_p = P_1 + P_2$, the peak pump power. The parameter κ is the phase mismatch

(3.38)

$$\kappa = \Delta k + 2\gamma_p P_p$$

Here, the term $2\gamma_p P_p$ is the induced pump nonlinearity with

(3.39)

$$\gamma_p = \left(2\pi / \lambda_p\right)\left(n_2 / A_{eff}\right)$$

The efficiency of four-wave mixing depends on the wavevector mismatch between the signal, idler, and pump, Δk:

(3.40)

$$\Delta k = k_s + k_i - 2k_p$$

where k_s is the signal wavevector, k_i the idler wavevector, and k_p the pump wavevector. In an optical fiber, Δk results from the bulk medium (Δk_m) and the waveguide (Δk_w). The coherence length can be defined as:

(3.41)

$$L_{coh} = 2\pi / \Delta k$$

where Δk is the maximum wave-vector mismatch that can be tolerated. If the length is less than the coherence length, significant FWM can occur.

In standard silica fiber, with an index contrast of 0.005 at 1550 nm, the wave-vector mismatch from material can be as large as 408 cm^{-1}. The waveguide contribution to the dispersion in this fibers cannot compensate the large wavevector mismatch. The wavevector mismatch from material and waveguide for FWM in standard silica single-mode fiber is plotted in Figure 3.7. However, in a large index contrast, small-core fiber such as the T-ASMF fiber, the material contribution can be compensated with the waveguide contribution. In Figure 3.8, the waveguide Δk_w, material Δk_m, and total phase mismatch, Δk, terms for T-ASMF are plotted versus signal wavelength, assuming a constant pump wavelength of 810 nm. The phase mismatch is very sensitive to the core diameter of the taper, so we have plotted the curves for T-ASMF of three different core diameters: 2.5, 3.0, and 3.5 μm. The calculations are performed using a vectorial analysis of a step-index fiber with an index difference of 0.3, and with all waves in the lowest order mode, HE_{11}. For T-ASMF fibers with diameters of ~3 μm and core-cladding index differences of 0.3, it is clear that the material contribution, Δk_m, can be compensated by the waveguide contribution, Δk_w. To improve the accuracy of the simulations, one should include the weak dependence of the effective index difference on the wavelength [97]. The fiber is not single-mode at the pump wavelength so higher order modes may also be excited, but their phase velocities do not allow phase matching. Because of the strong dependence of Δk on the core diameter, it is difficult to precisely determine the coherence length. Using the curves in Figure 3.8, we calculated the value of L_{coh} as 0.06 cm, 0.44 cm, and 0.06 cm for core diameters 2.5 μm, 3.0 μm, and 3.5 μm, respectively.

An upper bound for the maximum conversion efficiency was calculated with the formula below, from the solution of Equations 3.31 and 3.32.

(3.42)

$$\eta = \left(\lambda_s / \lambda_i\right)\left(\gamma_{eff} P_p / g\right)^2 \sinh^2\left(gL\right)$$

where λ_s is the signal wavelength; λ_i, the idler wavelength; γ_{eff} defined in Equation 3.37; P_p, the peak pump power; g defined in Equation 3.36; and L, the interaction length. This assumes an undepleted pump, a weak signal, a wavelength-independent value for nonlinearity (n_2), a single effective overlap integral, and no loss [75][95].

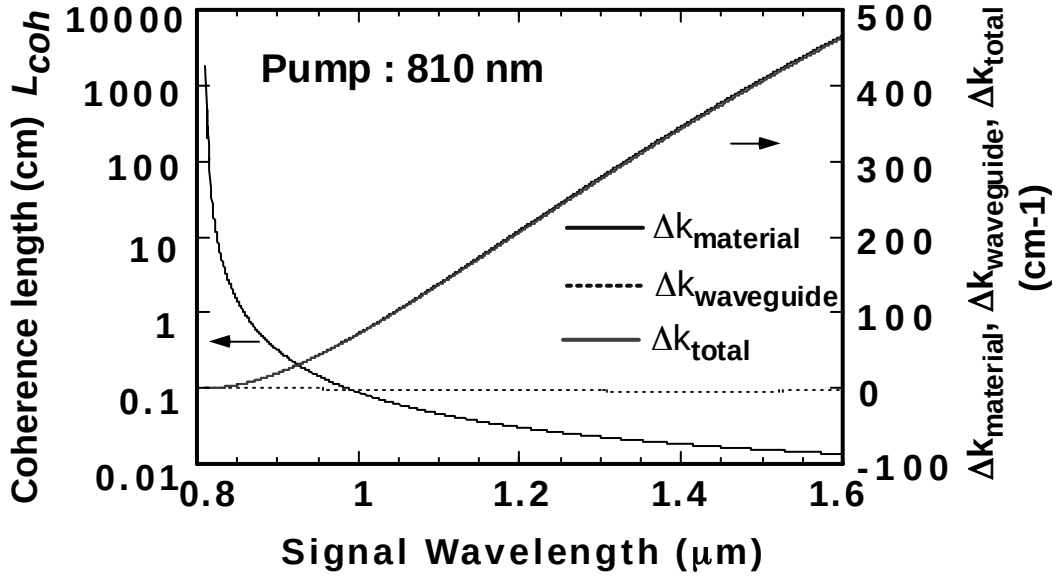

Figure 3.7 Wavevector mismatch and resulting coherence length versus signal wavelength for a constant pump wavelength at 810 nm in standard single-mode fiber.

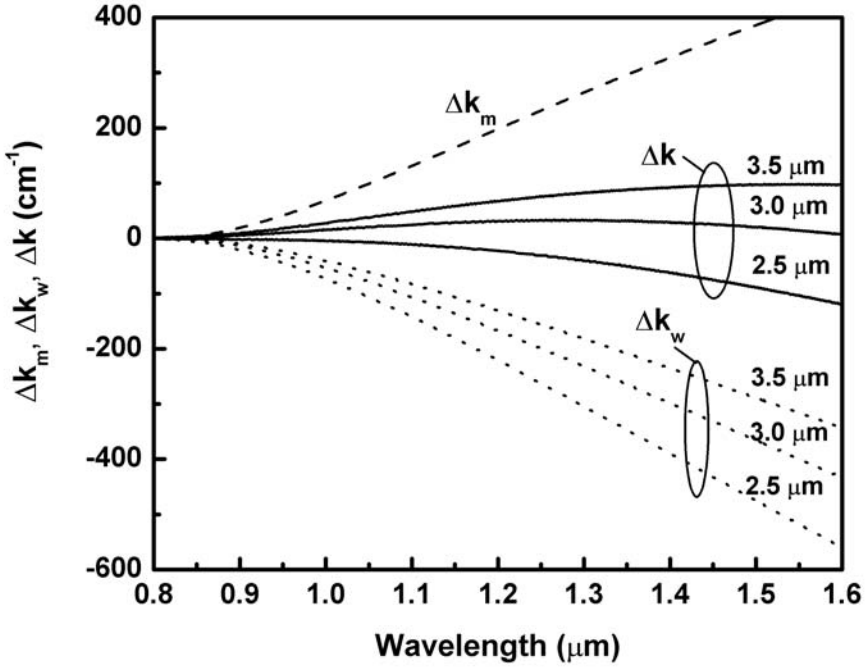

Figure 3.8 Wavevector mismatch for highly nondegenerate FWM in tapered microstructure fiber for three different core diameters 2.5, 3.0, and 3.5 μm. Contributions to the mismatch from the waveguide, material, and total dispersion are plotted versus signal wavelength. The pump wavelength is kept constant at 810 nm [91].

Using P_p = 1168 W, n_2 = 3.2 x 10^{-20} m^2/W, A_{eff} = 5 μm^2, L = 1.4 cm, and κ = 0, we calculate a maximum conversion efficiency of 168%. Because the conversion efficiency is defined as P_{idler}/P_{signal}, it can easily exceed 100%. Deviations in phase matching, uncertainty in the value of mode overlap integrals and in the value of n_2, and loss due to higher-order mode coupling and scattering probably contribute to the differences between experiment and theory. By adjusting the core diameter of the T-ASMF, further enhancements in conversion efficiency can likely be obtained.

3.4 Conclusion

In conclusion, we have demonstrated highly nondegenerate FWM with frequency shifts as large as 6000 cm^{-1} in T-ASMF fiber. A conversion efficiency of 10% was obtained in an interaction length of only 1.4 cm. This was possible because of the enhanced nonlinearity of the T-ASMF, the unique dispersion profile of the T-ASMF, and the high peak power of the femtosecond pulses used. Similar interactions in such fibers could be used for applications in squeezing, frequency metrology, and wavelength conversion.

CHAPTER 4: BISMUTH-OXIDE FIBER

4.1 Abstract

Bismuth-oxide-based fiber was investigated for amplification and supercontinuum generation. The work was performed in collaboration with Asahi Glass Company in Japan, who developed and gave us the bismuth-oxide fiber. At MIT, H. Sotobayashi, J. Sickler, and H. Shen collaborated on the experiments. Section 4.3 describes a study of the amplification properties of bismuth-oxide erbium-doped fiber (BiEDF). In a 22.7 cm piece of BiEDF, gains of 12 dB were demonstrated over an 80 nm (1520 to 1600 nm) gain-bandwidth. A passively modelocked L-band bismuth-oxide-based fiber laser is demonstrated in Section 4.4. The laser was tunable between 1570 to 1600 nm, with 288-fs pulses produced after external compression at 1600 nm. The subject of Section 4.5 is highly nonlinear bismuth-oxide fiber. The fiber was used to generate smooth unstructured supercontinuum from 1200 nm to 1800 nm. Pulse compression of 150-fs pulses to 25-fs was demonstrated with a 2-cm piece of this fiber.

4.2 Background

Glass fibers were first fabricated during Roman times, but optical fiber for communications was only developed in 1970 by researchers at Corning. In 1977, Chicago became the one of the first cities in the world to have an optical communications system. By the mid-1980's, single-mode fiber had been laid across large portions of the US for telecom traffic

[98]. With the discovery of fibers for telecom and the advent of the internet, more and more demand developed for high bandwidth systems. By the late 1990's, the telecom industry was expanding at an unhealthy rate. The bubble increased, exceeding the highest expectations, but in 2001, burst and the mad joyride was over. Today, in 2005, the telecom industry is making a slow recovery.

Information on telecom systems can be encoded in two different manners. Time-division multiplexed telecom systems (TDM) allot each channel a time slot to send and receive data. Each channel is interleaved to form the composite signal. In wavelength-division multiplexed (WDM) systems, each channel is carried by a different color of light. Thus, to be cost-effective, a high capacity WDM system requires broadband components rather than multiple narrowband devices with different center wavelengths. One major area of research is the development of broadband amplifiers and signal sources that are not simply confined to the C-band (1530 to 1570 nm) of optical communications. Several types of amplifiers that provide continuous C-band and L-band (1570 to 1620 nm) amplification have been investigated, including bismuth-oxide erbium-doped amplifiers. Additionally, a broadband source for WDM systems could be produced by spectrally splicing supercontinuum spectra. Supercontinuum is generated when high peak powers (i.e. short pulses) are injected into a length of highly nonlinear fiber. Bismuth-oxide fiber is one of many nonlinear fibers showing promise for spectral broadening. In this chapter, research on erbium-doped bismuth-oxide amplifiers and highly nonlinear bismuth oxide fiber will be presented.

Bismuth-oxide fiber is a newly developed fiber from Asahi Glass Company, in Japan [99][100][101][102][103]. It has several advantages over other types of non-standard, non-silica fiber. Bismuth-oxide fiber has a high refractive index, leading to a high nonlinear refractive index of 1.1×10^{-18} m^2/W. In contrast to chalcogenides, it does not contain any toxic elements, and is relatively easy to handle. The fiber has good mechanical and thermal stability. It can be fusion spliced [100] and has a fast response when used as a Kerr switch [99]. It can be doped with erbium to a much higher concentration than standard silica fiber, without the negative effects of concentration quenching and clustering.

4.3 Amplification properties of bismuth-oxide erbium-doped fiber

Bismuth-oxide erbium-doped fiber has a broader gain-bandwidth than conventional silica erbium doped fiber [104], with the potential to provide more efficient amplification in the L-band. The broader gain-bandwidth is a result of the high erbium concentrations possible

in the fiber. Figure 4.1 contrasts the amplified spontaneous emission (ASE) spectra of a conventional silica-based and BiEDF-based amplifier. In conventional communications systems today, separate C- and L-band erbium-doped fiber amplifiers (EDFAs) are used, but continuous amplification across several wavelength bands (ex. C- and L-band) is desirable. Amplification over several telecom wavelength bands can be achieved with newly developed rare-earth-doped fiber amplifiers using novel host materials. Thulium-doped fiber amplifiers can provide gain in the 1480-1510 nm wavelength band, allowing access to wavelengths shorter than those of conventional silica-based EDFAs [105]. Tellurite-based erbium-doped fiber amplifiers have a gain-bandwidth of 76 nm that covers not only the conventional gain band of the silica-based EDFA but also somewhat longer wavelengths [106]. Bismuth-oxide amplifiers are newly developed device that can provide amplification in both the C and L wavelength band of communications. Previous work on bismuth-oxide erbium-doped fiber amplifiers includes a demonstration of C- and L-band amplification with a cw-source [99] [100] and a study of the dispersion and amplification of 250-fs pulses at 1550 nm in a Bi-EDFA [101].

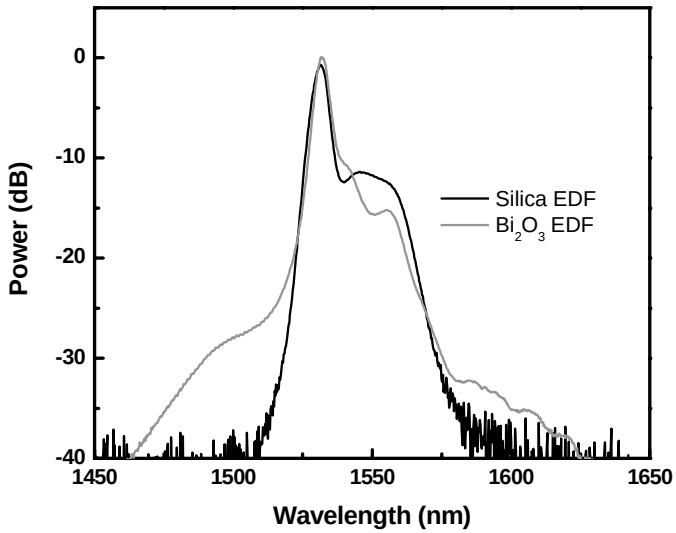

Figure 4.1 ASE spectra from a conventional silica EDF and a bismuth-oxide EDF. Data courtesy of J. Sickler.

In this work, the amplification properties of a 22.7 cm length of BiEDF (type T2M) were studied [107][108]. Key properties of the bismuth-oxide fiber are listed in Table 4.1. Figure 4.2 shows the experimental setup for amplification. To study the amplification properties of this fiber, an optical parametric oscillator was used as a signal source, producing 150-fs pulses at 82 MHz, tunable between 1.4 to 1.6 μm. The OPO was spectrally spliced with a tun-

able 4.5 nm filter, producing 1.0 to 1.3 ps pulses. These were coupled into the BiEDF through a WDM. The 22.7 cm length of BiEDF is bidirectionally pumped with two 975 nm laser diodes, producing a maximum of 260 mW each. It was important to include isolators to prevent lasing from small back reflections. The output was either sent to an optical spectrum analyzer, collimated and sent to an autocorrelator, or inserted into a power meter.

Table 4.1 Key characteristics of type T2M bismuth-oxide erbium-doped fiber.

Characteristic	**Value**
Codopants	La, B
Peak absorption @ 980 nm	127 dB/m
Peak absorption@ 1530 nm	141 dB/m
Max. background loss @ 1300 nm	< 1 dB/m
Max. loss/splice	< 1 dB/m
Numerical aperture	0.2
Mode field diameter @ 1550 nm	6 μm
Cutoff wavelength	< 1450 nm
Cladding diameter	125 μm
Coating diameter	250 μm
Refractive index of core/cladding	2.03/2.02
Erbium doping concentration	6470 ppm

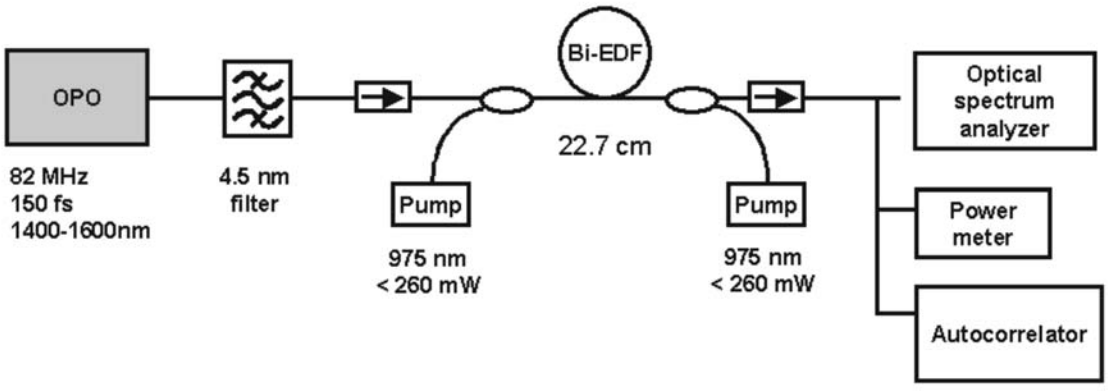

Figure 4.2 Experimental setup for studying amplification properties of BiEDF [107][108].

The gain as a function of average input power at 1530 nm is shown in Figure 4.3. The pump powers were set at 260 mW per diode. Gains as high as 17 dB were measured; an input power of 226 μW generated an output power of 11.7 mW. However, the large normal dispersion of this fiber (estimated through simulation to be 140 ps^2/km) may cause pulse distortion in BiEDFA's to be a concern. To study the effects of dispersion on pulse shape, autocorrelations were performed before and after amplification. Figure 4.4 shows several typical autocorrelations at a signal wavelength of 1530 nm. The two pumps set at 260 mW and the signal powers were varied over an order of magnitude from 55 to 562 μW. No pulse distortion is seen under small-signal or saturated amplification conditions. While the dispersion of the fiber is large, the short length of the BiEDF prevents the fiber's nonlinearity and dispersion from affecting the signal pulses.

Figure 4.5 shows the gain versus signal wavelength for a signal power of 70 μW and pumps powers set at 260 mW per diode. Gains of greater than 12 dB were observed over the entire 80 nm range and gains greater than 20 dB were observed between 1530 - 1555 nm. The gain peak is at 1530 nm. The pulsewidth and spectral width versus wavelength before and after amplification are shown in Figures 4.6 and 4.7. Over the entire wavelength range, there was very little change in pulsewidth from input to output. Self-phase modulation at 1530 and 1535 nm causes the variation in spectra width.

In order to perform picosecond pulse amplification with conventional silica-based EDFA's, the dispersion of the fiber must be compensated. Conventional EDFA's are often tens of meters long, causing the accumulated dispersion to be large and the pulses to broaden. However, because Bi-EDF lengths can be only tens of centimeters, picosecond signals can be amplified without pulsewidth broadening over a large wavelength range.

In conclusion, ps-pulse amplification has been demonstrated over an 80 nm bandwidth (1520 - 1600 nm) in a 22.7 cm length of Bi_2O_3-based EDF. The pulses are not distorted over the entire 80 nm bandwidth, making this a suitable fiber for high bit rate telecommunication applications spanning the C- and L-bands.

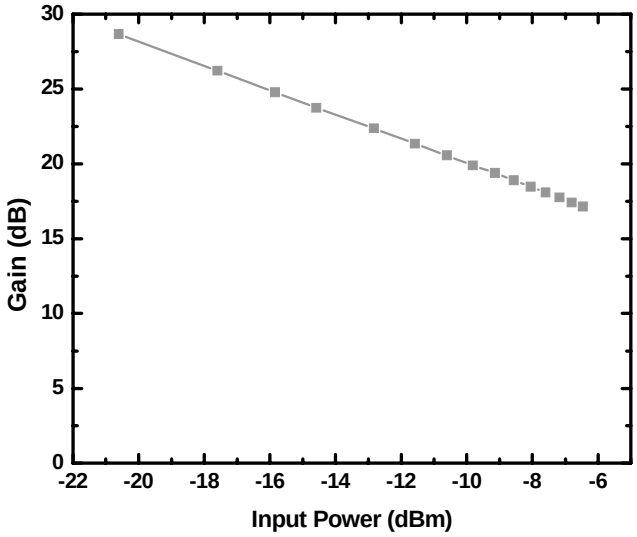

Figure 4.3 Gain as a function of input power at 1530 nm [107][108].

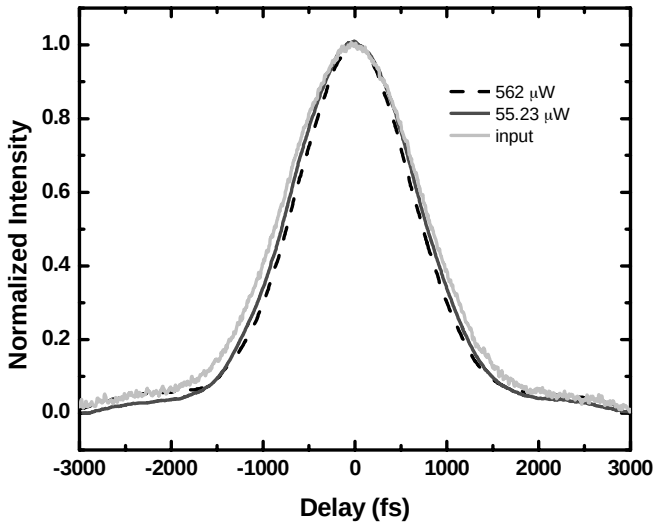

Figure 4.4 Autocorrelations before and after amplification as a function of input power for pump powers of 260 mW/diode [107][108].

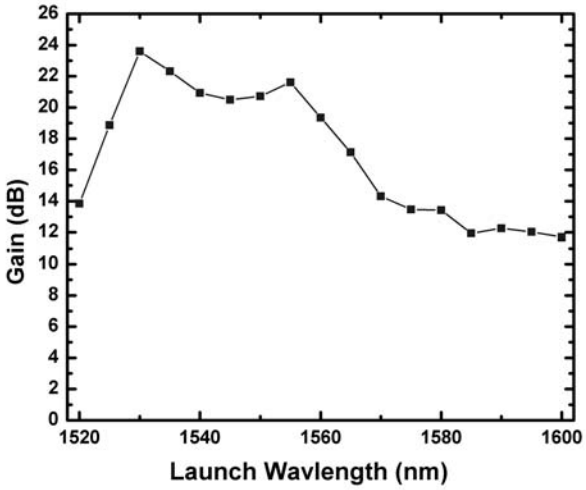

Figure 4.5 Gain versus wavelength for a constant input signal power of 70 μW [107][108].

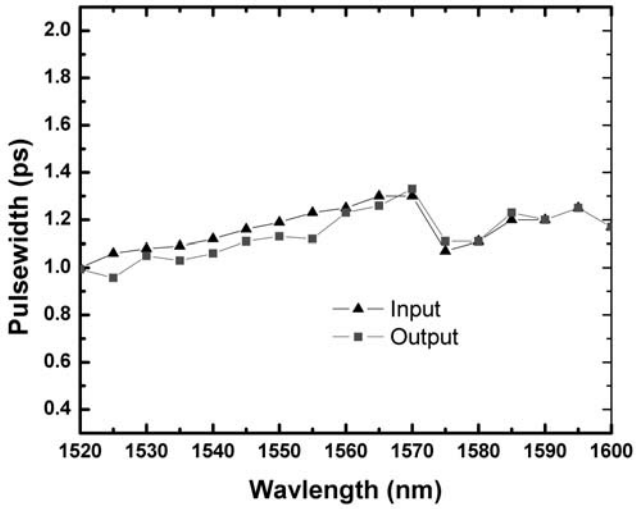

Figure 4.6 Input and output pulsewidth versus wavelength for an input signal power of 70 μW. The step at 1575 nm is caused by a filter change [107][108].

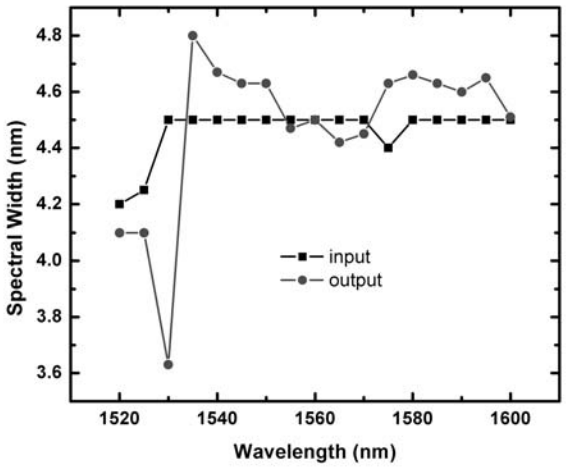

Figure 4.7 Input and output spectral width versus wavelength for an average input power of 70 μW [107][108].

4.4 Passively modelocked L-band bismuth-oxide fiber laser

L-band laser sources are of interest for high volume WDM telecommunications systems. A solution can be offered by bismuth-oxide erbium-doped fiber, with gain in the C- and L-band. It is possible to construct an L-band laser from a conventional silica-based EDFA, with a careful balance between fiber length, erbium doping concentration, and pump power [109]. However, construction of an L-band laser from bismuth-oxide fiber is simplified by the broad gain-bandwidth and high gain of BiEDF. In this section, an L-band modelocked laser incorporating bismuth-oxide erbium-doped fiber and an SBR is discussed [110].

A schematic of the laser cavity, constructed in a linear configuration, is shown in Figure 4.8. A 55.6 cm length of fiber (Type T2M, Asahi Glass Company) was used as the gain medium for the L-band fiber laser. Two WDMs allowed bi-directional pumping of the bismuth-oxide erbium-doped fiber with two 975 nm laser diodes. One end of the cavity was formed by a Faraday rotator mirror. On the other side of the gain medium, light passed through a 10% output coupler, a collimator, a 15 nm tunable filter, 2 waveplates, and an aspheric lens which focused onto a saturable absorber, acting as the other cavity end mirror. The high doping of erbium in the 55.6 cm BiEDF, 6470 ppm, allowed for sufficient gain in the L-band. The BiEDF was fusion spliced to standard silica fibers, with a loss per splice of less than 1 dB. The mode field diameter at 1550 nm was 6 μm, the maximum background loss at 1300 nm, less than 1 dB, and the cutoff wavelength shorter than 1450 nm.

A semiconductor saturable absorber was used as the modelocking mechanism for the laser. Since the cavity dispersion was normal, soliton effects did not play a role. The saturable absorber consisted of a 22-pair Bragg mirror grown by MOCVD containing alternating layers of AlAs/GaAs (Growth number R730, Kolodziejski, nickname: 'SBRV'). On top of this, an absorbing layer and cladding region were grown by gas-source molecular-beam epitaxy. These layers consisted of a half-wave layer of InP containing six centered $In_{0.5}Ga_{0.5}As$ quantum wells, with a bandedge of ~1580 nm. In order to reduce the recovery time, the sample was proton bombarded with 10^{14} protons/cm^2 at an energy of 40 keV [29]. This introduced mid-gap states into the material, speeding up the recombination time. To increase the modulation depth, the structure was anti-reflection coated with a $\lambda/4$ layer of Al_2O_3. The modulation depth was ~5%, the recovery time ~3 ps, and the saturation fluence ~3.5 μJ/cm^2. A schematic of the absorber structure is shown in Figure 4.9 and typical pump-probe traces are shown in Figure 4.10.

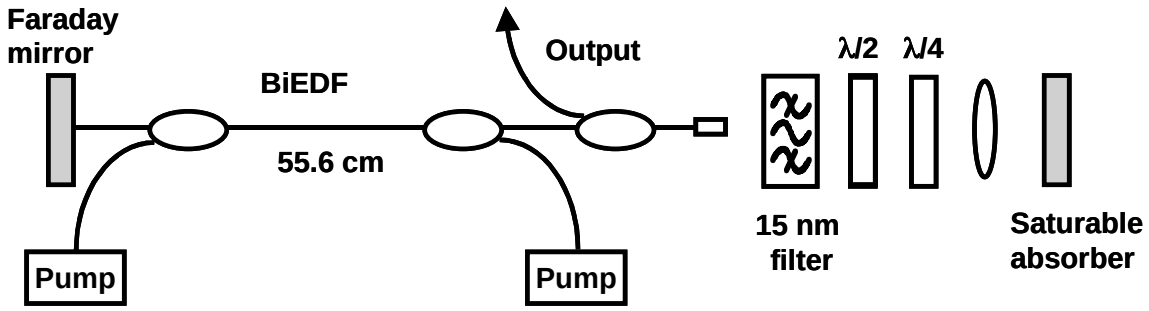

Figure 4.8 Schematic of laser cavity for L-band modelocked bismuth-oxide laser [110].

The laser was tuned with an optical filter and modelocked at center wavelengths from 1570 to 1600 nm. In Figure 4.11, modelocked spectra of the laser at 3 different wavelengths 1570, 1586, and 1600 nm are shown, with spectral widths from 9.1 to 9.8 nm. Sampling oscilloscope traces are shown at these wavelengths in Figure 4.12. An RF spectrum is shown in Figure 4.13, with the fundamental at 16.56 MHz, and 60 dB of noise suppression. The laser pumps were set to 255 and 168 mW, in order to achieve fundamental modelocking and avoid multiple pulsing [111]. The output powers when the laser was at the fundamental repetition rate were 596 mW at 1570.0 nm, 421 mW at 1586.0 nm, and 340 mW at 1600.1 nm, respectively. Autocorrelations, shown in Figure 4.14, measured pulsewidths directly from the laser of 2.20 ps at 1570.0 nm, 2.26 ps at 1586.0 nm, and 2.16 ps at 1600.1 nm.

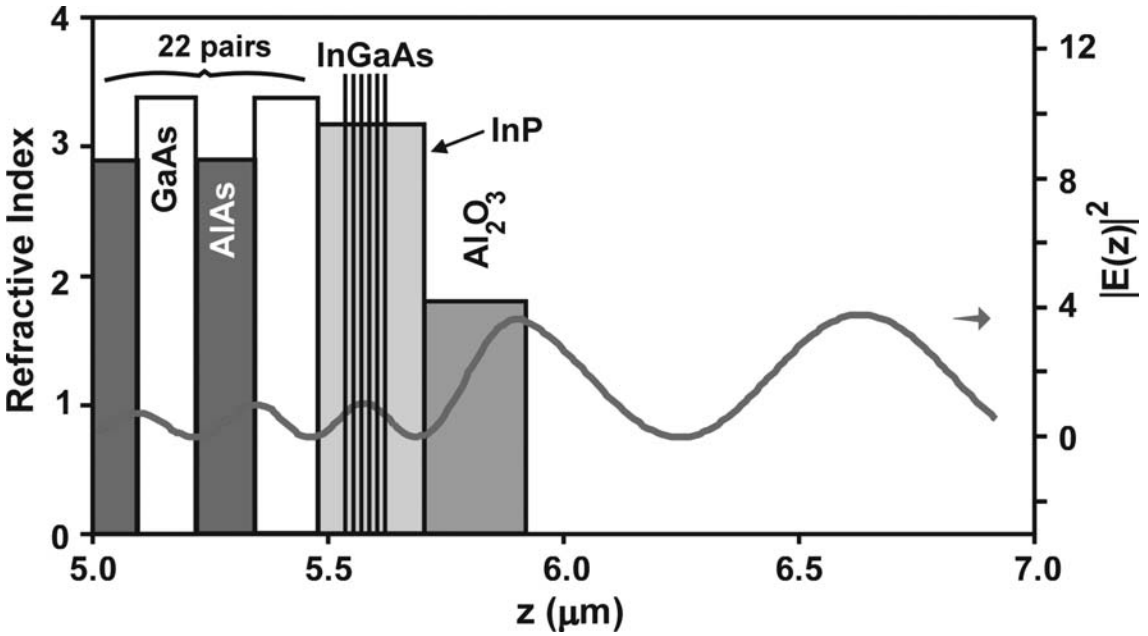

Figure 4.9 Refractive index and square of the electric field as a function of position for the SBR used in the L-band laser [110].

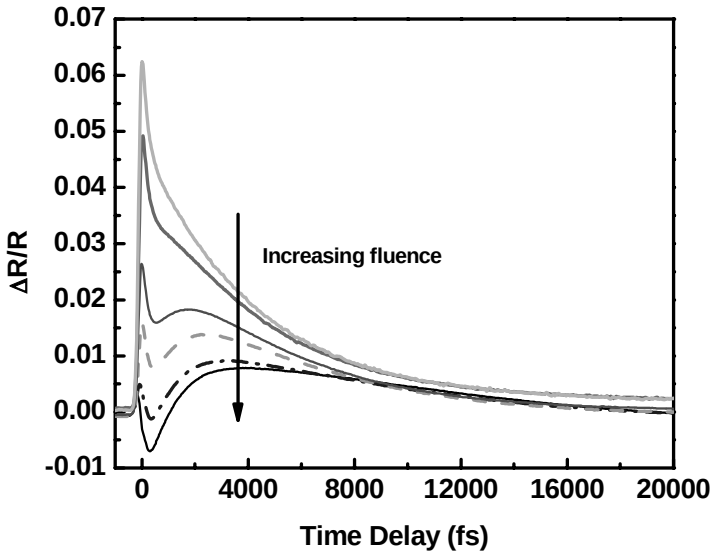

Figure 4.10 Typical pump-probe traces as a function of fluence at 1540 nm for the absorber used in the L-band laser (SBRV, antireflection-coated, 10^{14} protons/cm^2, 40 keV).

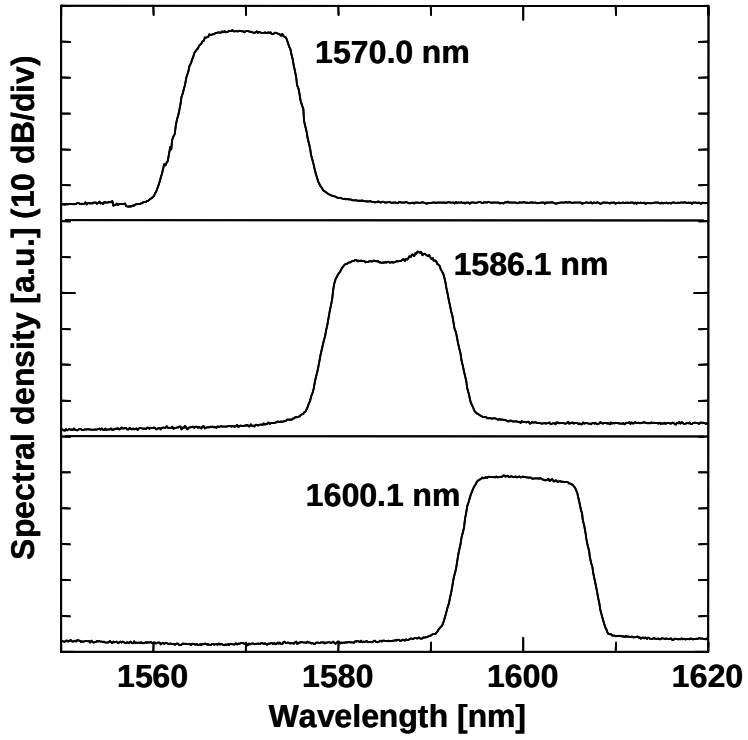

Figure 4.11 Modelocked spectra from L-band BiEDF laser at wavelengths of 1570.0 nm, 1586.1 nm, and 1600.1 nm [110].

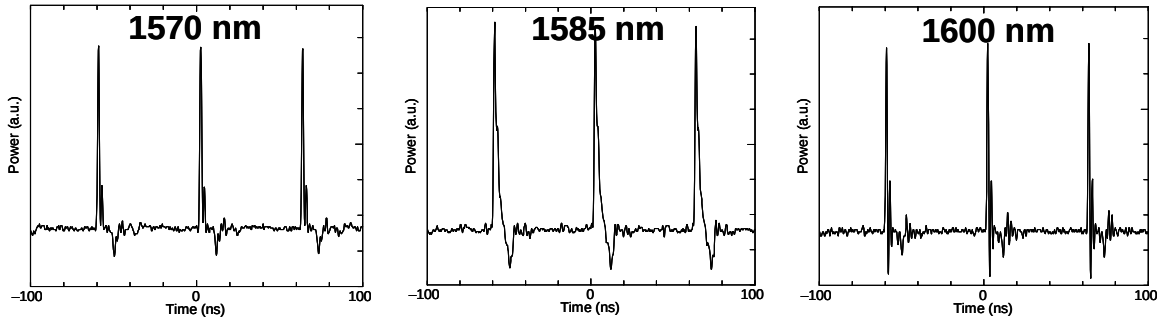

Figure 4.12 Sampling oscilloscope traces of modelocked operation at 1570 nm, 1585 nm, and 1600 nm [110].

The pulses exiting the laser are chirped. By externally compensating the dispersion with 100 m of large-area non-zero dispersion shifted fiber (dispersion of -0.0356 ps^2 at 1600 nm), pulses were compressed to 288 fs at 1600 nm, yielding a time-bandwidth product of 0.35, assuming a sech-shaped pulse.

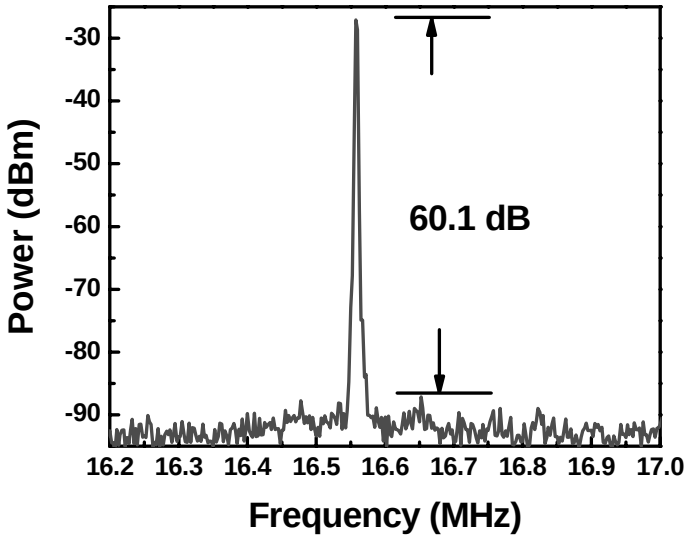

Figure 4.13 RF spectrum of modelocked L-band laser at 1600 nm [110].

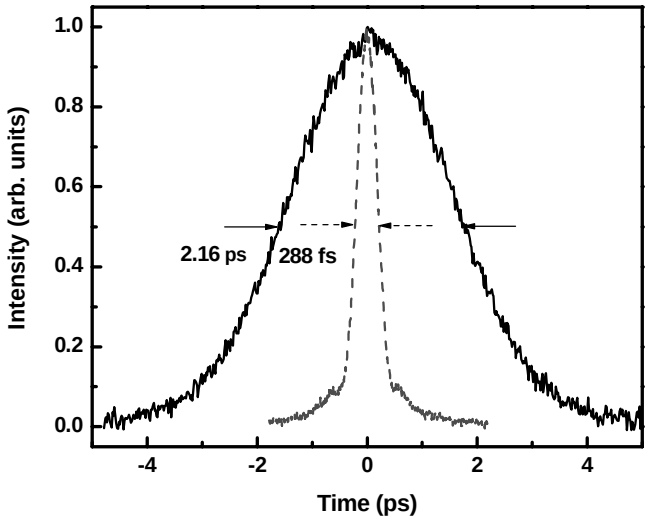

Figure 4.14 Autocorrelation of the laser output (pulsewidth of 2.16 ps), and after external chirp compensation (pulsewidth of 288 fs) at 1600 nm [110].

In conclusion, a passively modelocked L-band fiber laser tunable between 1570 to 1600 nm was demonstrated. It generated a 16.56 MHz, 2.2-ps pulse train. With external dispersion compensation, transform-limited 288-fs pulses were produced at 1600 nm. These

results are promising for applications in telecommunications, photonic processing, and optical sensing that utilize the L-band of optical communications.

4.5 Highly nonlinear bismuth-oxide fiber for smooth spectral broadening and pulse compression

The subject of this section is highly nonlinear bismuth-oxide fiber. In the past few years, there have been significant advances in the fabrication of highly nonlinear fiber. After the enabling technology of photonic crystal and microstructure fibers was developed, the field of frequency metrology was born in 2000 [5][6][7][80]. Such fibers enabled laser spectra to be broadened to an octave external to a laser cavity, allowing for phase-stabilized lasers, and their high profile application, metrology. In addition, broad spectra, or supercontinua, have many applications such as medical imaging [9], characterization of broadband devices [112][113], pulse compression [114], spectroscopy [8], and communications systems.

These applications sparked a great deal of research dealing with nonlinear fibers such as photonic crystal fibers [115][116], microstructure fibers [88], and other highly nonlinear solid-core fibers [117][118][119][120]. The nonlinearity of such fibers results from small core sizes (enabled by high-index contrast) and in some cases, material composition. These fibers often have unique dispersion profiles resulting from the contribution of waveguide dispersion to the total fiber dispersion. In contrast, standard single-mode fiber at 1550 nm has a dispersion profile dominated by that of the material, shown in Figure 3.1. In this section, an alternative to microstructure and photonic crystal fiber will be presented: solid-core highly nonlinear, normally dispersive bismuth oxide fiber. Its application to supercontinuum generation and pulse compression will be discussed [120].

Broad spectra, or supercontinua, can be produced with ultrafast modelocked lasers or highly nonlinear fiber. At 1550 nm, 20-fs pulses have been produced from a Cr^{4+}:YAG laser, with a spectrum corresponding to 190 nm FWHM [44]. An optical parametric amplifier stretcher/compressor system has been used to generate 14.5-fs pulses at the same wavelength [121]. Twenty-fs pulses were generated by a semiconductor laser, producing 1-ps pulses at 2 GHz, followed by four stages of soliton compression [122]. A less complex solution is offered by highly nonlinear, normally dispersive fiber such as nonlinear bismuth-oxide fiber.

In fiber, there are several techniques for supercontinuum generation. The broadest spectra are generated in anomalous dispersion fiber, but they are often noisy and structured due to modulation instability, pulse breakup and other nonlinear effects [123]. Spectral broad-

ening in normal dispersion fiber offers a nice alternative. In normal dispersion fiber, modulation instability and pulse breakup do not occur. The result is smooth, unstructured spectra, with broadening ultimately be limited by dispersion [123][124]. Bismuth-oxide-based glass fiber is a newly developed fiber with sufficiently high nonlinearity to permit stable supercontinuum generation at low powers under conditions of normal dispersion [102][103].

Spectral broadening in a normal dispersion fiber will be governed by the ratio of $(L_d/L_{nl})^{0.5}$, where L_d is the dispersive length, and L_{nl}, the nonlinear length [114][124]. The dispersive length can be written as

(4.1)

$$L_d = \tau_o^2 / \beta_{av}$$

where τ is the pulsewidth parameter and β_{av} is the average second-order dispersion. The nonlinear length is defined as

(4.2)

$$L_{nl} = 1 / \gamma P_o$$

where P_o is the peak power of the input excitation, and γ, the nonlinear index coefficient. Thus,

(4.3)

$$\sqrt{L_d / L_{nl}} = \sqrt{(\tau_o^2 P_o \gamma) / \beta_{av}}$$

The nonlinearity of the fiber, γ, is defined in Equation 3.15. By increasing the nonlinear index coefficient, γ, of the fiber, or by using pulses with high peak powers, spectral broadening can be improved. The use of a material with a large nonlinear index coefficient or a reduction in fiber effective area will also increase the nonlinearity. Dispersion will limit the maximum amount of spectral broadening possible, but the use of highly nonlinear fiber mitigates these effects. Although normal dispersion hinders spectral broadening, the supercontinuum generated in normal dispersion fiber is smooth and controlled.

The highly nonlinear bismuth-oxide fiber used in these experiments has a nonlinearity of 1100 $(W\text{-}km)^{-1}$ +/-15%. The fiber shares many properties of photonic crystal and microstructure fibers, but in a solid-core geometry. The small effective area of the fiber, 3.3 μm^2, and high nonlinear refractive index coefficient of the bismuth-oxide glass, 1.1 x 10^{-18} m^2/W, produce a very high nonlinearity, about 500 times that of standard dispersion-shifted single-mode fiber. The refractive index of the core was 2.22, and that of the cladding 2.13. The

high-index contrast makes the small core size of the fiber, 1.7 μm, feasible. The refractive index of the core is increased by doping it with In_2O_3. Adding In_2O_3 also increases the difference in glass transition temperature and crystallization temperature for the material, which is important for fabrication. A cross-section of the fiber is shown in Figure 4.15 [125].

The refractive index of the core versus wavelength is plotted in Figure 4.16. The dispersion relation is below [125][126].

(4.4)

$$n = \sqrt{a + \frac{b\lambda^2}{\lambda^2 - c} + d\lambda^2}$$

with a = 1.0, b = 3.93225, c = 0.04652, and d = -0.00796.

A simulation of the fiber dispersion is shown in Figure 4.17, with contributions from the material and waveguide plotted separately. The dispersion of the fiber is calculated for the lowest order HE mode, assuming a step-index fiber with a core-cladding index difference of 0.09. The mode propagation constant is solved iteratively and the mode index and dispersion of the fiber [32] are calculated in turn. The small core size and high-index-contrast of the fiber lead to a substantial contribution from the waveguide dispersion. Thus, the dispersion of the waveguide balanced that of the material resulting in relatively flat total dispersion between 1200 to 1800 nm. The simulation result was fairly close to the measured dispersion of the fiber at 1550 nm, -250 ps/nm/km [103].

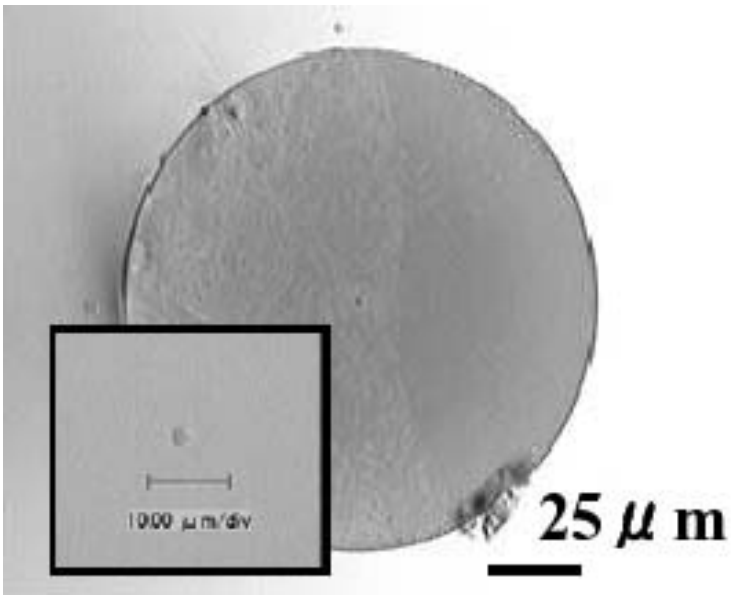

Figure 4.15 Cross-sectional image of highly nonlinear bismuth-oxide fiber [125].

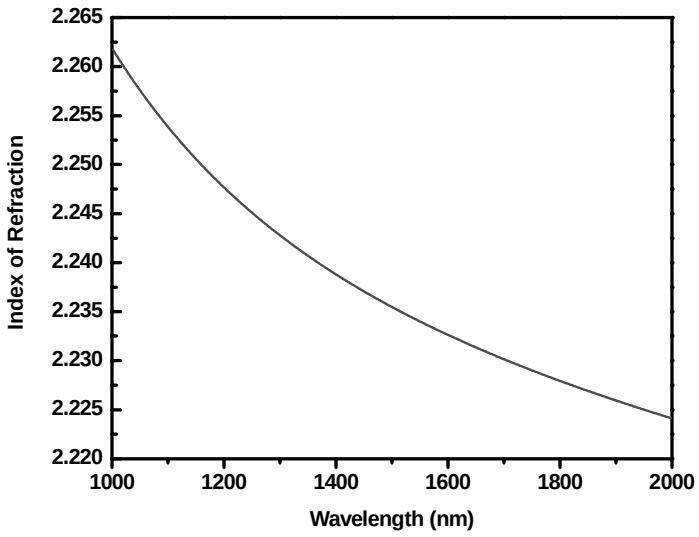

Figure 4.16 Index of refraction versus wavelength for nonlinear bismuth-oxide fiber [125].

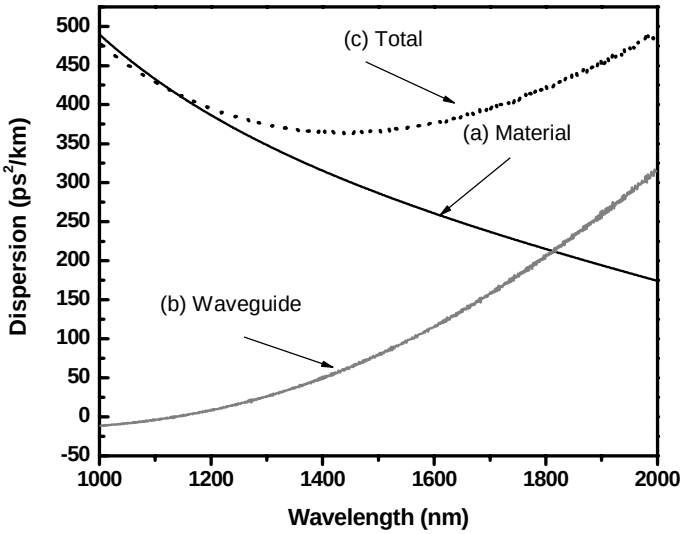

Figure 4.17 Dispersion as function of wavelength for: (a) bismuth-oxide glass (material) (b) waveguide (c) total dispersion of the fiber [125].

Simulations (under similar conditions to the experiments shown in Figure 4.20(d)) of supercontinuum generation are shown in Figure 4.18. The input excitation was at 1540 nm, with a 3-dB width of ~20 nm, and the fiber length was 2 cm. The input pulses were 150-fs duration sech-shaped and had a peak power of 2.6 kW. The split-step method was used to solve the nonlinear Schroedinger equation, including the effects of nonlinearity and second order dispersion [75]. In this case, the dispersion length was 0.0258 m, and the nonlinear length was 3.9×10^{-4} m. The resulting 3-dB spectral width was 200 nm, corresponding to a spectral broadening factor of 10. The spectral shape was smooth and flat, and was suitable for pulse compression.

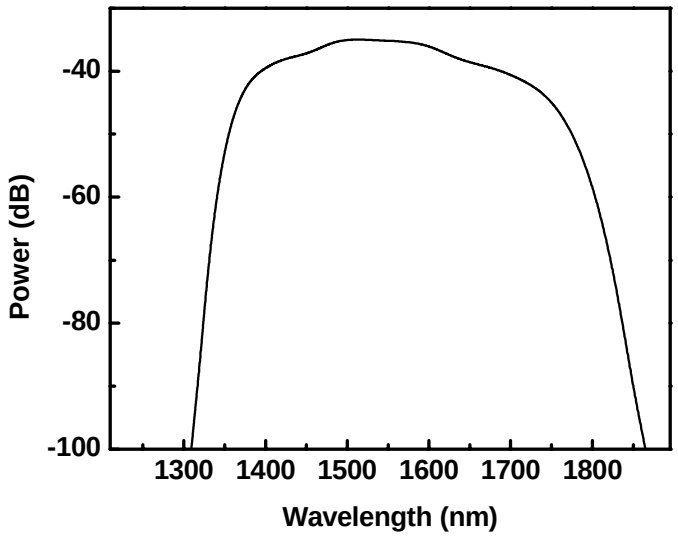

Figure 4.18 Simulation results for supercontinuum generation in 2 cm of bismuth-oxide fiber with 2.6 kW of peak power incident at 1540 nm [125].

The experimental setup for supercontinuum generation is shown in Figure 4.19. The OPO, producing 150-fs pulses tunable between 1400 to 1600 nm, was used as the signal source. The signal passed through an isolator, and was then spatially filtered with a 3 cm length of single mode fiber. This fiber was short enough that the pulses are not significantly distorted: the time-bandwidth product was within 20% of the transform limit. The pulses were coupled into a length of highly nonlinear bismuth-oxide fiber with an aspheric lens and the output collimated with an aspheric lens or reflecting objective. An optical spectrum analyzer, autocorrelator or grating compressor were used to characterize or further compress the output. The reflecting objective had ~30% loss, but eliminated chromatic dispersion. Two lengths of highly nonlinear bismuth-oxide fiber were investigated: 2-cm and 1-m. The ends of the 1-m length of fiber were prepared using a standard fiber cleaver at low tension (80 g). The 2-cm piece of fiber was embedded with wax in two connected ceramic ferrules and the ends were polished.

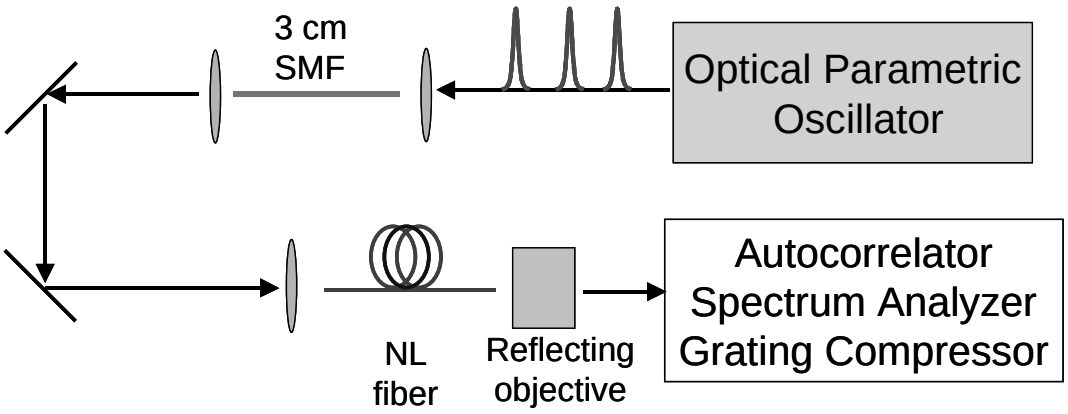

Figure 4.19 Experimental setup for supercontinuum generation in highly nonlinear bismuth-oxide fiber [125].

In Figure 4.20, spectra from a 2-cm length of fiber as a function of power are plotted. The coupling loss was 6 dB, and the OPO input was centered at 1540 nm. For an output average power of 32 mW, supercontinuum is produced from 1200 nm to > 1700 nm, and a 3 dB width of 170 nm. (The optical spectrum analyzer had a ranged limited to <1700 nm). For an average power of 32 mW exiting the fiber, the pulsewidth was 865 fs; for a power of 21.4 mW, the pulsewidth was 759 fs; for a power of 14 mW, the pulsewidth was 724 fs; and for a power of 7 mW, the pulsewidth was 488 fs. The interference seen in the center of the spectra was caused by insufficient attenuation of cladding modes. Optical wave breaking [75] is responsible for the shoulders apparent in the spectra. This effect occurs in the normal dispersion regime when the effects of self-phase modulation are much larger than that of group-velocity dispersion. The chirp resulting from group velocity dispersion is linear, while that resulting from self-phase modulation is not. Red-shifted light near the leading edge of the pulse overtakes unshifted light at the leading edge of the pulse. Blue shifted light at the trailing edge of the pulse travels more slowly than the unshifted light at the trailing edge. Interference results at the leading and trailing edges of the pulse because of the two different frequencies present. This gives rise to the shoulders seen in the optical spectra and oscillations near the pulse edges.

Next, the input wavelength of excitation was varied. Typical spectra, generated with 2-cm of fiber, are shown in Figure 4.21, for three different input wavelengths: 1450 nm, 1500 nm, and 1540 nm. The power was kept constant for the three measurements. The spectra are almost identical, indicative of the flat dispersion profile of the fiber. In order to obtain a more complete evaluation of the spectra for the case of the 1540 nm input, the measurements were extended to 1850 nm with a spectrometer.

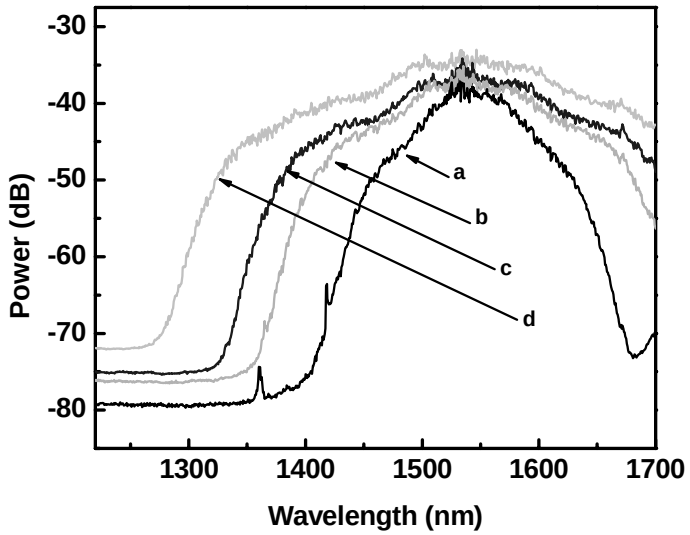

Figure 4.20 Spectra from a 2-cm piece of fiber generated by 1540-nm excitation at average powers exiting the fiber of: (a) 7 mW (b) 14 mW (c) 21.4 mW (d) 32 mW. The interference at the center of the spectra is due to insufficient attenuation of cladding modes.

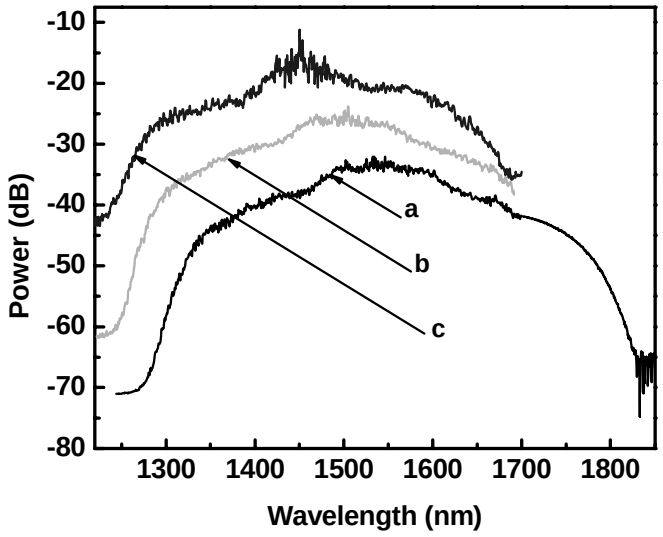

Figure 4.21 Spectra from a 2-cm length of fiber of input wavelengths of: (a) 1540 nm (b) 1500 nm (c) 1450 nm. The spectra were taken up to 1700 nm with an optical spectrum analyzer, and the measurement from 1700 - 1900 nm was taken with a spectrometer with the assistance of P. Rakich. The spectra were all taken for comparable powers and are vertically offset for ease of viewing.

Pulse compression experiments were performed for spectra generated with the 1540 nm input. The dispersion of the 2-cm piece of bismuth oxide fiber was compensated with a grating pair, with 75 lines/mm and separated by 8.5 cm [114]. The compressor, shown in Figure 4.22(a), had 5 dB of loss, with 6 mW of average power exiting the grating pair. The efficiency of the gratings as a function of wavelength is shown in Figure 4.23. The compressed pulses were measured with a broadband low-dispersion autocorrelator, shown in Figure 4.22(b). It consisted of two metallized beamsplitters, a speaker to dither the delay, a parabolic mirror to focus light onto a detector, and a GaAs LED used as a two-photon absorption detector. Figures 4.24 and 4.25 show a typical autocorrelation and spectrum. Pulses were compressed to 25 fs, and fitted with the PICASO phase retrieval algorithm [127]. The transform limit of the spectrum was 16 fs, and the time-bandwidth product of our compressed pulses, assuming a sech pulse envelope, was 0.49. Higher order chirp compensation probably limits the pulsewidth, as well as the roll-off in spectral efficiency of the gratings for wavelengths shorter than 1500 nm.

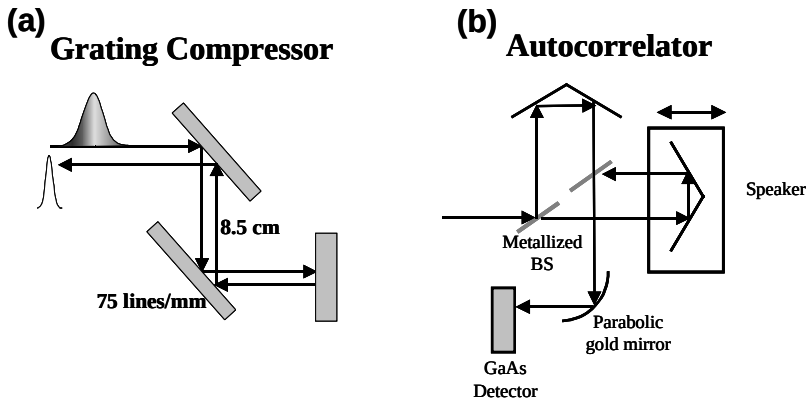

Figure 4.22 (a) Grating compressor used to compress pulses from 2 cm of highly nonlinear bismuth-oxide fiber. (b) Low dispersion broadband autocorrelator used to measure compressed pulses [125].

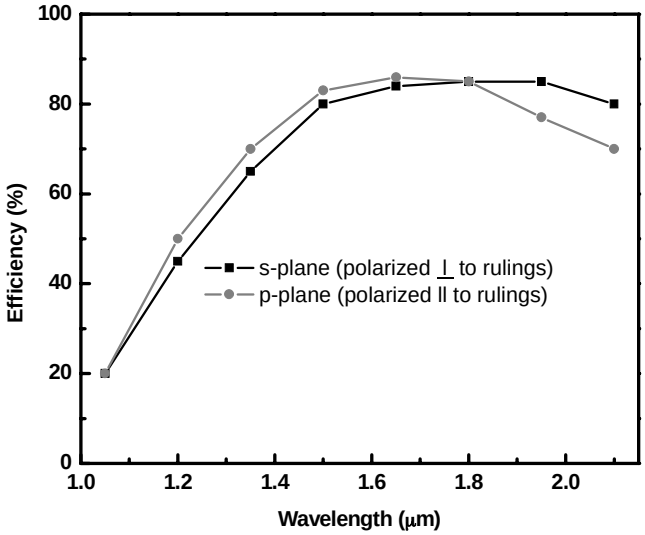

Figure 4.23 Efficiency of 75 line/mm gratings, as a function of wavelength.

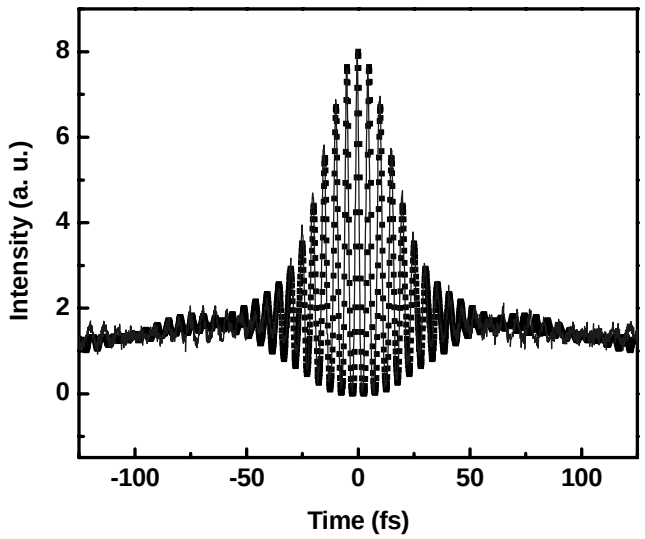

Figure 4.24 An interferometric autocorrelation of compressed pulses produced with 2 cm of fiber and a grating compressor. The PICASO phase retrieval algorithm was used to fit the data, and a pulsewidth of 25 fs is extracted. (Solid line: experimental result, black dots: retrieved autocorrelation.) [125]

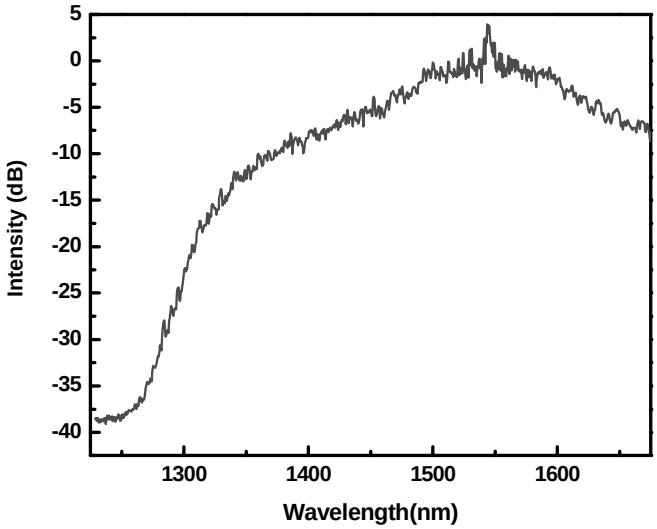

Figure 4.25 Spectrum corresponding to 25-fs compressed pulses.

A longer length of highly nonlinear bismuth-oxide fiber may be used if only broad spectra are required for an application. A spectrum produced from a 1-m length of highly nonlinear bismuth-oxide fiber is shown in Figure 4.26. The coupling loss is 4 dB, and the fiber has 2 dB of loss. The input excitation was 1540 nm and the maximum average output power 34 mW, and the corresponding pulse energy, 0.41 nJ. At this power, we estimate analytically an output pulsewidth is 80 ps. The pulse was too long to measure in our ultrafast autocorrelator. However, with the knowledge of the spectral 3-dB width and pulsewidth after 2 cm of fiber, we used the analytical formalism for the propagation of a chirped pulse through the additional 98 cm as follows [75].

(4.5)

$$\frac{T_1}{T_o} = \left[\left(1 + \frac{C\beta_2 z}{T_o^2} \right)^2 + \left(\frac{\beta_2 z}{T_o^2} \right)^2 \right]^{0.5}$$

where T_1 is the pulsewidth after propagation (1/e point for a Gaussian), T_0 is the initial pulse width (1/e point for a Gaussian), C is the chirp parameter, z is the propagation distance, and β_2, the second-order dispersion. The chirp parameter can be determined from the following relation

(4.6)

$$\Delta\omega = \frac{\left(1+C^2\right)^{0.5}}{T_o}$$

where Δω is the spectral half-width at T_o (at 1/e intensity point).

The spectrum generated, from 1200 to >1700 nm, is very similar to that produced in the 2-cm length, but the cladding modes are effectively suppressed with the longer 1-m length. After 2 cm, the pulse broadens to 800 fs and the effect of SPM is greatly decreased. Nevertheless, in the additional 98 cm, some additional spectral shaping is evidenced by the reduction of the shoulders due to optical wavebreaking.

The spectral broadening and pulse compression experiments described have all utilized fiber with cleaved or polished ends. However, it may be more convenient for some applications to use connectorized and spliced nonlinear fiber. The highly nonlinear fiber can be spliced to single mode fiber with a splicing loss of ~1.76 dB/spice.

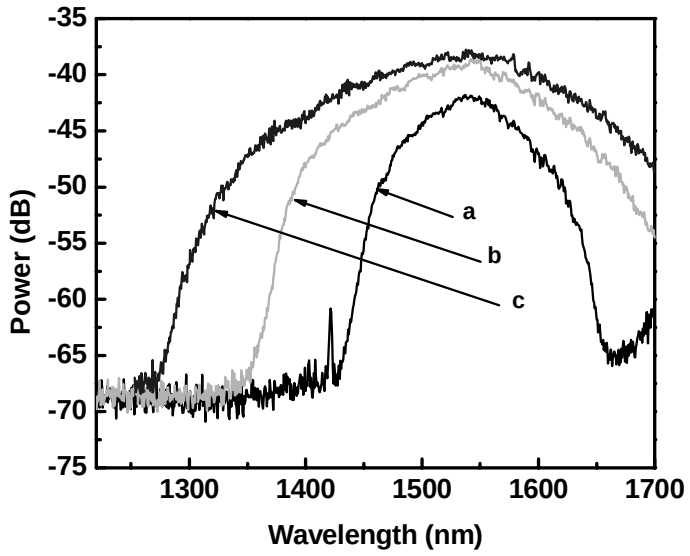

Figure 4.26 Spectra as a function of input power produced in a 1-m length of fiber at an input wavelength of 1540 nm. Average input powers and pulse energies were: (a) 10 mW/0.12 nJ (b) 20 mW/0.24 nJ (c) 34 mW/0.41 nJ [125].

In conclusion, highly nonlinear bismuth-oxide fiber has been used to generate smooth unstructured spectra at telecommunications wavelengths in very short lengths. Pulses have been compressed from 150 fs to 25 fs, using a 2-cm length of this fiber. Broad, Gaussian-like spectra, suitable for applications in medical imaging have been produced with a 1-m length of this fiber. A spliced length of this fiber was shown to produce continuum also. Highly nonlinear solid-core bismuth oxide fiber is a promising tool for applications requiring broad spectra and/or short pulses at telecommunications wavelengths. Potential applications include frequency metrology, spectroscopy, communications, characterization of broadband devices, and medical imaging techniques such as optical coherence tomography.

4.6 Conclusion

Bismuth-oxide fiber is a newly developed fiber with applications in broadband amplification and spectral broadening at telecom wavelengths. Bismuth-oxide amplifiers can provide continuous C- and L-band amplification unlike conventional silica-based EDFA's. Amplification in the L-band is more efficient than that of conventional silica-based EDFA's. The material composition of the bismuth-oxide-based glass host allows for higher doping with erbium. Thus gains of 20 dB are achievable in a 23-cm length of bismuth-oxide fiber, doped with 6470 ppm of erbium, between 1535 - 1555 nm. Gains of greater than 12 dB are measured between 1520 to 1600 nm. A 55.6 cm length of bismuth-oxide erbium-doped fiber was used as the gain medium in an L-band modelocked laser, producing 288-fs pulses at 1600 nm. Undoped, highly nonlinear, bismuth-oxide fiber can be used for smooth supercontinuum generation and pulse compression at telecom wavelengths. Supercontinuum with a full-width-half-maximum of 170 nm was generated in a 2-cm length of fiber, and 150-fs pulses were compressed to 25 fs.

CHAPTER 5: THIRD-ORDER NONLINEARITIES IN GE-AS-SE-BASED GLASSES

5.1 Abstract

The third-order optical nonlinearities of Ge-As-Se-based glasses were studied. The glasses have high melting and glass transition temperatures and can be integrated with traditional compound oxide glasses into highly nonlinear, high-index-contrast fibers. Two key parameters of the glasses: the nonlinear refractive index and two-photon absorption coefficient, were measured with z-scan and femtosecond pump-probe techniques at telecommunication wavelengths. Nonlinearities as high as ~900 times that of silica were measured at 1540 nm, in $Ge_{35}As_{15}Se_{50}$, with a glass transition temperature of 380°C. Section 5.2 gives background on chalcogenide glasses and Section 5.3 discusses the experiments. The chalcogenide glasses were fabricated at Omniguide Corporation with collaborators W. King, M. Shurgalin, and V. Flufygin and M. Soljačić (MIT/Omniguide).

5.2 Background

In the previous chapters, highly nonlinear fibers such as bismuth-oxide-based fiber and microstructure fiber were discussed. These fibers owe their high nonlinearity mainly to their small effective areas, made possible by high-index-contrast. An alternative approach involves fiber and devices fabricated from materials with intrinsically high nonlinear refrac-

tive index coefficients, such as chalcogenide glasses. While optical telecommunications systems with bit rates as high as 40 Gb/s have been commercialized, the systems are by no means 'all-optical'. Some key functions, such as switching, are still performed electronically. In the future, it is maybe expected that optical devices will supersede their electronic counterparts. Nonlinear materials will play a key role in these developments.

In materials, the optical Kerr effect causes a change in index of refraction that is proportional to the optical intensity, I, and the nonlinear index coefficient, n_2 (see Equation 3.10). The strength of n_2 is directly proportional to the third-order nonlinear susceptibility. While the Kerr effect is weak because it is a nonresonant effect, this also produces an ultrafast time response. Thus, the optical Kerr effect can be utilized for modelocking and nonlinear fiber or devices. In addition, an all-optical ultrafast switch with low switching energy can be designed based on the Kerr effect. To design such an all-optical switch, a Kerr material can be placed in one arm of a Mach-Zender interferometer, causing an intensity-dependent phase shift. Ultimately, such a switch will be limited by TPA, which occurs when the photon energy is above half-gap in the material. If a switch is fabricated from a glass-based material, absorption tails will lead to some TPA below half-gap. This limits the maximum phase shift achievable. For such a switch, a figure of merit, $n_2/\beta\lambda$ [128], where n_2 is the nonlinear refractive index, and β, the two-photon absorption coefficient, can be defined to assess the material properties relevant for efficient optical switching. To achieve a nonlinear optical phase shift of π, necessary for a Mach-Zender optical switch, with a nonlinear transmission loss of 20%, a figure of merit of ~2 is required [129]. This figure of merit may not be the only applicable measure of the feasibility of such a switch. Depending on the regime of operation, it is possible that linear losses could provide the ultimate limit on performance.

In communications systems, the nonlinearity of optical fiber, due, in part to the nonlinear refractive index coefficient of silica glass, is often undesirable. However, the nonlinearity of standard silica used for telecom fiber, $n_2 = 2.6 \times 10^{-20}$ m^2/W, is too low to allow fabrication of compact devices based on nonlinearities. Nonlinearities several orders of magnitude greater than silica at 1550 nm can be achieved in other materials such as semiconductors and chalcogenide glasses [129]. Chalcogenide glasses, glasses fabricated with elements from groups II, IV and VI of the periodic table, have been the subject of much research, with high nonlinearities at 1550 nm and transmission into the far infrared region [130][131][132]. Many different compositions fall under the chalcogenide family of glasses including As-Se, Ge-Se, As-S-Se, Ge-Se-Te, Ge-Se-Sb, and Ge-As-S-Se. There have been a number of studies of the nonlinearity of chalcogenide glasses [129][130][131][132] as well as the fabrication of fiber [133][134][135] and waveguides [136][137][138]. In particular, the Ge-As-Se chalco-

genide system is of interest due to high nonlinearity, high refractive index (2.4-2.65), suitable optical transmission at 1.55 μm and relatively broad glass formation region. This glass family also shows promise for fabrication into high-index-contrast highly nonlinear fiber for 1.55 μm applications.

Chalcogenide glasses have much lower softening and melting temperatures (100-400^{o}C) than standard glasses such as fused silica (900-1100^{o}C). Standard fabrication techniques cannot be used to make chalcogenide devices. The low melting temperatures also make it difficult to co-process chalcogenides with other glasses with lower indices and nonlinearities. However, glasses in the Ge-As-Se family have glass transition temperatures in the range of 150-390^{o}C making them suitable for integration with low refractive index compound-oxide glasses into high-index-contrast solid-core fiber. Low-index-contrast highly nonlinear chalcogenide fiber can be fabricated with a chalcogenide core and cladding [133][134]. However, high-index-contrast fiber offers the advantages of smaller modal volume, higher nonlinearity and greater range of achievable dispersion. While considerably more complex than low-index-contrast chalcogenide fibers, high-index-contrast solid core fibers offer perhaps a simpler alternative to 'holey' structures, in which air is used as the low-index-contrast material. Examples of these include photonic bandgap fiber [135] and microstructure chalcogenide fiber. However, the fabrication of solid-core high-index-contrast fiber does pose some challenges. The chalcogenide glasses used in the fiber core must have a glass transition and softening temperature compatible with that of lower index glasses used for the cladding.

5.3 Z-scan and pump-probe measurements of Ge-As-Se glasses

The glasses investigated in this research were specifically selected for their high nonlinearity and high glass transition temperatures ranging from 292^{o}C to 380^{o}C. The glasses investigated were: $Ge_{33}As_{12}Se_{55}$ (commercially available as AMTIR-1, from Amorphous Materials), $Ge_{35}As_{15}Se_{50}$, $Ge_{25}As_{10}Se_{65}$, and $Ge_{22}As_{20}Se_{58}$ (commercially available as GASIR1, from Umicore). The glasses are found to have nonlinearities between 200x - 900x that of silica, and figures of merit, $n_2/\beta\lambda$, as high as 3.2 [139]. Table 5.1 lists some of the common properties of $Ge_{33}As_{12}Se_{55}$ (AMTIR-1) [140].

Table 5.1 Properties of $Ge_{33}As_{12}Se_{55}$.

Characteristic	Value
Density	4.4 g/cm^3
Thermal Expansion	$12x10^{-6}/^oC$
Hardness (Knoop)	170
Rupture Modulus	2700 psi
Young's Modulus	$3.2x10^6$ psi
Shear Modulus	$1.3x10^6$ psi
Poisson's Ratio	0.27
Thermal Conductivity	$6x10^{-4}$ cal/(cm-s-K)
Specific Heat	0.07 cal/(g-K)
Resistivity	$2x10^{12}$ cm @ 100 Hz
Glass Transition Temperature	362 ^oC
Index of Refraction (1.5 μm)	2.5469

The samples of $Ge_{33}As_{12}Se_{55}$, $Ge_{35}As_{15}Se_{50}$, and $Ge_{25}As_{10}Se_{65}$, were prepared at Omniguide Corporation as follows. For each glass composition, 5N (99.999%) purity amorphous selenium shot, 7.5N (99.999995%) purity crystalline lump arsenic, and 6N (99.9999%) purity single crystal germanium were batched into a fused quartz looped tube along with a magnesium metal strip (4N purity). A schematic of the quartz tube is shown in Figure 5.1. The tube was placed into a two-level furnace, with the looped portion of the tube, containing the As, Se and magnesium metal strip, in the hotter furnace zone. Over ~12 hours, the As and Se components melted and were distilled from the loop into the lower part of the tube containing the Ge. During this process, the Mg strip getters any oxygen contaminants along with any other non-volatile contaminants. After distillation, the lower portion of the tube was sealed, creating the melt vessel, and the loop containing impurities was discarded [141]. The melt vessel was placed into a rocking furnace at 900°C for 12 hours, homogenizing the glass melt. The melt was then placed into a second furnace at the expected glass transition temperature. This furnace was switched off, allowing the glass to cool slowly to room temperature. The

glass boules were cut into flat disks of about 3 mm thickness and the facets were ground parallel and polished to optical quality. Samples of $Ge_{33}As_{12}Se_{55}$ prepared in this manner were found to have similar n_2, β, and bandgap energy to commercial samples purchased from Amorphous Materials. The sample of $Ge_{22}As_{20}Se_{58}$, a 3 mm thick sample with polished parallel faces, was purchased from Umicore.

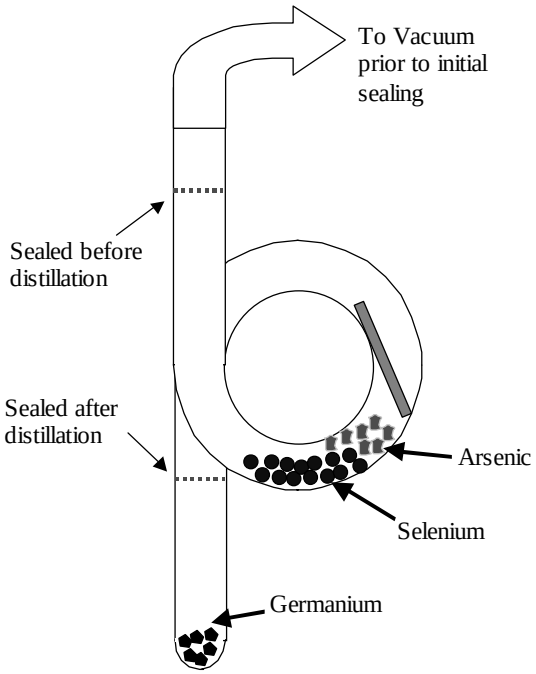

Figure 5.1 Looped quartz tube used to fabricate chalcogenide glasses from raw ingredients. Courtesy of W. King.

Linear transmission measurements were performed to characterize the optical bandgap of the samples. A spectrophotometer was used, in which a white light source was passed through the samples at normal incidence. Behind the samples a spectrometer scanned, and collected, transmission information versus wavelength. The signal was compared to the transmission through an identical blank reference compartment. By taking the ratio of the signal to the reference, one can determine the absolute transmission of the glasses versus wavelength. Because the chalcogenide glasses studied were amorphous, they did not have a sharp absorption edge. Thus, the point at which the absorption changed from a quadratic dependence on energy to an exponential dependence on energy (Urbach tail region [142]) was defined as the bandedge. In this region, the absorption obeys the relation:

(5.1)

$$\alpha(\omega) = \alpha(E_g)e^{-(E_g-\hbar\omega)/E_u}$$

where α(ω) is the absorption coefficient as a function of frequency, E_g, the energy gap, $h\omega/2\pi$, the energy of the incident photons, and E_u, a measure of the steepness of the absorption edge [143]. A typical value of the absorption coefficient, $\alpha(E_g)$, at this point is 1000 cm^{-1} [129] and was used here for the definition of the optical bandgap. Fits of the data to an exponential in the Urbach tail region yield the bandgap. The absorption coefficient is related to the linear transmission of a sample as follows:

(5.2)

$$\alpha = \ln(T) / L$$

where T is the transmission and L, the sample length. A typical measurement is shown in Figure 5.2.

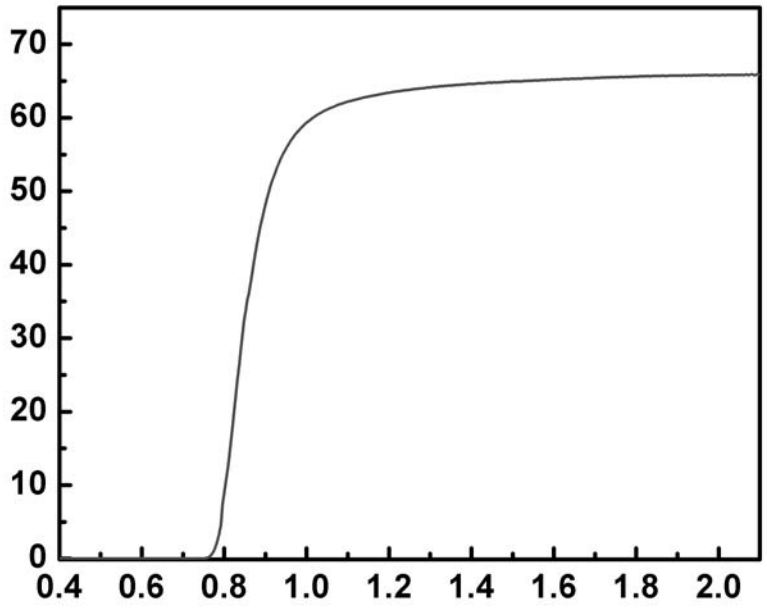

Figure 5.2 Typical linear transmission measurement of $Ge_{35}As_{15}Se_{50.}$ From this measurement, the bandedge was determined to be 639 nm.

Z-scan and pump-probe measurements were used to characterize the nonlinear refractive index (n_2) and two-photon absorption (β) coefficients of these glasses. The z-scan tech-

nique is a simple technique allowing the measurement of the change in phase caused by n_2 and the change in absorption caused by TPA. In the z-scan technique [144], a collimated Gaussian beam is focused onto a sample. The sample is translated through the beam focus and the transmission through an aperture behind the sample is measured. The nonlinear refractive index, n_2, causes a transverse variation of the index across the sample. Thus, the sample acts as a lens with an intensity-dependent focal length. When the sample is placed at the focus of the Gaussian beam, there is no change in transmission through the aperture. When the sample is moved further away from the focusing lens, in the case of a positive nonlinearity, it collimates the beam, increasing the transmission through the aperture. When the sample is moved closer to the focusing lens, it causes the beam to diverge (in the case of positive nonlinearity), and the transmission through the aperture decreases. Simply removing the aperture allows only the absorption caused by two-photon absorption to be measured. A schematic of the z-scan method is shown in Figure 5.3.

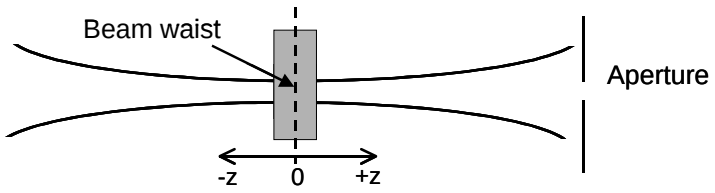

Figure 5.3 Schematic of the z-scan method.

Analytical expressions have been developed, allowing one to extract the value of n_2 and β from the z-scan traces. The data in these studies was fitted using the simplified expressions for open and closed aperture scans below [144][145].

(5.3)

$$T_{op(z)} = 1 - \frac{\beta I_o L}{2\sqrt{2}\left(1 + x^2\right)}$$

(5.4)

$$T_{cl(z)} \cong 1 + \frac{4x(\Delta\phi_o)(1-S)^{0.25}}{\left(1 + x^2\right)\left(9 + x^2\right)}$$

where β is the two-photon absorption coefficient; I_o, the peak on-axis intensity; L, the sample length; $x = z/z_o$, where z is distance and z_o, the confocal parameter defined as

(5.5)

$$z_o = \frac{\pi w_o^2}{\lambda}$$

with ω_o defined as the beam waist; S, the aperture transmission; and $\Delta\phi_o$ the time-averaged peak-on-axis phase change defined as

(5.6)

$$\Delta\phi_o = \frac{2\pi L n_2 I_o}{\lambda\sqrt{2}}$$

The expression for the open aperture scan assumes a Gaussian pulse shape. These expressions are valid for small phase shifts $\Delta\phi << 1$. Otherwise, one must use the exact formulas in [144].

Figure 5.4 shows the experimental setup. The z-scan formalism assumes a Gaussian beam. To ensure this, the OPO output beam was coupled through 3 cm of standard single mode silica fiber terminated with a collimator (Corning SMF-28) for spatial filtering. The 3 cm of SMF does not chirp the pulse significantly. Even at average powers as high as 150 mW, both the spectrum and pulsewidth are within 20% of the transform limit for a Gaussian pulse. However, with such short pulses at such high power, 3 cm is likely to be close to the maximum length of fiber that can be tolerated without distortion. After propagation through the SMF, the beam is recollimated and focused onto the sample, with a 50 mm lens. The optical length of the sample should be smaller than that of the beam's confocal parameter for the analysis above to be valid. Thus, with 3 mm sample thickness, we are limited in spot size by the above constraint. To measure n_2, a 200 μm aperture is placed after the sample (closed-aperture scan), and a lens images the apertured spot onto a large area Ge photodiode, connected to a lockin amplifier and a computer. By simply removing the aperture, the two-photon absorption coefficient can be measured (open-aperture scan). To account for inhomogeneities in the samples, traces at attenuated intensities were also taken and subtracted from the high intensity scans. The z-scan setup was calibrated with samples of Si, GaAs, and As_2Se_3, whose n_2 and β are known from the literature [146][147].

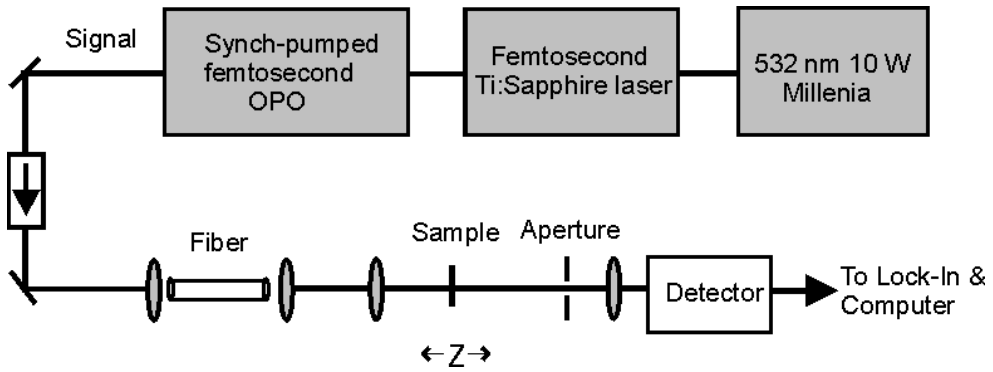

Figure 5.4 Experimental setup for z-scan measurements.

Z-scan is usually performed with lasers at low repetition rates (kHz), so that thermal lensing, which produces similar effects to that of self-focusing, is not a concern. With the 82 MHz laser used in this experiment, thermal lensing effects can occur. To prevent this, one must lower the average power. Pulse picking with an acousto-optic modulator is one alterative; another is performing the z-scan experiment with pulses of two different widths. Thermal effects are only sensitive to average power, not peak power. With long pulses, the signal will be dominated by thermal lensing effects. However, with short pulses, effects from both thermal lensing and nonlinearity will be observed. By comparing the two results, one can determine if there are any significant thermal lensing effects in the sample. In our study, z-scan measurements were performed with 150-fs pulses and 1.5 ps pulses. The 1.5 ps pulses were produced by replacing the 3 cm of SMF with 50 cm of dispersion compensating fiber (DCF), with a dispersion of -74 ps/nm/km. To ensure that the spot size incident on the sample was the same for both 1.5-ps and 150-fs pulses, identical collimators were spliced on to the ends of both fibers.

Because the Ge-As-Se samples had small TPA coefficients, it was difficult to accurately determine their values with z-scan. A pump-probe technique, which has higher sensitivity than that of z-scan, was used to verify some of these values. In the z-scan technique, a single beam is focused through a sample and onto a detector. As the sample is translated, small changes in the DC signal on the detector are observed. The sensitivity of z-scan is limited by linear scatter from the sample surface and the signal-to-noise ratio of the detector is degraded by the large unchanging DC background. In pump-probe, two beams are focused onto a sample and only probe photons that have interacted with modulated pump photons are detected. Thus, in pump-probe, one detects a small signal, indicative only of the change in the sample, enhancing the sensitivity. However, determination of the fluence incident on the sam-

ple in pump-probe can be more difficult than that of z-scan, since one needs to account for the overlap of the pump and probe beams on the sample. If the overlap of pump and probe is not perfect, it will lower the effective fluence on the sample. The pump-probe measurements on the chalcogenide samples were performed with a setup similar to that described in Chapter 2. A schematic of the setup used for these measurements is shown in Figure 5.5. The induced changes in absorption observed are dominated by two-photon absorption because the laser wavelength, 1540 nm, is well below the bandgap. With knowledge of the incident intensity, the two-photon absorption coefficient can be determined from the data. The fluence in the pump-probe setup was calibrated with a sample of known TPA. Measurements were taken at several different fluences to ensure that no other nonlinear effects appeared at the highest fluences. To determine the TPA coefficients of the chalcogenide glasses, a combination of pump-probe and z-scan measurements were used.

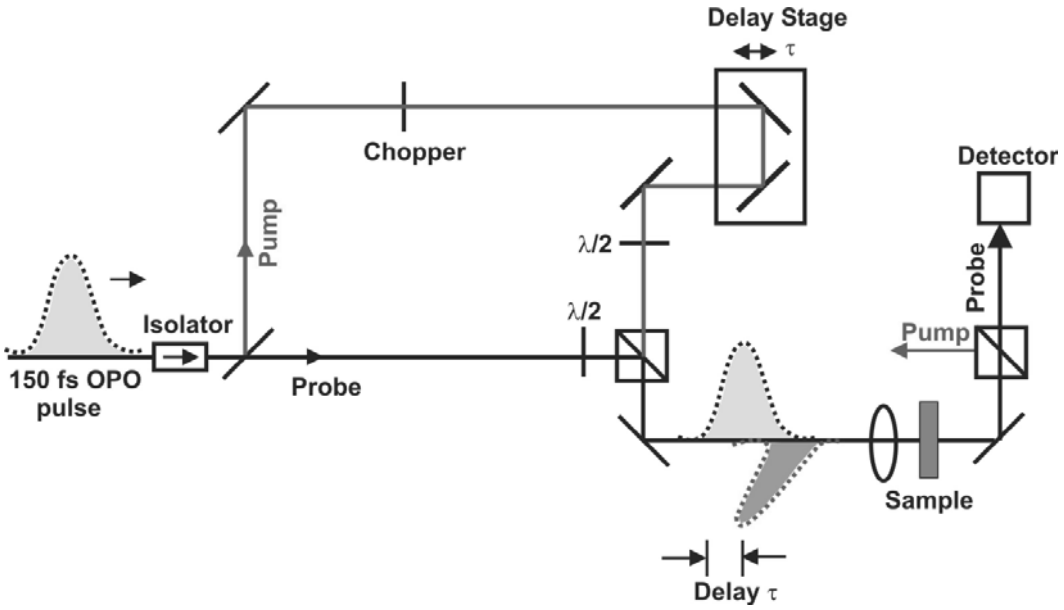

Figure 5.5 Schematic of pump-probe setup used to determine the TPA coefficients of the chalcogenide glasses.

Typical z-scan closed- and open-aperture traces are shown in Figures 5.6 and 5.7. At 1540 nm, the nonlinear refractive index (n_2) of $Ge_{33}As_{12}Se_{55}$ was measured to be $15x10^{-18}$ m^2/W +/- 25% and the two-photon absorption coefficient (β), 0.4 cm/GW +/- 25%. Values of n_2 in the other materials investigated ranged from 6.0 to $24x10^{-18}$ m^2/W, and that of β, from 0.4 to 0.5 cm/GW. Fresnel losses on the front sample surface were included (~18% loss), when determining incident intensity. No evidence of thermal effects for any of the glasses can be seen in the data. Data was taken with intensities as high as 170 MW/cm^2, and no damage

to the samples was observed. A typical pump-probe trace on $Ge_{35}As_{15}Se_{50}$ is shown in Figure 5.8.

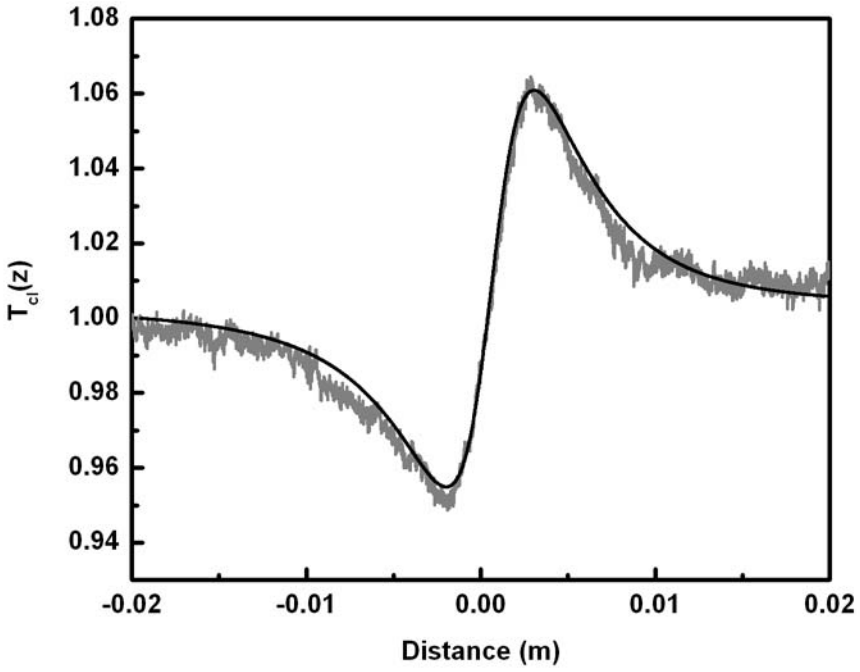

Figure 5.6 Closed-aperture scan of $Ge_{33}As_{12}Se_{55}$ [139].

Important characteristics of the chalcogenide glasses investigated such as nonlinearity, two-photon absorption coefficient, bandedge, glass transition temperature and figure of merit, are summarized in Table 5.2. At 1540 nm, the value of n_2 measured ranges from 200 to 900 times that of fused silica, 2.6 x 10^{-20} m^2/W. While As_2Se_3, a previously characterized chalcogenide glass, also has a nonlinearity 900 times that of silica, its glass transition temperature is quite low, 188°C. Upon first examination of Table 5.2, trends may not be apparent. With increasing Ge content, the bandgap energy of the glasses decreased and the nonlinearity and glass transition temperature increased. The two-photon absorption coefficient increased also, but slowly. Thus, with increasing Ge content, the figure of merit increases, making the glasses more suitable for fiber-based applications. Unfortunately, the Ge-As-Se glasses become more prone to crystallization with high Ge content [148]. The nonlinear figure of merit, $n_2/\beta\lambda$, was approximately 3.2 for $Ge_{35}As_{15}Se_{50}$, the highest value reported for glasses that can be codrawn into fiber with low index glasses (i.e. glasses with relatively high melting temperatures).

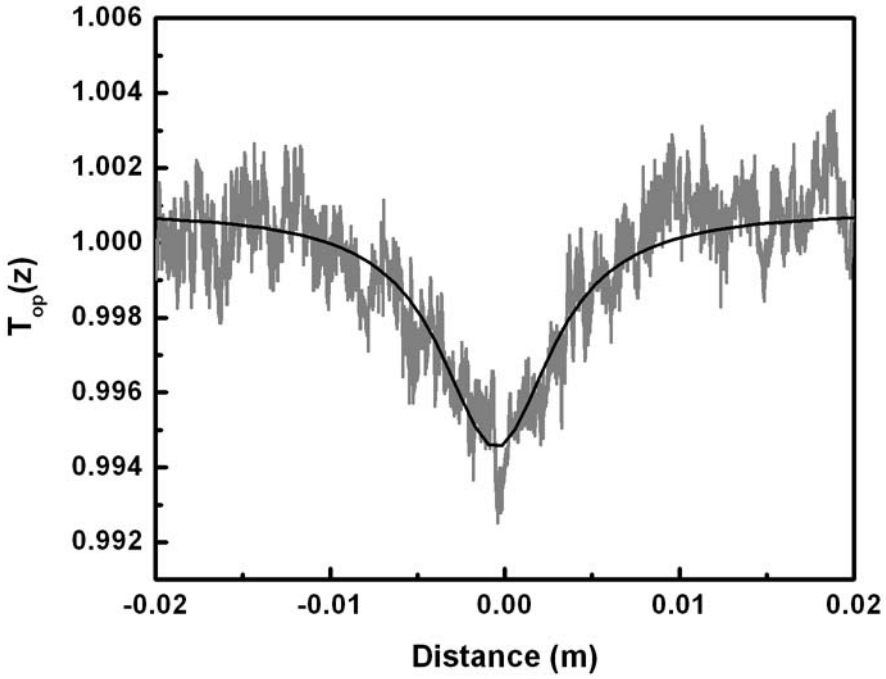

Figure 5.7 Open-aperture scan of $Ge_{33}As_{12}Se_{55}$ [139].

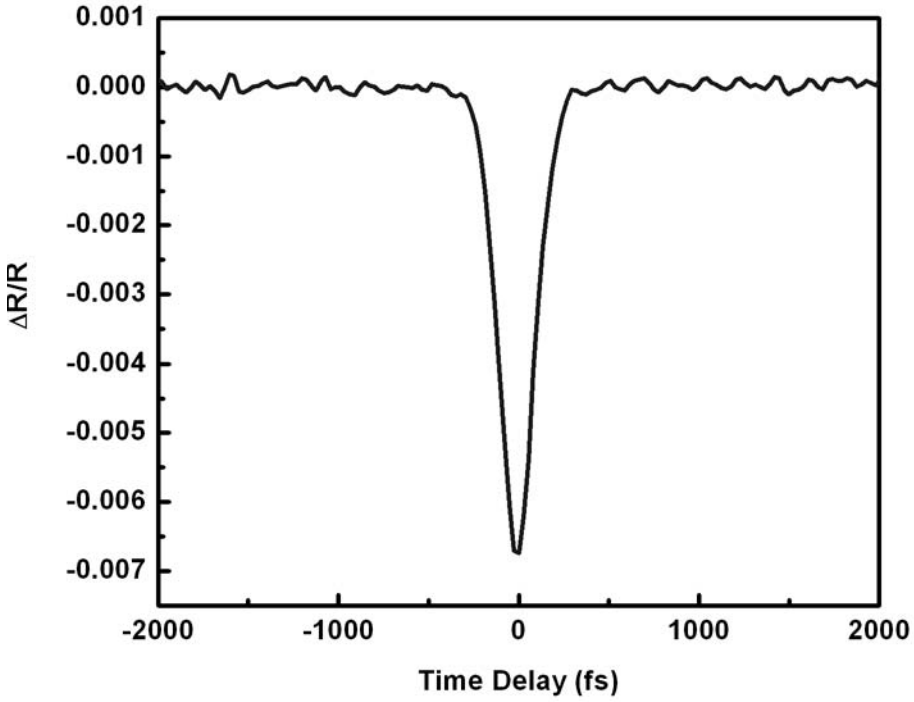

Figure 5.8 Typical pump-probe trace on $Ge_{35}As_{15}Se_{50}$.

Table 5.2 Properties of Ge-As-Se glasses.

Material	Bandedge (nm) +/- 4%	n_2 x 10^{-18} m_2/W +/- 25%	β (cm/GW) +/- 25%	Glass Transition Temp (^oC)	Softening Transition Temp (^oC)	Figure of Merit $n_2/\beta\lambda$
$Ge_{35}As_{15}Se_{50}$	639	24.6	0.5	380	474	3.2
$Ge_{33}As_{12}Se_{55}$	600	15	0.4	362	476	2.4
$Ge_{22}As_{20}Se_{58}$	614	9.2	0.4	292	unknown	1.5
$Ge_{25}As_{10}Se_{65}$	585	6.0	0.4	305	436	1.0

The glasses listed in Table 5.2 have only small compositional variation, but these differences have a large effect on the value of n_2. In contrast to the fourfold variation with composition of the nonlinear refractive index coefficient, the two-photon absorption coefficient does not vary much at all. Resonant effects cause both the two-photon absorption and nonlinear index coefficient to increase as the wavelength of operation approaches half-bandgap. Because the glasses exhibit an Urbach absorption tail below the bandgap, n_2 increases faster than β below half-gap, leading to a maximum in the figure of merit slightly below the half-bandgap [130].

As the composition of binary chalcogenide glasses such as GeSe is varied, the effects on the nonlinearity of the material is relatively well-understood [131][132]. The ‘lone electron pair’ approach is used to explain these correlations. According to this theory, the nonlinearity of the chalcogenide glasses increases with the concentration of the highly polarizable lone electron pairs [131][132]. However, this model does not satisfactorily explain the variations of the non-linear response we have observed. For example, in this study, the glass with the lowest number of lone electron pairs, $Ge_{35}As_{15}Se_{50}$, had the highest value of n_2. We have also observed an unexpected rise of nonlinear refractive index for compositions in which part of selenium is substituted with arsenic: compositions $Ge_{22}As_{20}Se_{58}$ and $Ge_{33}As_{12}Se_{55}$ versus composition $Ge_{25}As_{10}Se_{65}$ (Table 5.2). The trends we observe are similar to that made by *Quémard et. al.* [132] for the same family of chalcogenide glasses. Apparently, the contribution to polarizability from the lone electron pairs is not the predominant factor influencing the nonlinear properties of ternary Ge-As-Se glasses. Additional factors, such as glass structure

or density, the presence of unpaired electrons[148], and the presence of defect states must be taken into account. While the structure of the amorphous chalcogenide glasses can be viewed as an assembly of different structural units, such as $GeSe_4$ and $AsSe_3$, the situation is further complicated by the opportunity for both homopolar (e.g., Ge-Ge) and heteropolar bonds (ex. Ge-Se). This leads to a variety of 'defect' gap states, which can contribute to the nonlinearity. For the glasses reported herein, the smallest nonlinearity is seen for $Ge_{25}As_{10}Se_{65}$, which is expected to be closest to the stoichiometric ideal, highlighting the importance of 'defect' gap states.

5.4 Conclusion

In summary, we have investigated several Ge-As-Se chalcogenide glasses with high melting temperatures suitable for high-index contrast, high nonlinearity fiber. $Ge_{35}As_{15}Se_{50}$ has a nonlinearity of 24 x 10^{-18} m^2/W, and a figure of merit of 3.2. Such materials show great potential for telecom applications that might use highly nonlinear, high-index-contrast fiber.

CHAPTER 6: CONCLUSIONS AND FUTURE WORK

6.1 Conclusions

In this thesis, four major topics of research were presented: semiconductor saturable Bragg reflectors for a variety of ultrafast solid-state and fiber lasers, microstructure fiber for four-wave mixing, bismuth-oxide fiber for amplification and supercontinuum generation, and Ge-As-Se glasses with high nonlinearities for highly nonlinear fiber or integrated optical switches. The third-order nonlinearities in these devices and materials have been characterized to assess their suitable for applications in or with ultrafast lasers. The author hopes that this work will be useful for other researchers in the field of ultrafast optics.

Advances towards ultrabroadband saturable Bragg reflector design, fabrication, and implementation in femtosecond solid-state lasers have been presented both in III/V and Si-based materials. The III/V structures were fabricated using a modification of a process commonly used for VCSELs, the oxidation of AlAs; and the Si-based structures were fabricated with standard Si-CMOS compatible techniques. In contrast to other previously reported solutions, these structures were robust and stable, and the fabrication less complex. Self-starting femtosecond pulse operation has been achieved with broadband SBRs in Cr^{4+}:YAG, Cr:Forsterite, Ti:Sapphire, Er:glass and bismuth-oxide erbium-doped fiber lasers. These advances should allow the development of turnkey ultrafast laser systems with uses in frequency metrology, ultrafast spectroscopy, medical imaging, and other applications of nonlinear optics.

Ultrafast lasers are useful for their short pulses, broad spectra, and high peak powers, enabling nonlinear experiments. However, highly nonlinear fiber can be used to easily generate broad spectra. Microstructure fiber was used, not for continuum generation, but instead to generate new frequency components through four-wave mixing. In a tapered microstructure fiber, highly nondegenerate four-wave mixing with a frequency shift of 6000 cm^{-1} in a length of 1.4 cm was achieved. These experiments were really a proof of concept, showcasing the fact that with increasing nonlinearity and unique dispersion profiles, microstructure fibers are an important newly developed medium for nonlinear optics.

Broadband amplification and controlled supercontinuum generation have been demonstrated with bismuth-oxide fiber. Bismuth-oxide fiber amplifiers may be a candidate for continuous C- and L-band amplification and laser sources in WDM communication systems. Amplifier efficiency in the L-band is significantly higher than that of conventional erbium-doped amplifiers. High doping concentrations of erbium allow for short lengths of fiber to be used, enabling the construction of compact fiber amplifiers and lasers. Amplification with a 22.7 cm piece of fiber has been demonstrated between 1520-1600 nm. Undoped, highly nonlinear bismuth-oxide fiber can be used for controlled supercontinuum generation. Fibers with some of the highest nonlinearities reported, 1100 $(W\text{-}km)^{-1}$ have been fabricated. While the nonlinear index coefficient of bismuth-oxide glass is two orders of magnitude larger than fused silica, chalcogenide glasses have even higher nonlinear index coefficients. However, bismuth-oxide glass is a nice stepping stone between fused silica and chalcogenides. Fused silica's nonlinearities are too low to allow the fabrication of compact devices, while chalcogenide glasses are extremely difficult to process due to their softness, brittleness, and low melting temperatures. A short length of nonlinear bismuth-oxide fiber, 2 cm, has been used to generate spectral broadening of a 20 nm FWHM spectra to a 200 nm FWHM, and subsequently to compress 150-fs pulses to 25 fs. Applications are similar to those of SBRs: frequency metrology, medical imaging, and ultrafast spectroscopy.

This brings us to the final topic of this thesis: chalcogenides. Chalcogenide glasses have been the subject of extensive research for many years. They were first known for their transmission in the infrared, but more recently, have been the subject of research for fibers and devices that utilize their high nonlinearity. While there are still significant fabrication hurdles to be overcome, progress is being made [138]. The addition of Ge to As-Se-based chalcogenide glasses increases the glass transition temperature without degrading the nonlinearity. For $Ge_{35}As_{15}Se_{50}$, nonlinearities 900 times that of silica have been measured, with a figure of merit of 3.2. These glasses show promise for highly nonlinear fiber and integrated all-optical switching.

In summary, a variety of devices and materials for use in or with ultrafast lasers have been studied. Saturable Bragg reflectors have been demonstrated in a variety of self-starting laser systems producing femtosecond pulses. Microstructure fiber has been used to demonstrate highly non-degenerate four-wave mixing. Broadband amplification and an L-band laser have been demonstrated with erbium-doped bismuth-oxide fiber. Highly nonlinear bismuth-oxide fiber has been used for pulse compression and supercontinuum generation. Finally, chalcogenides glasses with nonlinearities almost three orders of magnitude larger than fused silica have been studied.

6.2 Future work

Research never stops, and so there is always more to be done. This seems to be in part the reason for the average time of an MIT Ph.D. thesis: 6 years. With the four topics discussed, I will outline improvements and future experiments that can be performed. The work to be performed is collaborative - not all of the suggested improvements can be implemented solely by the Ippen research group.

To more fully understand the dynamics of the semiconductor saturable Bragg reflectors, further ultrafast pump-probe spectroscopy could be performed. With ultrafast pulses, the time constant of the carrier-carrier scattering that is responsible for the fast time constant in SBRs could be resolved. This ultrafast time constant plays a major role in pulse shaping especially inside purely saturable-absorber modelocked lasers. The dynamics in the Si/Ge absorber, in particular, appear to be very fast. More information about the dynamics of this device could be extracted with ultrafast pump-probe measurements. A device should be fabricated with a thicker Ge layer. This will probably improve laser performance and will enable a more careful characterization study of the device with pump probe.

Additionally, heterodyne pump-probe could be performed on all the structures described. The pump-probe setup in this thesis could only measure changes in the absorption, not changes in index. Heterodyne pump-probe will allow us measure index changes and determine what role they play in laser modelocking. Complete studies of the large area III/V oxidized SBRs should be performed. Currently, pump-probe has only been performed at 1550 nm. This should be done at 1300 nm and 800 nm, so that the characteristics of the absorbers at different wavelengths can be compared. The SBRs should be systematically tested in lasers, including the Cr^{4+}:YAG, and measurements of the nonsaturable loss should be performed.

The efficiency of the highly nondegenerate four-wave mixing demonstrated in microstructure fiber could be improved with the design of an improved fiber. A redesigned fiber should maximize the interaction length of signal and pump (preferably to the full length of the 18 cm taper). The nonlinearity could be enhanced with the use of a different materials system also.

Research on bismuth-oxide fiber should focus on several issues. Excited-state absorption limits the efficiency and power output of the amplifiers. While the efficiency of these amplifiers is greater than that of conventional amplifiers in the L-band, it is below conventional amplifiers in the C-band. By improving this, bismuth-oxide amplifiers could become very attractive for telecommunications applications. The highly nonlinear bismuth-oxide fiber was quite fragile, and difficult to prepare, due a core and cladding asymmetrically placed in an outer jacket. Additionally, it was difficult to suppress unwanted cladding modes. The high normal dispersion of the fiber placed the ultimate limit on spectral broadening, while controlling the supercontinuum generation. Fiber, which still has normal dispersion, but less of it, will probably enable even broader supercontinuum.

Devices and fibers should be fabricated out of chalcogenide glasses. The nonlinearities measured are almost three orders of magnitude larger than that of fused silica. The real advantage of chalcogenides may be in the fabrication of devices for integrated optics such as switches.

While this a long list of future work, the author hopes that the experiments described in this thesis will make a contribution to the field of ultrafast optics.

REFERENCES

[1] A. R. Chraplyvy and R. W. Tkach, “Terabit/second transmission experiments,” IEEE J. Quantum. Electron. **34,** 2103-2105 (1998).

[2] I. N. Duling, “Subpicosecond all-fibre erbium lasers,” Electron. Lett. **27**, 544-545 (1991).

[3] R. A. Barry, V. W. S. Chan, K. L. Hall, E. S. Kintzer, J. D. Mores, K. A. Rauschenbach, E. A. Swanson, L. E. Adams, C. R. Doerr, S. G. Finn, H. A. Haus, E. P. Ippen, W. S. Wong, and M. Haner, “All-optical network consortium-ultrafast TDM networks,” IEEE Select. Areas in Comm. **14**, 999-1013 (1996).

[4] V. W. S. Chan, K. L. Hall, E. Modiano, and K. A. Rauschenbach, “Architectures and technologies for high-speed optical data networks,” J. Lightwave Tech. **16**, 2146-2168 (1998).

[5] D. J. Jones, S. A. Diddams, J. K. Ranka, A. Stentz, R. S. Windeler, J. L. Hall, and S. T. Cundiff, “Carrier-envelope phase control of femtosecond mode-locked lasers and direct optical frequency synthesis,” Science **288**, 635-639 (2000).

[6] B. R. Washburn, S. A. Diddams, N. R. Newbury, J. W. Nicholson, M. F. Yan, and C. G. Jorgenson, “Phase-locked, erbium-fiber-laser-based frequency comb in the near infrared,” Opt. Lett. **29**, 250-252 (2004).

[7] S. A. Diddams, D. J. Jones, J. Ye, S. T. Cundiff, J. L. Hall, J. K. Ranka, R. S. Windeler, R. Holzwarth, T. Udem, and T. W. Hansch, “Direct link between microwave and optical frequencies with a 300 THz femtosecond laser comb,” Phys. Rev. Lett. **84**, 5102-5105 (2000).

[8] J. Shah, “Ultrafast Spectroscopy of Semiconductors and Semiconductor Nanostructures,” Springer Series in Solid-State Sciences **115** (1996).

[9] W. Drexler, U. Morgner, F. X. Kaertner, C. Pitris, S. A. Boppart, X. D. Li, E. P. Ippen, and J. G. Fujimoto, “In vivo ultrahigh-resolution optical coherence tomography,” Opt. Lett. **24**, 1221-1223 (1999).

[10] K. Minoshima, A. M. Kowalevicz, E. P. Ippen, and J. G. Fujimoto, “Fabrication of coupled mode photonic devices in glass by nonlinear femtosecond laser materials processing,” Opt. Exp. **10**, 645-652 (2002).

[11] H. A. Haus, “Waves and Fields in Optoelectronics,” Prentice Hall (1984).

[12] H. A. Haus, J. G. Fujimoto, and E. P. Ippen, “Structures for additive pulse mode locking,” J. Opt. Soc. Am. B **8**, 2068-2075 (1991).

[13] O. E. Martinez, R. L. Fork, and J. P. Gordon, “Theory of passively mode-locked lasers including self-phase modulation and group-velocity dispersion,” Opt. Lett. **9**, 156-158 (1984).

[14] M. E. Fermann, M. Hofer, F. Haberl, A. Schmidt, and L. Turi, “Additive-pulse compression mode locking of a neodymium fiber laser,” Opt. Lett. **16**, 244-246 (1991).

[15] H. A. Haus, J. G. Fujimoto, and E. P. Ippen, “Analytic theory of additive pulse and kerr lens modelocking,” IEEE J. Quantum. Electron. **28**, 2086-2096 (1992).

[16] E. P. Ippen, D. J. Eichenberger, and R. W. Dixon, “Picosecond pulse generation by passive modelocking of diode lasers,” Appl. Phys. Lett. **37**, 267-269 (1980).

[17] M. N. Islam, E. R.Sunderman, C. E. Soccolich, I. Bar-Joseph, N.Sauer, and T. Y. Chang, “Color center lasers passively mode-locked by quantum wells,” IEEE J. Quantum. Electron. **25**, 2454-2463 (1989).

[18] E. Lariontsev and V. Serkin, “Possibility of using self-focusing for increasing contrast and narrowing of ultrashort light pulses,” Soviet J. of Quant. Elect. **5**, 796 (1975).

[19] D. E. Spence, P. N. Kean, and W. Sibbett, “60-fsec pulse generation from a self-mode-locked Ti:Sapphire laser,” Opt. Lett. **16**, 42-44 (1991).

[20] F. Salin, J. Squier, and M. Piche, “Mode locking of Ti:Al_2O_3 lasers and self-focusing: a Gaussian approximation,” Opt. Lett. **16**, 1674-1676 (1991).

[21] I. D. Jung, F. X. Kaertner, N. Matuschek, D. H. Sutter, F. Mourier-Genoud, Z. Shi, V. Scheuer, M. Tilsch, T. Tschudi, and U. Keller, “Semiconductor saturable absorber mirrors supporting sub-10-fs pulses,” Appl. Phys. B **65**, 137-150 (1997).

[22] D.H. Sutter, G. Steinmeyer, L. Gallmann, N. Matuschek, F. Morier-Genoud, U. Keller, V. Scheuer, G. Angelow, and T. Tschudi, “Semiconductor saturable-absorber mirror-assisted kerr-lens modelocked Ti:sapphire laser producing pulses in the two-cycle regime,” Opt. Lett. **24**, 631-633 (1999).

[23] M. Zirngibl, L. W. Stulz, J. Stone, J. Hugi, D. DiGiovanni, and P. B. Hansen, “1.2 ps pulses from a passively mode-locked laser diode pumped Er-doped fiber ring laser,” Electron. Lett. **27**, 1734-1735 (1991).

[24] W. H. Loh, D. Atkinson, P. R. Morkel, M. Hopkinson, A. Rivers, A. J. Seeds, and D. N. Payne, “Passively mode-locked Er^{3+} fiber laser using a semiconductor nonlinear mirror,” IEEE Phot. Tech. Lett. **5**, 35-37 (1993).

[25] W. H. Loh, D. Atkinson, P. R. Morkel, M. Hopkinson, A. Rivers, A. J. Seeds, and D. N. Payne, “All solid-state subpicosecond passively mode-locked erbium-doped fiber laser,” Appl. Phys. Lett. **63**, 4-6 (1993).

[26] E. R. Thoen, “Development of ultrashort pulse fiber lasers for optical communication utilizing semiconductor devices,” MIT Doctoral Thesis (2000).

[27] P. Griffiths, “Fourier transform infrared spectrometry,” Wiley-Interscience (1986).

[28] J. C. Diels and W. Rudolph, “Ultrashort laser pulse phenomena,” Academic Press (1996).

[29] J. T. Gopinath, E. R. Thoen, E. M. Koontz, M. E. Grein, L. A. Kolodziejski, and E. P. Ippen, “Recovery dynamics in proton-bombarded semiconductor saturable absorber mirrors,” Appl. Phys. Lett. **78**, 3409-3411 (2001).

[30] J. T. Gopinath, “The effect of proton bombardment on semiconductor saturable absorbers,” MIT S. M. Thesis (2000).

[31] P. Langlois, M. Joschko, E. R. Thoen, E. M. Koontz, F. X. Kaertner, E. P. Ippen, and L. A. Kolodziejski, “High fluence ultrafast dynamics of semiconductor saturable absorber mirrors,” Appl. Phys. Lett. **75**, 3841-3843 (1999).

[32] A. Yariv, “Optical electronics in modern communications,” Oxford University Press (1997).

[33] M. Joschko, P. Langlois, E. R. Thoen, E. M. Koontz, E. P. Ippen, and L. A. Kolodziejski, “Ultrafast hot-carrier dynamics in semiconductor saturable absorbers,” Appl. Phys. Lett. **76**, 1383-1385 (2000).

[34] E. R. Thoen, E. M. Koontz, M. Joschko, P. Langlois, T. R. Schibli, F. X. Kaertner, E. P. Ippen, and L. A. Kolodziejski, “Two-photon absorption in semiconductor saturable absorber mirrors,” Appl. Phys. Lett. **74**, 3927-3929 (1999).

[35] P. Grenier and F. F. Whitaker, “Subbandgap dynamics in low-temperature grown GaAs,” Appl. Phys. Lett. **70**, 1998-2000 (1997).

[36] E. R. Thoen, E. M. Koontz, D. J. Jones, D. Barbier, F. X. Kaertner, E. P. Ippen, and L. A. Kolodziejski, “Erbium-ytterbium waveguide laser mode-locked with a semiconductor saturable absorber mirror,” IEEE Phot. Tech. Lett. **12**, 149-151 (2000).

[37] J. B. Schlager, B. E. Callicoatt, R. P. Mirin, N. A. Sanford, D. J. Jones, and J. Ye, “Passively mode-locked glass waveguide laser with 14-fs timing jitter,” Opt. Lett. **28**, 2411-2413 (2003).

[38] F. J. Grawert, F. Ö. Ilday, D. Kielpinski, J. T. Gopinath, L. A. Kolodziejski, G. S. Petrich, E.P. Ippen and F. X. Kaertner, “Q-switch suppression in an Er-doped waveguide laser with an intracavity loss modulator,” Submitted to Conference on Advanced Solid-State Lasers (ASSP) (2004).

[39] F. X. Kaertner, I. D. Jung, and U. Keller, “Soliton mode-locking with saturable absorbers,” IEEE. J. Sel. Topics in Quant. Electron. **2**, 540-556 (1996).

[40] C. Honninger, R. Paschotta, F. Morier-Genoud, M. Moser, and U. Keller, “Q-switching stability limits of continuous-wave passive mode locking,” J. Opt. Soc. Am. B **46,** 46-56 (1999).

[41] T. R. Schibli, E. R. Thoen, F. X. Kaertner, and E. P. Ippen, “Suppression of Q-switched mode locking and break-up into multiple pulses by inverse saturable absorption,” Appl. Phys. B **70**, 41-49 (2000).

[42] T. R. Schibli, K. E. Robinson, U. Morgner, F. X. Kaertner, and S. Mohr, “Suppression of Q-switching instabilities in passively high repetition-rate and high-power lasers,” Advanced Solid-State Lasers, WD6, 498-504 (2002).

[43] C. Chudoba, J. G. Fujimoto, E. P. Ippen, H. A. Haus, U. Morgner, F. X. Kartner, V. Scheuer, G. Angelow, and T. Tschudi, “All-solid-state Cr:Forsterite laser generating 14-fs pulses at 1.3 μm,” Opt. Lett. **26**, 292-294 (2001).

[44] D. J. Ripin, C. Chudoba, J. T. Gopinath, J. G. Fujimoto, E. P. Ippen, U. Morgner, F. X. Kartner, V. Scheuer, G. Angelow, and T. Tschudi, “Generation of 20-fs pulses by a prismless Cr^{4+}:YAG laser,” Opt. Lett. **27**, 61-63 (2002).

[45] U. Keller, K. J. Weingarten, F. X. Kaertner, D. Kopf, B. Braun, I. D. Jung, R. Fluck, C. Honninger, N. Matuschek, and J. Aus der Au, “Semiconductor saturable absorber mirrors (SESAM's) for femtosecond to nanosecond pulse generation in solid-state lasers,” IEEE. J. Select. Top. Quant. Electron. **2**, 435-453 (1996).

[46] S. Tsuda, W. H. Knox, S. T. Cundiff, W. Y. Jan, and J. E. Cunningham, “Mode-locking ultrafast solid-state lasers with saturable Bragg reflectors,” IEEE. J. Select. Top. Quant. Electron. **2**, 454-464 (1996).

[47] S. Schon, L. Gallmann, M. Haiml, and U. Keller, “Fluoride SESAM for ultrabroadband pulse generation,” Conf. on Lasers and Electro-Optics (CLEO), CWB2, 314-315 (2001).

[48] A. Owyoung, R. W. Hellwarth, and N. George, “Intensity-Induced Changes in Optical Polarizations in Glasses,” Phys. Rev. B **5**, 628-633 (1972).

[49] P. M. W. French, N. H. Rizci, J. R. Taylor, and A. V. Shestakov, “Continuous-wave mode-locked Cr^{4+}:YAG lasers,” Opt. Lett. **18**, 39-41 (1993).

[50] A. Sennaroglu, C. R. Pollock, and H. Nathel, “Continuous-wave self-mode-locked operation of a femtosecond Cr^{4+}:YAG laser,” Opt. Lett. **19**, 390-392 (1994).

[51] Y. P. Tong, P. M. W. French, J. R. Taylor and J. G. Fujimoto, “All-solid-state femtosecond sources in the near infrared,” Opt. Comm. **136**, 235-238 (1997).

[52] F. X. Kaertner, N. Matuschek, T. Schibli, U. Keller, H. A. Haus, C. Heine, R. Morf, V. Scheuer, M. Tilsch, and T. Tschudi, “Design and fabrication of double-chirped mirrors,” Opt. Lett. **22**, 831-833 (1997).

[53] B. C. Collings, J. B. Stark, S. Tsuda, W. H. Knox, J. E. Cunningham, W. Y. Jan, R. Pathak, and K. Bergman, “Saturable Bragg reflector self-starting passive mode locking

of a Cr^{4+}:YAG laser pumped with a diode-pumped Nd:YVO_4 laser," Opt. Lett. **21**, 1171-1173 (1996).

[54] S. Spalter, M. Bohm, M. Burk, B. Mikulla, R. Fluck, I. D. Jung, G. Zhang, U. Keller, A. Sizmann, and G. Leuch, Self-starting soliton-modelocked femtosecond Cr(4+):YAG laser using an antiresonant Fabry-Pérot saturable absorber," Appl. Phys. B **65**, 335-338 (1997).

[55] M. J. Hayduk, S. T. Johns, M. F. Krol, C. R. Pollock, and R. P. Leavitt, "Self-starting passively mode-locked tunable femtosecond Cr^{4+}:YAG laser using a saturable absorber mirror," Opt. Comm. **137**, 55-58 (1997).

[56] Y. Chang, R. Maciejko, R. Leonelli, and A. S. Thorpe, "Self-starting passively mode-locked tunable Cr^{4+}: yttrium–aluminum–garnet laser with a single prism for dispersion compensation," Appl. Phys. Lett. **73**, 2098-2100 (1998).

[57] Z. Zhang, T. Nakagawa, K. Torizuka, T. Sugaya, and K. Kobayashi, "Self-starting mode-locked Cr^{4+} YAG laser with a low-loss broadband semiconductor saturable-absorber mirror," Opt. Lett. **24,** 1768-1770 (1999).

[58] Z. Zhang, T. Nakagawa, K. Torizuka, T. Sugaya, and K. Kobayashi, "Gold-reflector-based semiconductor saturable absorber mirror for femtosecond mode-locked Cr^{4+}:YAG lasers," Appl. Phys. B **70**, S59-S62 (2000).

[59] D. J. Ripin, J. T. Gopinath, H. M. Shen, A. A. Erchak, G. S. Petrich, L. A. Kolodziejski, F. X. Kaertner, and E. P. Ippen, "Oxidized GaAs/AlAs mirror with a quantum-well saturable absorber for ultrashort-pulse Cr^{4+}:YAG laser," Opt. Comm. **214**, 285-289 (2002).

[60] K. D. Choquette, K. M. Geib, C. I. H. Ashby, R. D. Twesten, O. Blum, H. Q. Hou, D. M. Follstaedt, B. E. Hammons, D. Mathes, and R. Hull, "Advances in selective wet oxidation of AlGaAs alloys," IEEE J. Select. Top. Quant. Electron. **3**, 916-926 (1997).

[61] H. M. Shen, "Ultrashort pulse generation with a solid state Cr^{4+}:YAG laser," MIT S. M. Thesis (2000).

[62] D. T. Reid, W. Sibbett, J. M. Dudley, L. P. Barry, B. Thomsen, and J. D. Harvey, "Commercial semiconductor devices for two photon absorption autocorrelation of ultrashort light pulses," Opt. and Phot. News **9**, SUPL6-8 (1998).

[63] S. N. Tandon, J. T. Gopinath, H. M. Shen, G. S. Petrich, L. A. Kolodziejski, F. X. Kaertner, and E. P. Ippen, "Large-area broadband saturable bragg reflectors by use of oxidized AlAs," Opt. Lett. **21**, 2551-2553 (2004).

[64] S. N. Tandon, J. T. Gopinath, A. A. Erchak, G. S. Petrich, L. A. Kolodziejski, and E. P. Ippen. "Large Area Oxidation of AlAs Layers for Dielectric Stacks and Thick Buried Oxides," J. of Electron. Mat. **33**, 774-779 (2004).

[65] T. R. Schibli, J. Kim, O. Kuzucu, J. T. Gopinath, S. N. Tandon, G. S. Petrich, L. A. Kolodziejski, J. G. Fujimoto, E. P. Ippen, and F. X. Kaertner, "Attosecond active synchronization of passively mode-locked lasers by balanced cross correlation," Opt. Lett. **28**, 947-949 (2003).

[66] J. -W. Kim, “Toward single-cycle optical pulses,” MIT S. M. Thesis (2004).

[67] M. Dinu, F. Quochi, and H. Garcia, “Third-order nonlinearities in silicon at telecom wavelengths,” Appl. Phys. Lett. **82**, 2954-2956 (2003).

[68] M. D. Dvorak and B. L. Justus, “Z-scan studies of nonlinear absorption and refraction in bulk, undoped InP,” Opt. Comm. **114**, 147-150 (1995).

[69] J. W. Sickler, J. T. Gopinath, S. N. Tandon, H. Sotobayashi, G. S. Petrich, E. P. Ippen, and L. A. Kolodziejski, “Femtosecond laser using broadband erbium-doped bismuth oxide gain fiber,” Conf. on Lasers and Electro-Optics (CLEO), CThK6 (2004).

[70] F. J. Grawert, S. Akiyama, J. T. Gopinath, F. Ö. Ilday, H. Shen, J. Liu, K. Wada, L. C. Kimerling, E. P. Ippen, and F. X. Kärtner, “220 fs Er-Yb:glass laser mode-locked by a broadband low-loss Si/Ge saturable absorber,” to be published in Opt. Lett. (2004).

[71] H.-C. Luan, D. R. Lim, K. K. Lee, K. M. Chen, J. G. Sandland, K. Wada, and L. C. Kimerling, “High-quality Ge epilayers on Si with low threading-dislocation densities,” Appl. Phys. Lett. **75**, 2909-2911 (1997).

[72] G. W. Bryant, “Two-photon absorption in Ge: Band effects,” Phys. Rev. B **22**, 1992-1999 (1980).

[73] G. Wasik, F. W. Helbing, F. Koenig, A. Sizmann, and G. Leuchs, “Bulk Er:Yb:glass soliton femtosecond laser,” Conf. on Lasers and Electro-Optics (CLEO), CMA4 (2001).

[74] G. J. Spuehler, L. Gallman, R. Fluck, G. Zhang, L. R. Brovelli, C. Harder, P. Laporta, and U. Keller, “Passively modelocked diode-pumped erbium-ytterbium glass laser using a semiconductor saturable absorber mirror,” Elect. Lett. **35**, 567-569 (1999).

[75] G. P. Agrawal, “Nonlinear fiber optics,” Academic Press (1995).

[76] C. Dorman, I. Kucukkara, and J. P. Marangos, “Measurement of high conversion efficiency to 123.6-nm radiation in a four-wave-mixing scheme enhanced by electromagnetically induced transparency,” Phys. Rev. A **61**, 013802-013806 (1999).

[77] R. W. Hellwarth, “Generation of time-reversed wave fronts by nonlinear refraction,” J. Opt. Soc. Am. B **67**, 1-3 (1977).

[78] R. E. Slusher, L. W. Hollberg, B. Yurke, J. C. Mertz, and J. F. Valley, “Observation of squeezed states generated by four-wave mixing in an optical cavity,” Phys. Rev. Lett. **55**, 2409-2412 (1985).

[79] M. D. Levenson, R. M. Shelby, and S. H. Perlmutter, “Squeezing of classical noise by nondegenerate four-wave mixing in an optical fiber,” Opt. Lett. **10**, 514-516 (1985).

[80] S. A. Diddams, D. J. Jones, J. Ye, S. T. Cundiff, J. L. Hall, J. K. Ranka, and R. S. Windeler, “Direct RF to optical frequency measurements with a femtosecond laser comb,” IEEE Trans. Instrum. Meas. **50**, 552-555 (2001).

[81] R. H. Stolen, J. E. Bjorkholm, and A. Ashkin, “Phase-matched three-wave mixing in silica fiber optical waveguides,” Appl. Phys. Lett. **24**, 308-310 (1974).

[82] K. O. Hill, D. C. Johnson, and B. S. Kawasaki, “Efficient conversion of light over a wide spectral range by four-photon mixing in a multimode graded-index fiber,” Appl. Opt. **20**, 1075-1079 (1981).

[83] J. E. Sharping, M. Fiorentino, A. Coker, P. Kumar, and R. S. Windeler, “Four-wave mixing in microstructure fiber,” Opt. Lett. **26**, 1048-1050 (2001).

[84] Z. Su, X. Zhu and W. Sibbett, “Conversion of femtosecond pulses from the 1.5- to the 1.3- μm region by self-phase-modulation-mediated four-wave mixing,” J. Opt. Soc. Am. B **10**, 1050-1053 (1993).

[85] P. Russell, “Holey fiber concept spawns optical-fiber renaissance,” Las. Foc. World **38**, 77-82 (2002).

[86] C. Kerbage and B. J. Eggleton, “Microstructured optical fibers,” Opt. and Phot. News **13**, 39-42 (2002).

[87] F. G. Omenetto, A. J. Taylor, M. D. Moores, J. Arriaga, J. C. Knight, W. J. Wadsworth and P. Russell, “Simultaneous generation of spectrally distinct third harmonics in a photonic crystal fiber,” Opt. Lett. **26**, 1158-1160 (2001).

[88] J. K. Ranka, R. S. Windeler, and A. J. Stentz, “Optical properties of high-delta air-silica microstructure optical fibers,” Opt. Lett. **25**, 796-798 (2000).

[89] J. K. Chandalia, B. J. Eggleton, R. S. Windeler, S. G. Kosinski, X. Liu, and C. Xu, “Adiabatic coupling in tapered air-silica microstructured optical fiber,” IEEE Phot. Tech. Lett. **13**, 52-54 (2001).

[90] X. Liu, C. Xu, W. H. Knox, J. K. Chandalia, B. J. Eggleton, S. G. Kosinski, and R. S. Windeler, “Soliton self-frequency shift in a short tapered air-silica microstructure fiber,” Opt. Lett. **9**, 358-360 (2001).

[91] K. S. Abedin, J. T. Gopinath, E. P. Ippen, C. E. Kerbage, R. S. Windeler, and B. J. Eggleton, “Highly nondegenerate femtosecond four-wave mixing in tapered microstructure fiber,” Appl. Phys. Lett. **81**, 1384-1387 (2002).

[92] J. D. Kafka, M. L. Watts, and J. W. Pieterse, “Synchronously pumped optical parametric oscillators with LiB_3O_5,” J. Opt. Soc. Am. B **12**, 2147-2157 (1995).

[93] A. Ghatak and K. Thyagarajan, “Introduction to Fiber Optics,” Cambridge University Press (1998).

[94] Q. Ye, C. Xu, X. Liu, W. H. Knox, M. F. Yan, R. S. Windeler, and B. Eggleton, “Dispersion measurement of tapered air-silica microstructure fiber by white-light interferometry,” Appl. Opt. **41**, 4467-70 (2002).

[95] R. H. Stolen and J. E. Bjorkholm, “Parametric amplification and frequency conversion in optical fibers,” IEEE J. Quant. Electron. **18**, 1062-1072 (1982).

[96] G. A. Nowak, Y. -H. Kao, T. J. Xia, and M. N. Islam, “Low-power high-efficiency wavelength conversion based on modulational instability in high-nonlinearity fiber,” Opt. Lett. **25**, 936-938 (1998).

[97] A. Ferrando, E. Silvestre, J. J. Miret, and P. Andres, “Nearly zero ultraflattened dispersion in photonic crystal fibers,” Opt. Lett. **25**, 790-792 (2000).

[98] J. Hecht, “City of light,” Oxford University Press (1999).

[99] N. Sugimoto, “Ultrafast optical switches and wavelength division multiplexing (WDM) amplifiers based on bismuth-oxide glasses,” J. Am. Ceram. Soc. **85**, 1083-1088 (2002).

[100] Y. Kuriowa, N. Sugimoto, K. Ochiai, S. Ohara, Y. Fukasawa, S. Ito, S. Tanabe, and T. Hanada, “Fusion spliceable and high efficient Bi_2O_3-based EDF for short length and broadband amplification pumped at 1480 nm,” presented at Optical Fiber Communication Conference (OFC), TuI5 (2001).

[101] K. Taira, K. Kikuchi, and N. Sugimoto, “Dispersion and pulse amplification characteristics of bismuth oxide-based erbium-doped fiber amplifiers,” Optical Amplifiers and Applications Conference (OAA), OTuC2 (2002).

[102] K. Kikuchi, K. Taira, and N. Sugimoto, “Highly nonlinear bismuth-oxide-based glass fibres for all-optical signal processing,” Electron. Lett. **38**, 156-157 (2002).

[103] N. Sugimoto, T. Nagashima, T. Hasegawa, S. Ohara, K. Taira, and K. Kikuchi, “Bismuth-based optical fiber with nonlinear coefficient of 1360 $W^{-1}km^{-1}$,” Optical Fiber Communication Conference Postdeadline, PDP26 (2004).

[104] E. Desurvire, “Erbium-doped fiber amplifiers, principles and applications,” John Wiley and Sons (2002).

[105] S. Aozasa, H. Masuda, H. Ono, T. Sakamoto, T. Kanamori, Y. Ohishi, and M. Shimizu, “1480-1510 nm-band Tm-doped fiber amplifier (TDFA) with a high power conversion efficiency of 42%,” Optical Fiber Communication Conference (OFC), PD1 (2001).

[106] M. Yamada, A. Mori, K. Kobayashi, H. Ono, T. Kanamori, K. Oikawa, Y. Nishida, and Y. Ohishi, “Gain-flattened tellurite-based EDFA with a flat amplification bandwidth of 76 nm,” IEEE Photon. Tech. Lett. **10**, 1244-1246 (1998).

[107] H. Sotobayashi, J. T. Gopinath, and E. P. Ippen, “23 cm long Bi_2O_3-based EDFA for picosecond pulse amplification with an 80 nm gain-bandwidth,” IEE Elect. Lett. **39**, 1374-1376 (2003).

[108] J. T. Gopinath, H. Sotobayashi, and E. P. Ippen, “Broadband amplification of picosecond pulses in a 23 cm length of Bi_2O_3-based Erbium-doped fiber,” OSA TOPS **92** (Optical Amplifiers and Their Applications), 50-53 (2003).

[109] K. Tamura, Y. Kimura, and M. Nakazawa, “Femtosecond pulse generation over 82 nm wavelength span from passively modelocked erbium-doped fibre laser,” IEE Electron. Lett. **31**, 1062-1063 (1995).

[110] H. Sotobayashi, J. T. Gopinath, E. M. Koontz, L. A. Kolodziejski, and E. P. Ippen, “Wavelength tunable passively mode-locked bismuth oxide-based erbium-doped fiber laser,” Opt. Comm. **237**, 399-403 (2004).

[111] B. C. Collings, K. Bergmann, S. T. Cundiff, S. Tsuda, J. N. Kutz, J. E. Cunningham, W. Y. Jan, M. Koch, and W. H. Knox, “Short cavity erbium/ytterbium fiber lasers mode-

locked with a saturable Bragg reflector," IEEE J. Sel. Top. Quant. Electron. **4**, 1065-1075 (1997).

[112] P. T. Rakich, J. T. Gopinath, H. Sotobayashi, C. W. Wong, S. G. Johnson, J. D. Joannopoulos, and E. P. Ippen, "Broadband supercontinuum-based measurements of high-index contrast photonic bandgap devices from 1 to 2 μm," Annual Meeting of the Lasers and Electro-Optic Society (LEOS), ThI3 (2004).

[113] R. T. Neal, M. D. C. Charlton, G. J. Parker, C. E. Finlayson, M. C. Netti, and J. J. Baumberg, "Ultrabroadband transmission measurements on waveguides of silicon-rich silicon dioxide," Appl. Phys. Lett. **83**, 4598-4600 (2003).

[114] W. J. Tomlinson, R. H. Stolen, and C. V. Shank, "Compression of optical pulses chirped by self-phase modulation in fibers," J. Opt. Soc. Am. B. **l1**, 139-149 (1984).

[115] J. C. Knight, J. Arriaga, T. A. Birks, A. Blanch-Ortigosa, W. J. Wadsworth, and P. St. J. Russell, "Anomalous dispersion in photonic crystal fiber," IEEE Phot. Tech. Lett. **12**, 807-809 (2000).

[116] H. Ebendorff-Heidepriem, P. Petropoulos, S. Asimakis, V. Finazzi, R. C. Moore, K. Frampton, F. Koizumi, D. J. Richardson, and T. M. Monro, "Bismuth glass fibers with high nonlinearity," Opt. Exp. **12**, 5082-5087 (2004).

[117] R. E. Slusher, G. Lenz, J. Hodelin, J. Sanghera, L. B. Shaw, and I. D. Aggarwal, "Large Raman gain and nonlinear phase shifts in high-purity As_2Se_3 chalcogenide fibers," J. of the Opt. Soc. of Am. B **21**, 1146-1155 (2004)

[118] K. Kikuchi, K. Taira, and N. Sugimoto, "Highly nonlinear bismuth oxide-based glass fibres for all-optical signal processing," Elect. Lett. **38**, 156-157 (2002).

[119] N. Sugimoto, T. Nagashima, T. Hasegawa, S. Ohara, K. Taira, and K. Kikuchi, "Bismuth-based optical fiber with nonlinear coefficient of 1360 $W^{-1}km^{-1}$," Optical Fiber Communication Conference (OFC) Postdeadline, PDP26 (2004).

[120] J. T. Gopinath, H. M. Shen, H. Sotobayashi, E. P. Ippen, T. Hasegawa, T. Nagashima, and N. Sugimoto, "Highly nonlinear bismuth-oxide fiber for smooth supercontinuum generation at 1.5 μm," Opt. Exp. **12**, 5697-5702 (2004).

[121] M. Nisoli, S. Stagira, S. De Silvestri, O. Svelto, G. Valiulis, and A. Varanavicius, "Parametric generation of high-energy 14.5-fs light pulses at 1.5 μm," Opt. Lett. **23**, 630-632, (1998).

[122] Y. Matsui, M. D. Pelusi, and A. Suzuki, "Generation of 20-fs optical pulses from a gain-switched laser diode by a four-stage soliton compression technique," IEEE Phot. Tech. Lett. **11**, 1217-1219 (1999).

[123] K.L. Corwin, N.R. Newbury, J.M. Dudley, S. Coen, S.A. Diddams, B.R. Washburn, K. Weber, and R.S. Windeler, "Fundamental amplitude noise limitations to supercontinuum spectra generated in a microstructured fiber," Appl. Phys. B **B77**, 269-277 (2003).

[124] S. Taccheo and L. Boivin, “Investigation and design rules of supercontinuum sources for WDM applications,” Optical Fiber Communication Conference (OFC), ThA1 (2000).

[125] J. T. Gopinath, H. M. Shen, H. Sotobayashi, E. P. Ippen, T. Hasegawa, T. Nagashima, and N. Sugimoto, “Highly nonlinear bismuth-oxide fiber for supercontinuum generation and femtosecond pulse compression,” submitted to J. Light. Tech. (2004).

[126] E. Hecht, “Optics,” Addison-Wesley (2002).

[127] W. Nicholson, J. Jasapara, W. Rudolph, F. G. Omenetto, and A. J. Taylor, “Full-field characterization of femtosecond pulses by spectrum and cross-correlation measurements,” Opt. Lett. **24**, 1774-1776 (1999).

[128] V. Mizrahi, K. W. DeLong, G. I. Stegeman, M. A. Saifi, and M. J. Andrejco, “Two-photon absorption as a limitation to all-optical switching,” Opt. Lett. **14**, 1140-1142 (1989).

[129] G. Lenz, J. Zimmerman, T. Katsufuji, M. E. Lines, H. Y. Hwang, S. Spalter, R. E. Slusher, S. -W. Cheong, J. S. Sanghera, and I. D. Aggarwal, “Large kerr effect in bulk Se-based chalcogenide glasses,” Opt. Lett. **25**, 254-256 (2000).

[130] J. M. Harbold, F. Ö. Ilday, F. W. Wise, and B. G. Aitken, “Highly nonlinear Ge-As-Se and Ge-As-S-Se glasses for all-optical switching,” IEEE Phot. Technol. Lett. **14**, 822-824 (2002).

[131] F. Smektala, C. Quémard, V. Couderc, and A. Barthélémy, “Non-linear optical properties of chalcogenide glasses measured by z-scan,” J. Non-Cryst.Solids **274**, 232-237 (2000).

[132] C. Quémard, F. Smektala, V. Couderc, A. Barthélémy, and J. Lucas, “Chalcogenide glassses with high nonlinear optical properties for telecommunications,” J. Phys.and Chem. Solids **62**, 1435-1440 (2001).

[133] K. Uchiyama, T. Morioka, M. Saruwatari, M. Asobe, and T. Ohara, “Error free all-optical demultiplexing using a chalcogenide glass fibre based nonlinear optical loop mirror,” Electron.Lett. **32**, 1601-1602 (1996).

[134] P. A. Thielen, L. B. Shaw, P. C. Pureza, V. Q. Nguyen, J. S. Sanghera, and I. D. Aggarwal, “Small-core As-Se fiber for Raman amplification,” Opt. Lett. **28**, 1406-1408 (2003).

[135] B. Temelkuran, S. D. Hart, G. Benoit, J. D. Joannopoulos, and Y. Fink, “Wavelength-scalable hollow optical fibres with large photonic bandgaps for CO_2 laser transmission,” Nature **420**, 650-653 (2002).

[136] S. Spalter, H. Y. Hwang, J. Zimmerman, G. LEnz, T. Katsufuji, S. -W. Cheong, and R. E. Slusher, “Strong self-phase modulation in planar chalcogenide waveguides,” Opt. Lett. **27**, 363-365 (2002).

[137] Y. Ruan, W. Li, R. Jarvis, N. Madsen, A. Rode, and B. Luther-Davies, “Fabrication and characterization of low loss rib chalcogenide waveguides made by dry etching,” Opt. Exp. **12**, 5140-5145 (2004).

[138] B. Luther-Davies, D. Freeman, Y. Ruan, N. Madsen, S. Madden, R. Jarvis, A. V. Rode, and M. Samoc, “Chalcogenide Glass Photonic Devices,” Annual Meeting of Lasers and Electro-Optic Society (LEOS), ThV1 (2004).

[139] J. T. Gopinath, M. Soljacic, E. P. Ippen, V. N. Flufyigin, W. A. King, and M. Shurgalin, “Third order nonlinearities in Ge-As-Se-based glasses for telecommications applications,” J. Appl. Phys. **96**, 1-3 (2004).

[140] Amorphous Materials website, “http://amorphousmaterials.com/Amtir-1.htm”.

[141] W. A. King, A. G. Clare, and W. C. LaCourse, “Laboratory preparation of highly pure As_2Se_3 glass,” J. Non-Cryst. Solids **181**, 231-237 (1995).

[142] J. Tauc, “Amorphous and liquid semiconductors,” Plenum (1974).

[143] N. F. Nott and E. A. Davis, “Electronic processes in noncrystalline materials,” Oxford University Press (1979).

[144] M. Sheik-Bahae, A. A. Said, T. Wei, D. J. Hagan, and E. W. Van Stryland, “Sensitive measurement of optical nonlinearities using a single beam,” IEEE J. Quantum Electron. **26**, 760-769 (1990).

[145] Y. Choi, J.-H. Park. M. R. Kim, W. Jhe, and B. K. Rhee, “Z-scan using circularly symmetric beams,” Appl. Phys. Lett. **78**, 856-858 (2001).

[146] M. Dinu, F. Quocchi, and H. Garcia, “Third-order nonlinearities in silicon at telcom wavelengths,” Appl. Phys. Lett. **82**, 2954-2956 (2002).

[147] J. M. Harbold, F. O. Ilday, F. W. Wise, J. S. Sanghera, V. Q. Nguyen, L. B. Shaw, and I. D. Aggarwal, “Highly nonlinear As-S-Se glasses for all-optical switching,” Opt. Lett. **27**, 119-121 (2002).

[148] Z. S. Borisova, “Glassy semiconductors,” Plenum (1981).

[149] W.-Z. Lin, R. Shoenlein, J. G. Fujimoto, and E. P. Ippen, “Femtosecond absorption saturation studies of hot carriers in GaAs and AlGaAs,” IEEE J. of Quant. Electron. **24**, 267-275 (1988).

[150] S. Arlt, U. Siegner, J. Kunde, F. Morier-Genoud, and U. Keller, “Ultrafast dephasing of continuum transitions in bulk semiconductors,” Phys. Rev. B **B59**, 14860-14863, (1999).

[151] F. Ganikhanov, K. C. Burr, and C. L. Tang, “Ultrafast dynamics of holes in GaAs probed by two-color femtosecond spectroscopy,” Appl. Phys. Lett. **73**, 64-67 (1998).

[152] K. L. Hall, G. Lenz, A. M. Darwish, and E. P. Ippen, “Subpicosecond gain and index nonlinearities in InGaAsP diode lasers,” Opt. Comm. **111**, 589-612 (1994).

[153] K. Ogawa, Y. Matsui, T. Itatani, and K. Ouchi, “Carrier relaxation in an InP/InGaAs nonlinear bragg reflector,” Appl. Phys. Lett. **73**, 297-299 (1998).

APPENDIX A: SATURABLE ABSORBER SAMPLE DETAILS

A.1 Abstract

Details of the saturable absorbers fabricated for this thesis are listed below. For each structure, I have listed the growth number (record locator for the fabrication group), the fabrication location, the exact structure layer by layer, and summarized characterization results succinctly.

A.2 Saturable absorber structures

Table A.1 SBR structures: name and layer thicknesses. Structures are listed from the surface downwards.

Growth number	Fabrication Location/Fabricator	Structure
R577 (‘SBR I’)	Kolodziejski (Koontz)	15 nm InP 6 nm $In_{0.5}Ga_{0.5}As$ 7 nm InP 6 nm $In_{0.5}Ga_{0.5}As$ 210 nm InP tunable 1.55 μm mirror OR MOCVD 22 pairs: 115 nm GaAs/133 nm AlAs
R579 (‘SBR II’)	Kolodziejski (Koontz)	15 nm InP 5.5 nm $In_{0.5}Ga_{0.5}As$ 7 nm InP 5.5 nm $In_{0.5}Ga_{0.5}As$ 210 nm InP tunable 1.55 μm mirror OR MOCVD 22 pairs: 115 nm GaAs/133 nm AlAs
R581 (‘SBR III’)	Kolodziejski (Koontz)	112 nm InP 6.6 nm $In_{0.5}Ga_{0.5}As$ 7 nm InP 6.6 nm $In_{0.5}Ga_{0.5}As$ 7 nm InP 112.2 nm InP tunable 1.55 μm mirror OR MOCVD 22 pairs: 115 nm GaAs/133 nm AlAs

Table A.1 SBR structures: name and layer thicknesses. Structures are listed from the surface downwards.

Growth number	Fabrication Location/Fabricator	Structure
R582 (‘SBR IV’)	Kolodziejski (Koontz)	98.6 nm InP 6.6 nm $In_{0.5}Ga_{0.5}As$ 7 nm InP 6.6 nm $In_{0.5}Ga_{0.5}As$ 7 nm InP 6.6 nm $In_{0.5}Ga_{0.5}As$ 7 nm InP 6.6 nm $In_{0.5}Ga_{0.5}As$ 98.6 nm InP tunable 1.55 μm mirror OR MOCVD 22 pairs: 115 nm GaAs/133 nm AlAs
R730 (‘SBR V’)	Kolodziejski (Koontz) *also overgrown with 20 λ/2 layer of InP (growth no. R787) *additionally, some pieces proton bombarded with 40 keV 10^{13}, 10^{14}, 10^{15} protons/cm^2	70 nm InP 10 nm $In_{0.5}Ga_{0.5}As$ 7 nm InP 10 nm $In_{0.5}Ga_{0.5}As$ 7 nm InP 10 nm $In_{0.5}Ga_{0.5}As$ 7 nm InP 10 nm $In_{0.5}Ga_{0.5}As$ 7 nm InP 10 nm $In_{0.5}Ga_{0.5}As$ 7 nm InP 10 nm $In_{0.5}Ga_{0.5}As$ 70 nm InP MOCVD 22 pairs: 115 nm GaAs/133 nm AlAs
R749 (‘SBR VI’)	Kolodziejski (Koontz) *also overgrown with 20 λ/2 layer of InP (growth no. R787) *additionally, some pieces proton bombarded with 40 keV 10^{13}, 10^{14}, 10^{15} protons/cm^2	64.4 nm InP 102 nm $In_{0.5}Ga_{0.5}As$ 71 nm InP MOCVD 22 pairs: 115 nm GaAs/133 nm AlAs

Table A.1 SBR structures: name and layer thicknesses. Structures are listed from the surface downwards.

Growth number	Fabrication Location/Fabricator	Structure
R885	Kolodziejski (Petrich/Erchak) *post-growth oxidation to convert AlAs->Al_xO_y	111 nm InP 10 nm $In_{0.5}Ga_{0.5}As$ 111 nm InP 7 pairs: 106 nm GaAs/240 nm AlAs
R921	Kolodziejski (Petrich)	73.5 nm InP 6 pairs: 10 nm $In_{0.5}Ga_{0.5}As$/7 nm InP 147 nm InP 6 pairs: 10 nm $In_{0.5}Ga_{0.5}As$/7 nm InP 73.5 nm InP MOCVD 22 pairs: 115 nm GaAs/133 nm AlAs
R968	Kolodziejski (Petrich/Tandon) *post-growth oxidation to convert AlAs->Al_xO_y	102 nm GaAs 10 nm $In_{0.5}Ga_{0.5}As$ 102 nm GaAs 7 pairs: 111 nm $Al_{0.3}Ga_{0.7}As$/240 nm AlAs
R971	Kolodziejski (Petrich/Tandon) *post-growth oxidation to convert AlAs->Al_xO_y	109 nm InP 10 nm $In_{0.5}Ga_{0.5}As$ 109 nm InP 7 pairs: 111 nm $Al_{0.3}Ga_{0.7}As$/240 nm AlAs
R981	Kolodziejski (Petrich/Tandon) *post-growth oxidation to convert AlAs->Al_xO_y *additionally, some pieces proton bombarded with 40 keV 10^{14} protons/cm^2	68.4 nm InP 6 pairs: 10 nm $In_{0.5}Ga_{0.5}As$/ 7 nm InP 68.4 nm InP 7 pairs: 119 nm $Al_{0.3}Ga_{0.7}As$/259 nm AlAs 119 nm $Al_{0.3}Ga_{0.7}As$

Table A.1 SBR structures: name and layer thicknesses. Structures are listed from the surface downwards.

Growth number	Fabrication Location/Fabricator	Structure
R1014	Kolodziejski (Petrich/Tandon) *post-growth oxidation to convert AlAs->Al_xO_y	68.4nm InP 6 pairs: 10nm $In_{0.5}Ga_{0.5}As$/7nm InP 68.4nm InP 7 pairs: 119nm $Al_{0.3}Ga_{0.7}As$/259nm AlAs 119nm $Al_{0.3}Ga_{0.7}As$
R1021	Kolodziejski (Petrich/Tandon) *post-growth oxidation to convert AlAs->Al_xO_y	50 nm GaAs 6 pair: 12 nm $In_{0.5}Ga_{0.5}As$/9 nm GaAs 50 nm GaAs 7 pairs: 119 nm $Al_{0.3}Ga_{0.7}As$/259 nm AlAs 119 nm $Al_{0.3}Ga_{0.7}As$
R1023	Kolodziejski (Petrich/Tandon) *post-growth oxidation to convert AlAs->Al_xO_y	109 nm InP 10nm $In_{0.5}Ga_{0.5}As$ 109 nm InP 7 pairs: 111 nm $Al_{0.3}Ga_{0.7}As$/240 nm AlAs 111 nm $Al_{0.3}Ga_{0.7}As$
R1027	Kolodziejski (Petrich/Tandon) *post-growth oxidation to convert AlAs->Al_xO_y	67 nm InP 100 nm $In_{0.5}Ga_{0.5}As$ 67 nm InP 7 pairs: 119 nm $Al_{0.3}Ga_{0.7}As$/259 nm AlAs
SOI-PBG3 (Si/Ge absorber)	Kimerling (Akiyama/Liu)	70 nm poly-Si 30 nm SiO_2 40 nm Ge 196 nm SOI (c-Si) 5 pairs: 244 nm SiO_2/100 nm poly-Si 244 nm SiO_2 600 μm bonded Si-wafer

Table A.2 Additional details about the SBR structures listed in Table Table A.1. AR= antireflection-coating, Res= resonant-coating, AR/HR=antireflection-coating (1550nm)/ high-reflection-coating (980 nm).

Growth No.	Intended Laser	Ref.	PL	Mod. Depth/ Recovery time	Coatings	Laser Results
R577	Cr^{4+}:YAG laser		1450 nm	0.4% @ 1450 nm 150 ps	none	
R579	Cr^{4+}:YAG laser		1490 nm	0.6% @ 1470 nm 100 ps	none	
R581	Er-fiber laser	[26]	1547 nm		Res: 213 nm Al_2O_3 117 nm Si 213 nm Al_2O_3 117 nm Si 416 nm Al_2O_3 ---------- AR (1550 nm) λ/4 Al_2O_3 ---------- AR/HR: AR 1550 nm HR 980 nm 306 nm Al_2O_3 444 nm TiO_2 λ/8 950 nm Si λ/4 950 nm Al_2O_3 λ/4 950 nm Si λ/4 950 nm Al_2O_3 λ/8 950 nm Si λ/4 1550 nm TiO_2	
R582	Er-fiber laser, Er:Yb waveguide laser	[31][33][36]	1530 nm	2%@1540 nm, AR 14%@1540 nm, Res	AR, Res coatings of R581	1 ps pulses with Er:Yb waveguide

Table A.2 Additional details about the SBR structures listed in Table Table A.1. AR= antireflection-coating, Res= resonant-coating, AR/HR=antireflection-coating (1550nm)/ high-reflection-coating (980 nm).

Growth No.	Intended Laser	Ref.	PL	Mod. Depth/ Recovery time	Coatings	Laser Results
R730	Er-fiber laser	[29][110]	1650 nm	3% @1540 nm (nonAR) 6%@1540 nm (AR) 40 ps non-proton bombarded	AR $\lambda/4$ Al_2O_3	288 fs pulses at 1600 nm (L-band bismuth-oxide laser)
R749	Er-fiber laser	[29][36]	1580 nm	3% @1540 nm (nonAR) 6%@1540 nm (AR) 40 ps non-proton bombarded	AR $\lambda/4$ Al_2O_3	1 ps pulses with Er:Yb waveguide laser
R921	Er:Yb waveguide laser	[38]	1620 nm	7%@ 1540 nm (no coating) 16%@1540 nm (AR) 18%@1560 nm (Res) 60 ps	AR $\lambda/4$ HfO_2 Resonant: 288 nm SiO_2 119 nm Si 577 nm SiO_2	1-30 ps pulse from Er:Yb waveguide laser
R885	Cr^{4+}:YAG laser	[59]	1540 nm	0.3%@ 1540nm 40 ps	none	35 fs from Cr^{4+}:YAG
R968	Cr^{4+}:YAG laser		too strained to see pl	0.3%@ 1540nm 12 ps	none	
R971	Cr^{4+}:YAG laser		1525 nm	0.3%@ 1540nm >20 ps	none	

Table A.2 Additional details about the SBR structures listed in Table Table A.1. AR= antireflection-coating, Res= resonant-coating, AR/HR=antireflection-coating (1550nm)/ high-reflection-coating (980 nm).

Growth No.	Intended Laser	Ref.	PL	Mod. Depth/ Recovery time	Coatings	Laser Results
R981	bismuth-oxide er-doped fiber laser	[69][63]	1550 nm	1.3%@ 1540 nm 40 ps	AR $\lambda/4$ Al_2O_3	155 fs from bismuth-oxide erbium-doped fiber laser
R1014	bismuth-oxide er-doped fiber laser		1525 nm		none	
R1021	bismuth-oxide er-doped fiber laser		too strained to see pl		none	
R1023	Cr^{4+}:YAG laser		1400 nm	none per-formed - bandedge too short for Cr^{4+}:YAG	none	
R1027	ultrafast pump-probe			3.25%@ 1540 nm	none	
SOI-PBG3 (Si/Ge absorber)	Er:glass laser, Cr^{4+}:YAG laser	[70]		0.13%@15 40 nm <1 ps	none	220 fs from Er:glass laser

APPENDIX B: PULSE COMPRESSION AND ULTRAFAST PUMP-PROBE

B.1 Abstract

In the experiments reported here, pulses have been compressed from 150-fs to 35-fs extracavity. A low-dispersion broadband autocorrelator/pump-probe setup was constructed. Preliminary measurements of ultrafast pump-probe on broadband saturable absorbers will be presented. The fiber was designed and developed by T. Kato, Sumitomo Japan. The broadband absorbers were fabricated by G. Petrich, S. Tandon, L. Kolodziejski, J. Liu, S. Akiyama, F. Grawert, and L. Kimerling. The experiments were performed in collaboration with H. Shen, H. Sotobayashi, and A. Motamedi.

B.2 Background

In Chapter 2, saturable Bragg reflectors were discussed and numerous pump-probe traces were plotted. The different absorbers all have a bitemporal response: a fast component due to carrier-carrier scattering (< 300 fs) and a slow component due to recombination (ps - ns). When pulses are produced from pure saturable absorber modelocking, this fast component plays a major role in pulse shaping. However, the OPO which was used to characterize many of these absorbers produces 150-fs pulses, too long to resolve this fast time constant.

There are not many studies of the relaxation time of carrier-carrier scattering at 1550 nm as short pulses at this wavelength (sub-100-fs) are difficult to achieve. The ultrafast dynamics of GaAs/AlGaAs materials systems have been studied with the aid of colliding-pulse mode-locked dye lasers [149] and Kerr lens modelocked Ti:sapphire lasers [150][151]. Hall et. al [152] investigated ultrafast dynamics with a pump-probe heterodyne technique in 1.5 μm semiconductor optical lasers and amplifiers, extracting an ultrafast time constant of 150 fs, on the order of the color-center laser pulses used. Ogawa et. al. extracted a 100-fs carrier-carrier scattering time in an InP/InGaAs structure, using 150-fs optical parametric oscillator pulses [153].

B.3 Pulse compression and preliminary ultrafast pump-probe results

Short pulses at 1550 nm can be produced through extracavity compression. Several pulse compression techniques exist including soliton compression and fiber-grating compression. In soliton compression, pulses propagate through an anomalous dispersion fiber. The spectrum broadens, while the pulse is compressed through soliton effects. Using this technique, 1-ps pulses were compressed to 20 fs at 1550 nm [122]. However, soliton compressors often suffer from poor pulse quality [75]. An alternative is the fiber-grating compressor. Highly nonlinear normal dispersion fiber is used to broaden the spectrum. The normal dispersion causes the pulse to broaden also, but has the beneficial effect of linearizing the chirp acquired by the pulse. This chirp can be easily compensated with a standard grating compressor (see Figure 4.22 for example) [114].

In this research, a fiber-grating compressor was used to compress the 150-fs OPO pulses. One meter of highly nonlinear fiber from Sumitomo was used (Sumitomo fiber 031512AA-5-1). It had a second order dispersion of 5.4 ps^2/km, a third order dispersion of -0.03 ps^3/km, a mode field diameter of 5.6 μm, an effective area 24 μm^2, an attenuation 0.22 dB/km and a cutoff wavelength of 943 nm (all values at 1550 nm). Simulations using the split-step Fourier method to solve the nonlinear Schroedinger equation for pulse propagation through this fiber were performed. A simulation and experimental spectra are shown in Figure B.1. Good agreement is observed between theory and measurements.

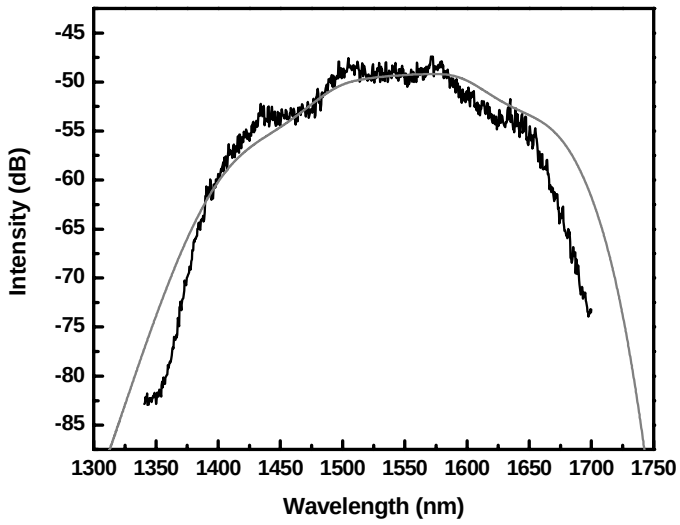

Figure B.1 Simulated (grey) and measured (black) spectra from 1 m of Sumitomo fiber, with an input excitation at 1540 nm with an average power of 70 mW.

The OPO light passes through an isolator, and is focused with an aspheric lens into the fiber. A coupling efficiency of 67% was achieved. Another aspheric lens collimates the output, which is sent to an optical spectrum analyzer, grating compressor, or autocorrelator. Figure B.2 shows the spectral broadening achieved as a function of input power. Table B.1 gives the output pulsewidth and spectral width, as a function of input power. After the fiber, the light is sent to a grating compressor consisting of a pair of parallel gratings separated by 7.0 cm, with 75 line/mm ruling. The compressor is similar to that shown in Figure 4.22. The dispersion of the compressor exactly compensates the second-order dispersion of the fiber, but the achievable compressed pulsewidth is limited by the mismatch in third-order dispersion between the compressor and the fiber ($+1.35 \times 10^4$ fs^3, compressor versus -3×10^4 fs^3, fiber).

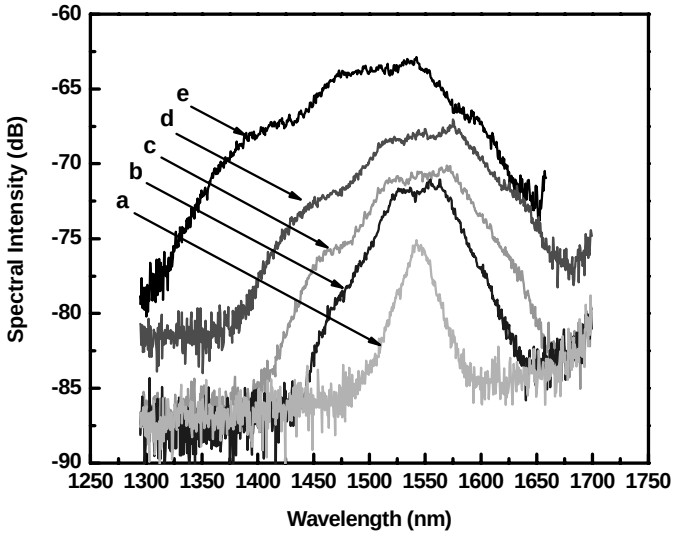

Figure B.2 Output spectrum versus input power for 1 m of highly nonlinear fiber from Sumitomo. The input excitation is 150-fs pulses centered at 1540 nm. Average input powers were: (a) 10 mW (b) 30 mW (c) 50 mW (d) 70 mW (e) 100 mW.

Table B.1 Input power versus spectral width, pulsewidth, and Fourier limit of spectrum.

Input Power (mW)	Output pulsewidth (fs)	Spectrum FWHM (nm)	Fourier limit of spectrum (fs)
100	723	150	21
70	602	110	26
50	510	100	31
30	422	70	41
10	295	20	57

A broadband low dispersion pump-probe setup is used to measure the pulsewidth and perform pump-probe experiments. A schematic of the setup is shown in Figure B.3. Light impinges on a 3 mm thick wedge of CaF_2. A Fresnel reflection from the front surface is used as the probe beam; the pump passes through the wedge. The pump passes through a mechanical chopper and a delay stage. The probe passes through a broadband half-wave plate. A

parabolic mirror focuses the two beams onto either a photodiode (cross-correlation measurement) or a reflective sample (pump-probe). For the pump-probe measurements, the sample is angled, and the reflected probe beam is focused through a Glan-Thompson polarizer to reject any additional scattered pump and onto a GaAs LED detector. The pump and probe powers are in a ratio of ~ 20:1. A typical cross-correlation, with a FWHM of 37 fs, is shown in Figure B.4.

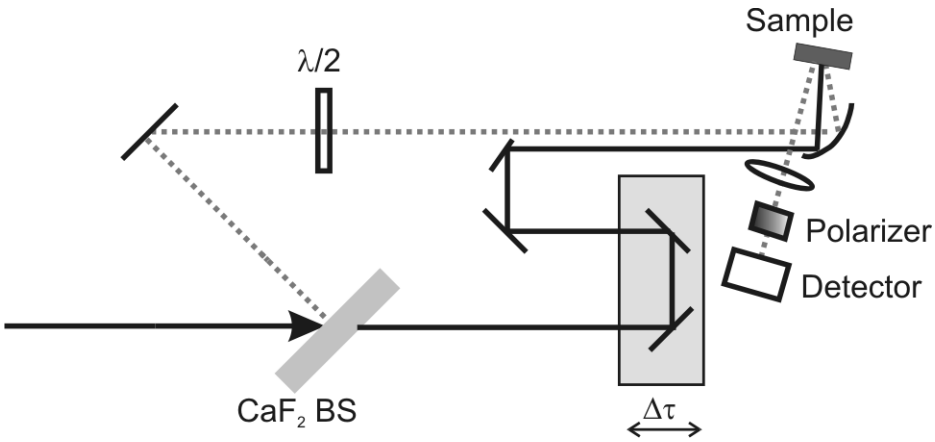

Figure B.3 Setup of ultrafast pump-probe. CaF_2 BS = calcium fluoride beamsplitter, Polarizer = Glan Thompson polarizer, Detector = GaAs LED.

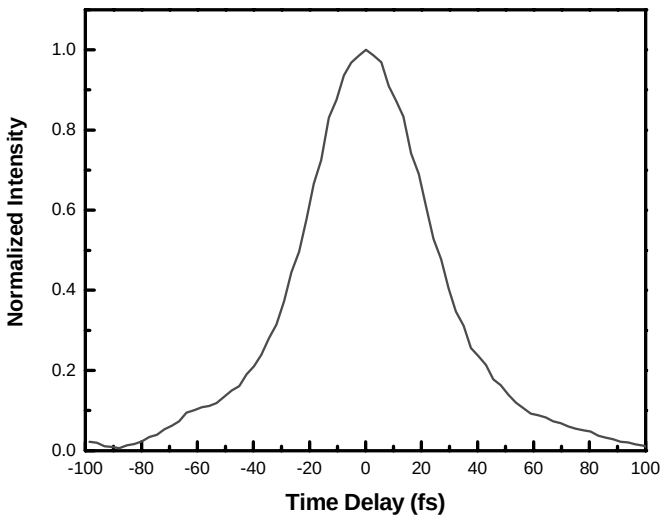

Figure B.4 Typical cross-correlation of compressed OPO pulse at 1540 nm. The FWHM is 37 fs, at an average power of 30 mW.

With these pulses, pump-probe was performed on a variety of SBRs. In Figure B.5, Figure B.6, and Figure B.7, typical traces on several III/V broadband SBRs are shown below, with the cross-correlation of pump and probe superimposed. Figure B.8 shows the laser spectrum superimposed on the passband of a typical broadband 1550 nm III/V SBR. It is clear that the mirror does not filter the spectrum.

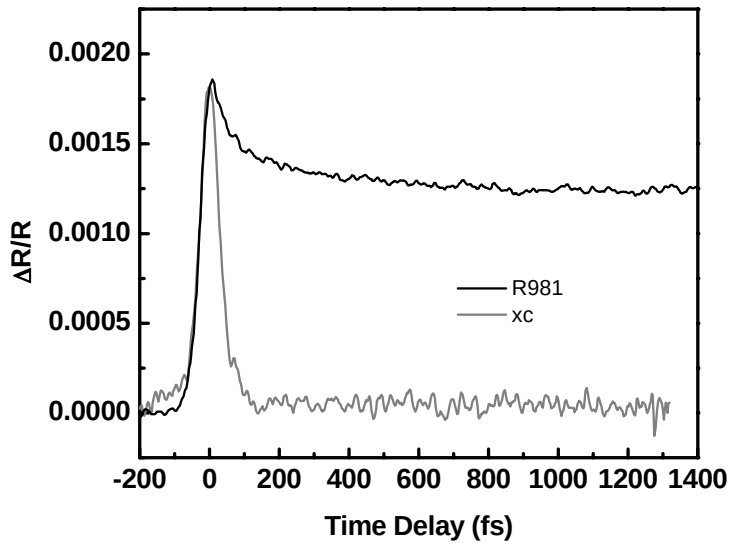

Figure B.5 Pump-probe of R981 oxidized 6/9/04 at 410C for 4.5 hours with 2 temperature ramps. The structure consists of 6 quantum wells embedded in a λ/2 layer of InP on top of a 7-pair Al_xO_y/$Al_{0.3}Ga_{0.7}As$ mirror.

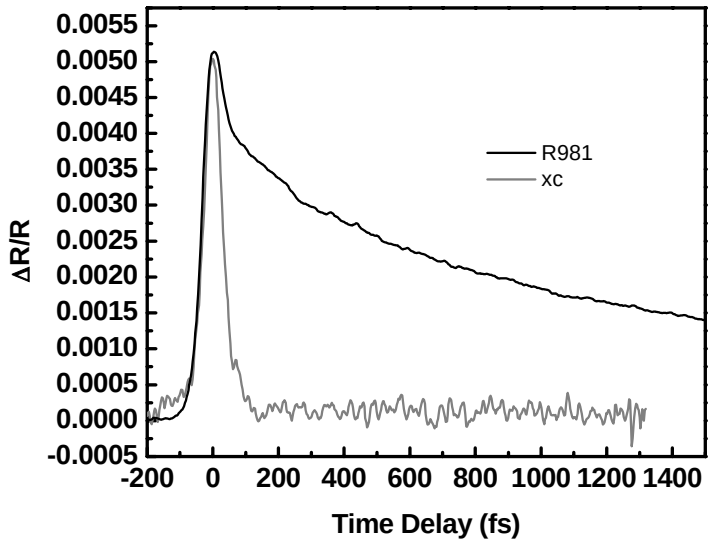

Figure B.6 Pump-probe of R981, oxidized 9/10/03 410C, 4 hr 45 minutes with a 50 minute ramp. The structure was proton bombarded with 40 keV protons at a dose of 10^{14} protons/cm^2 and was antireflection-coated with a λ/4 HfO_2. The structure consists of 6 quantum wells embedded in a λ/2 layer of InP on top of a 7-pair $Al_xO_y/Al_{0.3}Ga_{0.7}As$ mirror.

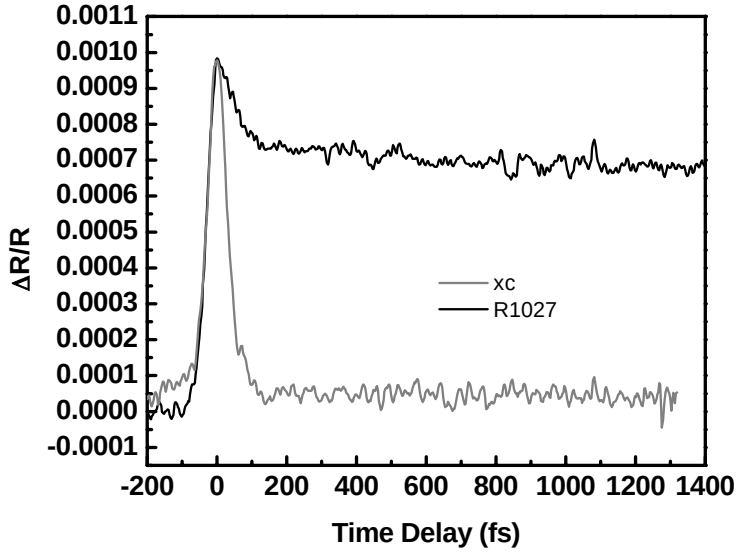

Figure B.7 Pump-probe of R1027, oxidized 6/5/04, 410C for 2 hours with 2 ramps. The structure consists of a λ/2 layer of InP containing 100 nm of $In_{0.5}Ga_{0.5}As$ on top of a 7-pair $Al_xO_y/Al_{0.3}Ga_{0.7}As$ mirror.

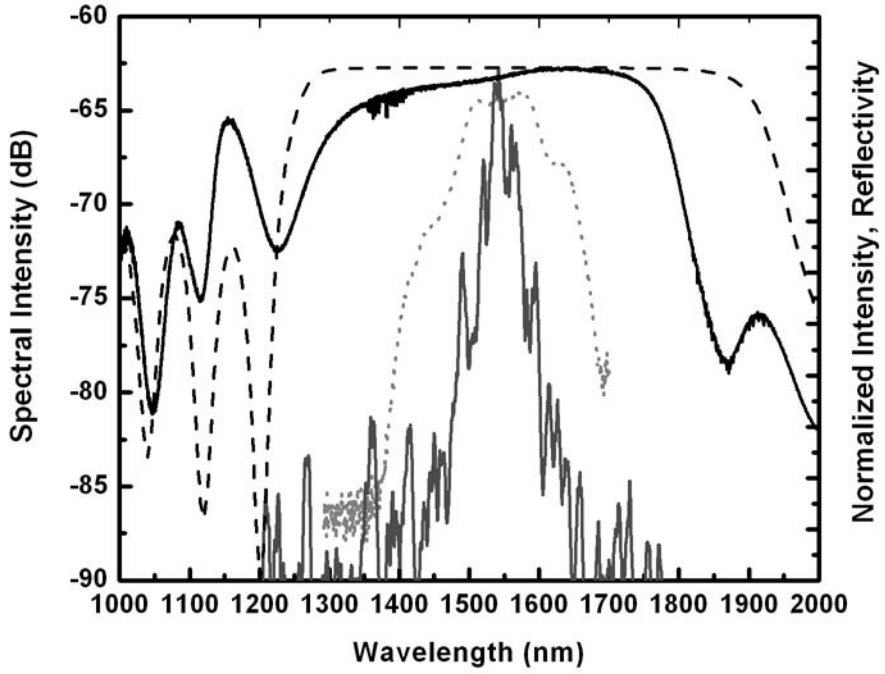

Figure B.8 For growth number R981, the measured and calculated reflectivity, the photoluminescence, and the 37-fs laser spectra (dotted grey).

By deconvolving the cross-correlation of pump and probe with the impulse response of the sample, one can extract the fast time constants. Preliminary deconvolution fits indicate a time constant between 40-100 fs, similar to the width of the cross correlation. The measurement should be repeated at a shorter wavelength of excitation so that the absorption edge of the samples does not filter the spectrum. Additionally, pump-probe could be performed with compressed pulses that are shorter or with an ultrafast source, such as the Cr^{4+}:YAG directly.

B.4 Conclusion

The 150-fs OPO pulses have been compressed to 37 fs using 1 m of highly nonlinear fiber and a standard grating compressor. A low dispersion broadband pump-probe setup was constructed, and ultrafast pump-probe performed on some ultrabroadband SBR samples. Preliminary results indicate a time constant for carrier-carrier scattering on the order of the pulsewidth.